IOP Publishing Reports on Progress in Physics
Rep. Prog. Phys. **79** (2016) 116501 (39pp) doi:10.1088/0034-4885/79/11/116501

Review

Vortices in high-performance high-temperature superconductors

Wai-Kwong Kwok[1], Ulrich Welp[1], Andreas Glatz[1,2], Alexei E Koshelev[1], Karen J Kihlstrom[1,3] and George W Crabtree[1,3]

[1] Materials Science Division, Argonne National Laboratory, Argonne, IL 60439, USA
[2] Department of Physics, Northern Illinois University, DeKalb, IL 60115, USA
[3] Departments of Physics, Electrical and Mechanical Engineering, University of Illinois at Chicago, Chicago, IL 60607, USA

E-mail: kwok@anl.gov

Received 13 December 2015, revised 5 July 2016
Accepted for publication 19 July 2016
Published 21 September 2016

Abstract

The behavior of vortex matter in high-temperature superconductors (HTS) controls the entire electromagnetic response of the material, including its current carrying capacity. Here, we review the basic concepts of vortex pinning and its application to a complex mixed pinning landscape to enhance the critical current and to reduce its anisotropy. We focus on recent scientific advances that have resulted in large enhancements of the in-field critical current in state-of-the-art second generation (2G) YBCO coated conductors and on the prospect of an isotropic, high-critical current superconductor in the iron-based superconductors. Lastly, we discuss an emerging new paradigm of *critical current by design*—a drive to achieve a quantitative correlation between the observed critical current density and mesoscale mixed pinning landscapes by using realistic input parameters in an innovative and powerful large-scale time dependent Ginzburg–Landau approach to simulating vortex dynamics.

Keywords: superconductivity, critical current, vortex matter, vortex pinning, superconducting wires, time-dependent Ginzburg–Landau

(Some figures may appear in colour only in the online journal)

1. Introduction

Two decades of basic and applied research have transformed brittle ceramic cuprate high-temperature superconductors (HTS) into flexible coated conductors that carry loss-less currents of 4 MA cm^{-2} at 77 K. These wires have been successfully implemented at pilot sites world-wide as prototype transmission lines and fault current limiters. Furthermore, new applications in energy generation via superconducting wind turbines and in energy storage via superconducting magnetic energy storage systems are at the horizon. A large barrier to broad acceptance of this revolutionary technology is the high cost of the wires for electricity transmission and their weak performance in high magnetic fields where the latter precludes their applications in superconducting rotating machinery. A decisive approach to lower the cost is to increase the wires' current-carrying capacity, thereby reducing the amount of superconducting material required for a given application. In other words, doubling the capacity can reduce the cost by half. For applications in high magnetic fields, current-carrying capacity depends strongly on magnetic field orientation with respect to the layered structure of the wire. In rotating machinery, the orientation of the windings with respect to the field changes constantly, favoring isotropic over anisotropic current-carrying capacity. More recently, the discovery of the iron-based superconductors has spurred interest in the application potential of this new class of superconducting materials. Although the superconducting transition temperatures, T_c, are generally lower than in the cuprates, these materials have relatively lower anisotropy, making them amenable for

applications in superconducting rotating machinery where the industry targets for operation temperature and magnetic field are 20–30 K and 1.5 to 3 Tesla, respectively.

The most important applications metric of a superconductor is the maximum loss-less current or critical current density it can carry at given operation conditions. This quantity is determined by the behavior of vortex matter—that is the macroscopic ensemble of vortex lines within a superconductor. Vortices appear inside the superconductor in sufficiently high magnetic fields and can be viewed as single quanta of magnetic flux composed of supercurrents circulating around normal cores. An electric current applied to a superconductor exerts a force on the vortices. Once this current reaches a critical threshold value, the critical current density, vortices are set in motion. As moving vortices dissipate energy, the superconductor loses its 'loss-less' current carrying ability. The interaction of vortices with defects in the underlying superconducting material can immobilize or pin vortices, and the strength of this pinning interaction determines the maximum 'loss-less' current that the superconductor can sustain. Thus, in order to enhance the current carrying capacity of superconductors, an understanding of the most effective vortex pinning defect structures needs to be achieved.

Currently, the dynamic behavior of vortex matter remains poorly understood due to the complexity of the vortex system, which consists of flexible vortex lines that interact with each other over long distances and with defect structures that in general contain a mixture of defects of various shapes and sizes, so-called mixed-pinning landscapes. In particular, innovative approaches that could identify and guide the rational design of optimal vortex pinning defect structures are highly desirable.

There are several factors that emerge for large-scale vortex pinning arrays that result in the ultimate bulk critical current. They include (i) the mutual long-range repulsion between vortex lines allowing at times for a single vortex to influence the motion of many of its neighbors, (ii) the inherent flexibility of vortex lines enabling them to simultaneously seek and attach to many pinning defects at different locations along its length and to move in intricate dynamic configurations as vortex segments detach and attach from one defect site to another, and (iii) the possibility of vortices cutting and reconnecting into new configurations in the course of their motion. Furthermore, the non-linear dynamic interaction of these vortices with a complex defect landscape and the interruption of the superconducting current pathways by non-superconducting defects that reduce the cross-sectional area available for supercurrent are issues to be addressed. Hence, predicting the dynamic behavior of large-scale arrays of vortices in these complex pinning landscapes is a fundamental challenge of high practical value and has so far remained out of reach of analytical theory and conventional numerical simulation.

In this review, we focus on the role of vortex matter in the recent scientific advances that have driven the critical current of high-performance, high-temperature superconductors to new limits. The synthesis and experimental challenges that emerge for understanding large-scale vortex pinning arrays include tailoring the synthesis for custom insertion of various size, shape, morphology and density of the pinning defects, differentiating the competition among the different types of defects that could confound vortex dynamics and static pinning and specifically identifying the dominant and secondary pinning defects within the material that is responsible for the bulk critical current. While there are many synthesis routes towards high-temperature superconducting wires, we limit our review mostly to so-called coated conductors that display very high critical current densities and are close to or are already industrially implemented. We loosely define 'high-T_c' as superconductors with transition temperatures near and above 35 K, following their discovery in cuprates. We present a brief review of the current synthetic strategies to tailor the defect structures and the surprising non-conventional methods using particle irradiation on commercial high-temperature coated conductors as a *viable* industrial option to substantially enhance the critical current in post-production wires. We will also review the critical current limits of the newly discovered, nearly isotropic iron based superconductors and their potential as the next commercial HTS coated conductor. In the last section, we review an emerging novel synergistic approach that combines theory, experiments and large-scale simulations of vortex matter to achieve a new paradigm, '*critical current by design*' that is, realizing a quantitative correlation between the observed critical current density and multi-scale mixed pinning landscapes by using realistic input parameters in a powerful, large-scale time dependent Ginzburg–Landau approach to simulating vortex dynamics.

2. Properties of vortex matter

2.1. What is vortex matter?

The high-performance superconductors described here are so-called type-II superconductors, meaning that a sufficiently high magnetic field penetrates inside them via the formation of vortices (Abrikosov 1957). Vortices can be viewed as non-superconducting cores that are surrounded by circulating persistent superconducting currents, see figure 1(a). The core radius is approximately given by the coherence length, ξ, which for high-temperature superconductors (HTS) is of the order of several nanometers, and the circulating supercurrents extend out to the magnetic penetration depth, λ, which is of the order of 100–200 nm. An isolated vortex in a bulk superconductor carries magnetic flux equal to the flux quantum $\Phi_0 = hc/2e \approx 2.068 \cdot 10^{-7}$ G $\cdot$ cm^2. As a consequence, the areal density of the lines n_v is set by the magnetic induction B as $n_v = B/\Phi_0$.

Arrays of vortices are known as vortex matter (Blatter *et al* 1994, Brandt 1995, Crabtree and Nelson 1997, Nattermann and Scheidl 2000, Blatter and Geshkenbein 2003) as they display properties that are reminiscent of ordinary material matter such as the existence of the crystalline state which is characterized by the elastic energy and a melting transition transforming this state into the liquid phase. Contrary to atomic matter, however, interaction with disorder due to material imperfections plays a very important role in the physics of vortex matter. At a qualitative level, the different phases

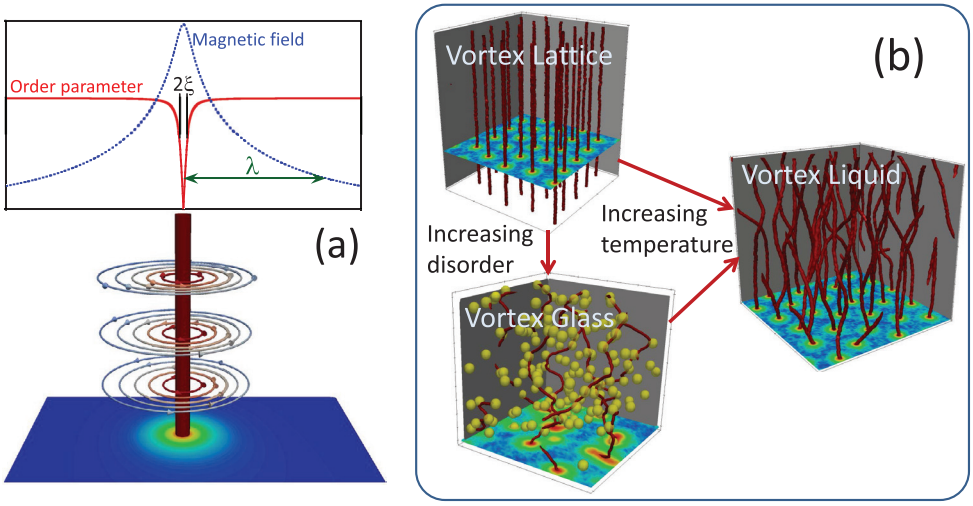

Figure 1. (a) Structure of an isolated vortex (red). The top graph shows the distribution of the magnetic field and order parameter amplitude in a cross-section through the vortex. The vector-lines circling the vortex represent the supercurrent screening the magnetic flux of the vortex. The bottom plane-cut shows the distribution of the order parameter. (b) Illustrations of different vortex states for differnt temperatures and disorder (yellow). 3D illustrations are generated using the time-dependent Ginzburg–Landau equations, see section 4.2.

arising in vortex matter appear due to the interplay between the vortex–vortex interaction, thermal fluctuations, and the interaction of vortices with material defects. In the absence of any disorder in the superconducting material and at sufficiently low temperatures, vortices form a regular lattice, the Abrikosov lattice, see figure 1(b). On increasing temperature, thermal fluctuations induce a 1st-order melting transition transforming the Abrikosov lattice into the vortex liquid phase in which vortices are no longer bound to a certain position but can freely slide past each other. Strong disorder in the superconducting material drives vortices off their lattice positions and destroys the crystalline order even at low temperatures leading to a vortex-glass state, see figure 1(b). With increasing temperature, the vortex glass transforms into the vortex liquid via a continuous phase transition.

High-power applications of superconductors are centered on their ability to carry large loss-less currents.[4] The behavior of the superconductor is inevitably determined by the interaction of currents flowing in the superconductor with the various vortex states that arise either in response to an external magnetic field or are generated by the flowing currents themselves. An external electric current density $\mathbf{J}$ generates a Lorentz force acting on the vortex line perpendicular to both the current direction and the unit vector along the line $\mathbf{n}$, $\mathbf{F}_\mathrm{L} = (\Phi_0/c)\mathbf{J} \times \mathbf{n}$, see figure 2. In a uniform superconductor, this force drives the vortex with velocity $\mathbf{v}$ which is limited by the Bardeen–Stephen friction viscosity η arising from the normal quasiparticles in the vortex core, $\mathbf{v} = \mathbf{F}_\mathrm{L}/\eta$. Motion of the vortices due to the Lorentz force generates a finite electric field proportional to the velocity, $\mathbf{E} = \mathbf{B} \times \mathbf{v}/c$, which is perpendicular to the velocity and parallel to the electric current leading to dissipation of energy and to a finite flux-flow resistivity. Therefore, in the presence of vortices, a uniform

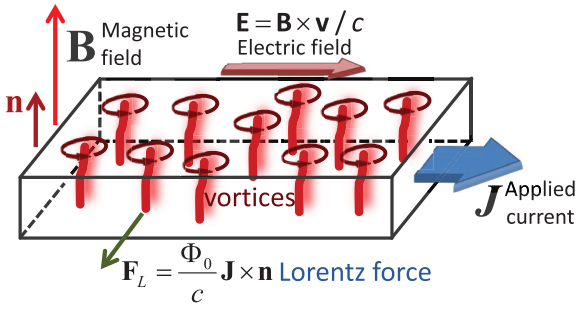

Figure 2. Illustration of dissipation caused by moving vortices in uniform superconductors. An applied electric current $\mathbf{J}$ generates a Lorentz force F_L acting on vortices perpendicular to the current direction, which drives them with velocity $\mathbf{v}$. The vortex motion generates a finite electric field $\mathbf{E}$ proportional to $\mathbf{v}$ and perpendicular to its direction. This mean that $\mathbf{E}$ is parallel to $\mathbf{J}$, corresponding to a finite flux-flow resistivity.

superconductor loses its key property of supporting dissipation-free currents. The successful fabrication of high-performance superconductors can only be achieved by suppression of vortex mobility, i.e. by effectively pinning vortices in their positions. In this regard, no simple defect can optimally pin the vortices over the entire temperature and magnetic field range of the superconductor's phase diagram. Empirical studies have demonstrated that in order to achieve the highest critical current for a targeted temperature and magnetic field regime, a mixture of various defect morphology types is necessary, creating a complex mixed-pinning landscape for vortex interactions. Unraveling the intricate dynamic behavior of vortex matter in a mixed-pinning landscapes will provide crucial information towards a rational design for enhancing the performance of applied superconductors.

2.2. *Phenomenology of vortex matter*

The theoretical descriptions of an individual vortex and vortex-matter states are mostly based on the Ginzburg–Landau (GL)

[4] We do not consider here properties relevant for other applications of superconductivity such as Josephson junctions (Barone and Paterno 1982), superconducting detectors (Zmuidzinas 2012), or superconducting cavities (Padamsee 2014).

model. This model also forms the basis for the simulations of vortex dynamics presented in section 4.2. While a phenomenological theory, this model can be rigorously derived from the microscopic Bardeen–Cooper–Schrieffer theory in the vicinity of the critical temperature T_c of the superconducting transition (Gor'kov 1959). The GL theory describes the superconducting state in terms of a spatially dependent complex order parameter ψ, which is related to the superconducting electron density (see figure 1(a)—at the center of the vortex, the superconducting order parameter is zero, as the material at the core of the vortex is in the normal state). In the presence of a magnetic field, **B**, the GL free energy is given as,[5]

$$\mathcal{F}_{GL} = \int d^3\mathbf{r}\left[-a_0\epsilon(\mathbf{r})|\psi|^2 + \frac{b}{2}|\psi|^4 + \sum_\alpha \frac{1}{4m_\alpha}\left|\left(\hbar\nabla_\alpha + \frac{2e}{\imath c}A_\alpha\right)\psi\right|^2 + \frac{\mathbf{B}^2}{8\pi}\right] \quad (1)$$

where $-e$ is the electron's charge, c is the speed of light, m_α are the effective mass components with $\alpha = x, y, z$ (we will assume that $m_x = m_y = m$, $m_z/m_x = \gamma^2 > 1$), a_0, b are phenomenological constants, **A** is the electromagnetic vector potential, and $\imath$ is the imaginary unit. Furthermore, $\epsilon(\mathbf{r}) = [T_c(\mathbf{r}) - T]/T$ is a dimensionless function of temperature, which vanishes at the local critical temperature $T \to T_c(\mathbf{r})$. The GL theory of superconductivity has two characteristic length scales: the coherence length, $\xi_0 = \sqrt{\hbar^2/4ma_0}$, and the London penetration length $\lambda_0 = \sqrt{mc^2/8\pi e^2\psi_0^2}$, where $\psi_0 = \sqrt{a_0/b}$ is the scale for the equilibrium order parameter in the absence of an electromagnetic field. For a spatially uniform superconducting critical temperature, $T_c(\mathbf{r}) = T_c$ and, therefore, $\epsilon(\mathbf{r}) = \epsilon$. The temperature-dependent coherence length $\xi = \xi_0/(1 - T/T_c)^{1/2}$ describes the typical scale of order parameter variations in space and the magnetic penetration length $\lambda = \lambda_0/(1 - T/T_c)^{1/2}$ describes the depth to which a small external magnetic field can penetrate into the superconductor. The temperature-independent ratio $\kappa = \lambda/\xi = \lambda_0/\xi_0$ is called the GL parameter. The typical scale for the energy density gain in the superconducting state $a_0^2/2b$ is called the condensation energy. The magnetic field at which the magnetic energy $B^2/8\pi$ is equal to the condensation energy defines the thermodynamic field $H_{c0} = \Phi_0/(2\sqrt{2}\,\pi\xi_0\lambda_0)$. Near T_c, the temperature-dependent thermodynamic field H_c vanishes as $H_c = H_{c0}(1 - T/T_c)$. Furthermore, GL theory yields the highest current a superconductor can carry, the depairing critical current density, $J_{dp} = c\Phi_0/(12\sqrt{3}\,\pi^2\xi\lambda^2)$, $J_{dp} \propto (1 - T/T_c)^{3/2}$. Beyond this current, the kinetic energy of the supercurrent electrons exceeds the condensation energy and the superconducting state breaks down.

The cuprate high-temperature superconductors are layered materials, in which the superconductivity arises in the CuO_2 planes and electronic tunneling leads to the Josephson coupling between these planes. In moderately anisotropic materials, such as $YBa_2Cu_3O_{7-\delta}$, this coupling is strong and the order parameter typically changes smoothly from layer to layer meaning that they can be treated as anisotropic three-dimensional superconductors. In this review, we focus on such materials and do not discuss highly-anisotropic superconductors like $Bi_2Sr_2CaCu_2O_{8-\delta}$, where the layered structure has a dramatic influence on properties of the vortex matter, see, e.g. Blatter and Geshkenbein (2003).

Equilibrium states of superconductors are obtained from the GL equations by minimizing the GL free energy (1): $\delta\mathcal{F}_{GL}/\delta\psi^* = 0$ and $\delta\mathcal{F}_{GL}/\delta\mathbf{A} = 0$. In particular, these equations allow for a solution in the form of an isolated vortex line defined by the phase singularity in the order parameter, where the phase winds by 2π around the vortex. This topological property determines other properties of the vortex such as the vanishing of the order parameter at the vortex core, the pattern of supercurrents circulating around it, and the total magnetic flux equal to the flux quantum Φ_0. In a uniform material at low temperatures, vortices are straight and have a line energy of

$$\epsilon_l \approx \epsilon_0[\ln(\lambda/\xi) + 0.497] \quad (2)$$

with $\epsilon_0 = \Phi_0^2/(4\pi\lambda)^2$. This line energy determines the lower critical field $H_{c1} = 4\pi\epsilon_l/\Phi_0$ above which the formation of vortices in the bulk becomes energetically favorable. Straight parallel vortex lines separated by distance r repel each other with the interaction energy per unit length $U(r) = 2\epsilon_0 K_0(r/\lambda)$ where $K_0(x)$ is the modified Bessel function of the second kind. Due to this interaction, and for negligible thermal fluctuations in the absence of disorder, the lines form a triangular lattice with the period $a = \sqrt{2\Phi_0/\sqrt{3}\,B}$.[6] Without thermal fluctuations, this lattice exists as long as the distance between vortices exceeds the coherence length, corresponding to magnetic fields below the upper critical field $H_{c2} = \Phi_0/2\pi\xi^2$, beyond which the superconductor reverts to the normal state.

A key feature of high-temperature superconductors is a strong amplitude of thermal fluctuations. The strength of thermal fluctuations in a superconductor can be conveniently quantified by the relative temperature range at zero magnetic field where fluctuations become strong. This parameter is known as the Ginzburg number $Gi = \Delta T_f/T_c$ (Larkin and Varlamov 2005). For three-dimensional superconductors, it is proportional to the square of the ratio of the thermal energy $k_B T_c$ to the condensation energy within the correlation volume $H_{c0}^2\xi_0^3/(8\pi\gamma)$:

$$Gi = \frac{1}{2}\left(\frac{\gamma k_B T_c}{H_{c0}^2\xi_0^3}\right)^2 = \frac{1}{2}\left(\frac{8\pi^2\gamma\lambda_0^2 k_B T_c}{\Phi_0^2\xi_0}\right)^2 \quad (3)$$

where k_B is the Boltzmann constant. The latter equation can be rewritten as $Gi = 0.0325(\gamma\kappa\ \lambda_0(\text{cm})\ T_c(\text{K}))^2$. The large amplitude of thermal fluctuations in HTSs is a consequence of very high transition temperature, small coherence length, high anisotropy, and low superfluid density, i.e. large λ_0.

[5] Here we use CGS units.

[6] The triangular vortex lattice always gives the ground state for temperatures sufficiently close to T_c and for sufficiently small magnetic fields. However, in several clean superconducting materials, such as $YBa_2Cu_3O_7$ (Brown *et al* 2004) or borocarbides (De Wilde *et al* 1997, Sakata *et al* 2000), the symmetry of the electronic structure favors a square vortex lattice within a wide region of the temperature-magnetic field phase diagram.

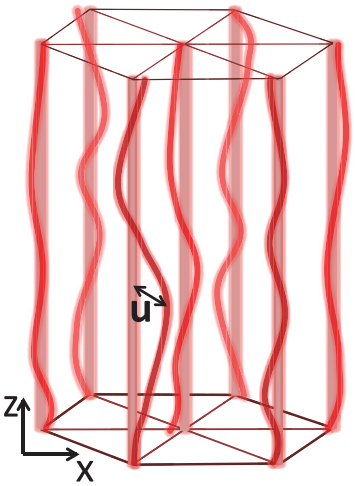

Figure 3. Elastic deformations of vortices $\mathbf{u}(\mathbf{r})$ with respect to ideal lattice positions. Such deformations can be caused by either thermal noise or interactions with defects.

For cuprates one finds $Gi \sim 2 \cdot 10^{-2}$ which is much higher than for conventional clean low-T_c materials, where $Gi < 10^{-7}$. For iron-based superconductors the Ginzburg number $Gi = 10^{-4} - 10^{-3}$ is somewhat smaller than for cuprate HTSs but still much larger than for conventional superconductors.

Thermal fluctuations are especially pronounced in the vortex state. For the treatment of these fluctuations and interaction with disorder, one has to consider small displacements $\mathbf{u}(\mathbf{r})$ with respect to the equilibrium ground-state configuration, see figure 3. We consider first an isolated vortex line. In anisotropic superconductors, the vortex line is highly flexible and can deform easily either due to thermal noise or interactions with defects. A periodic displacement of the line from the equilibrium position, $u(z) = u_0 \cos(k_z z)$ with $\lambda^{-1} \ll k_z \ll \xi^{-1}$, costs energy per unit length of $\epsilon_1(k_z) k_z^2 u_0^2$. Here the effective line tension $\epsilon_1(k_z)$ consists of two contributions (Brandt 1995). The first term, $\epsilon_1^{(1)}(k_z) \approx (\epsilon_0/\gamma^2) \ln(\gamma/k_z\xi)$, appears due to the kinetic energy of supercurrents along the c-axis, which is determined by the anisotropy factor γ. The second term, $\epsilon_1^{(2)}(k_z) = (\epsilon_0/2k_z^2\lambda^2) \ln(1 + \lambda^2 k_z^2)$, mostly comes from the perturbation of the magnetic part of the energy. Both terms are nonlocal, since they do not have the simple elastic-string form with k_z-independent elastic tension ϵ_1. In moderately anisotropic superconductors, the first term typically dominates. In this term the additional k_z dependence appears only under the logarithm, meaning that the nonlocality is weak. In most cases, this weak nonlocality is not essential and a vortex line is frequently approximated by an elastic string with the line tension $\epsilon_1 \approx (\epsilon_0/\gamma^2) \ln(\gamma L_k/\xi)$, where L_k is the cutoff length determined by the typical k_z in the problem under consideration.

In the case of a vortex crystal, small displacements $\mathbf{u}(\mathbf{r})$ with respect to the ideal lattice position cost elastic energy, similar to usual atomic crystals. This energy cost has to be evaluated by taking into account the long-range interactions between the vortex lines leading to the following result, see, e.g. Brandt (1995),

$$E_{\rm el} = \frac{1}{2} \int \frac{{\rm d}^3\mathbf{k}}{(2\pi)^2} \{ [C_{11}(\mathbf{k}) - C_{66}][\mathbf{k}_\parallel \cdot \mathbf{u}(\mathbf{k})]^2 + [C_{66} k^2 + C_{44}(\mathbf{k}) k_z^2] |\mathbf{u}(\mathbf{k})|^2 \}. \quad (4)$$

Here, $\mathbf{u}(\mathbf{k})$ is the Fourier transform of $\mathbf{u}(\mathbf{r})$,

$$C_{11}(\mathbf{k}) = \frac{B^2}{4\pi} \frac{1 + \lambda_c^2 k^2}{(1 + \lambda^2 k^2)(1 + \lambda_c^2 k_\parallel^2 + \lambda^2 k_z^2)}, \; C_{66} = \frac{B\Phi_0}{(8\pi\lambda)^2}, \quad (5)$$

$$C_{44}(\mathbf{k}) = \frac{B^2}{4\pi} \frac{1}{1 + \lambda_c^2 k_\parallel^2 + \lambda^2 k_z^2} + \frac{B}{\Phi_0} \epsilon_1(k_z) \quad (6)$$

are the bulk, shear, and tilt moduli for the field range $H_{c1} \ll B \ll H_{c2}$. The second term in $C_{44}(\mathbf{k})$ comes from the elastic tension of isolated lines. The strong $\mathbf{k}$ dependence of the bulk and tilt moduli reflects nonlocality caused by long-range interactions. For small $\mathbf{k}$, the shear modulus C_{66} is much smaller than the bulk modulus $C_{11}(\mathbf{k})$ and hence the energy cost for shear deformations is much smaller than for compression. The elastic energy provides a basis for the analysis of thermal fluctuations of the vortex lattice and its response to disorder.

2.3. Vortex phase diagram

The Abrikosov lattice can be destroyed either by thermal fluctuations or by strong disorder. At finite temperatures the vortex lines wiggle around their equilibrium positions due to thermal noise, see figure 3. The amplitude of these fluctuations $\langle u^2 \rangle$ is determined by the shear part of elastic energy (4). In clean materials the lattice melts when the typical fluctuation displacement $u_{\rm f} = \sqrt{\langle u^2 \rangle}$ reaches a certain fraction of the vortex-lattice spacing (Lindemann criterion), $u_{\rm f} = c_{\rm L} a$ where $c_{\rm L} \approx 0.1$–0.2 is the Lindemann number. The vortex liquid phase emerging above the melting line is composed of entangled and mobile vortex lines. Similar to atomic matter, the melting is a 1st-order transition. In particular, it is accompanied by jumps in the resistivity, specific heat, and equilibrium magnetization. The melting temperature has been evaluated first using the Lindemann criterion (Houghton *et al* 1989) and then accurately computed in numerical simulations (Koshelev and Nordborg 1999) giving $T_{\rm m} \approx 0.1 \epsilon_0 a/\gamma$ for $H_{c1} \ll B \ll H_{c2}$. Thermodynamic measurements of the melting transition have been reported in several experimental papers, see e.g. Pastoriza *et al* (1994), Zeldov *et al* (1995), Schilling *et al* (1996) and Welp *et al* (1996). The melting line for disorder-free materials is shown in figure 4. Due to strong thermal fluctuations in cuprate HTSs, the melting magnetic field at fixed temperature lies considerably below the upper critical field H_{c2} above which the material becomes normal, and the liquid phase occupies a significant portion of the phase diagram. This has large ramifications for potential applications since the vortex liquid cannot easily be pinned by defects. In contrast, in conventional low-T_c superconductors the melting field and H_{c2} practically coincide.

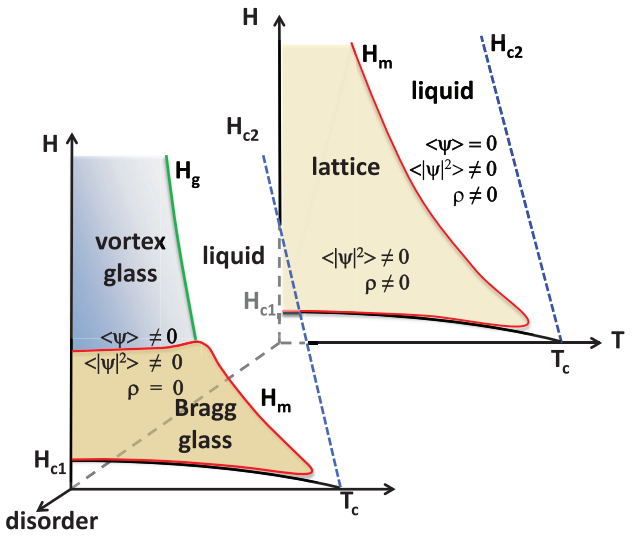

Figure 4. Schematic vortex phase diagrams of an anisotropic 3D superconductor for the clean case and for an intermediate degree of disorder. The clean system contains the Meissner phase below H_{c1}, the Abrikosov lattice phase and the liquid phase. The lattice and liquid phases are separated by the 1st order melting line H_m. Due to thermal fluctuations there is no superconducting phase coherence in the vortex liquid phase, the average value of the order parameter $\langle\psi\rangle$ averages to zero, and the electrical resistance ρ is finite. The transition into the normal state above H_{c2} is a crossover, since due to fluctuations, $\langle|\psi|^2\rangle$ stays finite even above H_{c2}. In an ideally clean system $\rho \neq 0$, since any current will set the lattice in motion, see figure 2. With finite disorder the Abrikosov lattice gives way to the vortex glass phase at high fields and to the Bragg glass at low fields. The glass phases display phase coherence, time averages $\langle\psi\rangle \neq 0$, and finite resistivity $\rho \neq 0$. For very strong disorder, the Bragg glass phase disappears, and the vortex glass is the only remaining vortex solid phase.

Disorder in the superconducting material drives vortices off their equilibrium lattice positions destroying long-range crystalline order (Larkin and Ovchinnikov 1979). However, for sufficiently weak disorder and relatively low magnetic fields quasi-long-range order can persist and Bragg peaks in the structure factor are preserved. The vortex lattice in the presence of relatively weak disorder is frequently called a Bragg glass (Giamarchi and Le Doussal 1995, Emig *et al* 1999, Nattermann and Scheidl 2000). Analogous to the Abrikosov lattice, the Bragg glass transforms into the vortex liquid at the melting point via a 1st-order phase transition. With increasing strength of disorder at low temperatures, the quasi-long-range order is destroyed and the Bragg glass transforms into an amorphous vortex glass, see figure 4. This transition also takes place with increasing magnetic fields, as demonstrated by the Lindemann analysis in Ertaş and Nelson (1996). In strongly disordered superconductors, the Bragg-glass state is absent. The most essential dynamic feature of the glass states is the vanishing of the linear resistivity, $\rho(J) = E/J \to 0$ for $J \to 0$. With increasing temperature, the vortex glass melts into the vortex liquid via a continuous phase transition at which finite resistivity emerges (Fisher 1989). Another experimental signature of the transition into the vortex-glass phase is the emergence of a hysteretic magnetization, signaling vortex pinning and the flow of persistent supercurrents. In fact, the magnetization hysteresis, that is the difference in magnetization measured on increasing and decreasing magnetic fields, is a direct measure of the critical current density (Bean 1964, Gyorgy *et al* 1989). The temperature-dependent magnetic field line separating irreversible and reversible regimes is known as the irreversibility line and is usually very close to the glass transition line, $H_g(T)$.

2.4. Interaction of vortices with defect pinning centers

Disorder caused by different types of crystalline defects plays a very special role in the physics of vortex matter because it is responsible for pinning and immobilization of vortices, thereby restoring the capability of the superconductor to carry dissipation-free currents. The types of defects are pointlike pinning centers (impurities, vacancies, inclusions), one-dimensional defects (dislocations, irradiation tracks), and two-dimensional defects (twin boundaries, stacking faults). One- and two-dimensional defects are also referred to as correlated pinning sites. Figure 5 shows schematics of vortex configurations in pinning structures of various dimensionality.

Point defects are the most typical and most studied pinning centers. The interaction of an isolated pin with a vortex is characterized by the pinning energy and the pin-breaking force. One can separate weak pins, e.g. atomic defects, from strong pins, which have dimensions comparable to the coherence length.

2.4.1. Atomic defects: δT_c and δl pinning. Introducing a large number of atomic defects influences not only pinning of vortices, but also macroscopic superconducting properties. The impact of impurities on superconductivity is determined by their electronic configurations as well as symmetry of the superconducting order parameter. Recent advances in scanning tunneling microscopy (Fischer *et al* 2007, Hoffman 2011) have enabled the investigation of the electronic structure of separate defects. Experimental and theoretical studies of impurity effects in conventional and unconventional superconductors have developed into a separate large field (Balatsky *et al* 2006).

The microscopic structure of atomic defects is manifested by their electronic scattering properties, which can be either purely of potential or of magnetic type. Within the theoretical BCS framework, potential-type impurities in isotropic s-wave superconductors do not influence the transition temperature (Anderson theorem) (Anderson 1959). Nevertheless, such non pair-breaking impurities affect other important properties of superconductors. In particular, they enhance the upper critical field and suppress the superfluid density. Both effects enhance thermal fluctuations.

The classical example of pair-breaking impurities which suppress superconductivity is given by magnetic impurities (Abrikosov and Gor'kov 1960). In superconductors with unconventional order parameters, such as a d-wave order parameter in cuprate HTSs, potential-type impurities are also pair breakers and suppress T_c.[7]

[7] In fact, due to strong correlation effects, superconductivity in cuprate HTSs is more stable with respect to disorder then one can expect for a simple BCS d-wave superconductor.

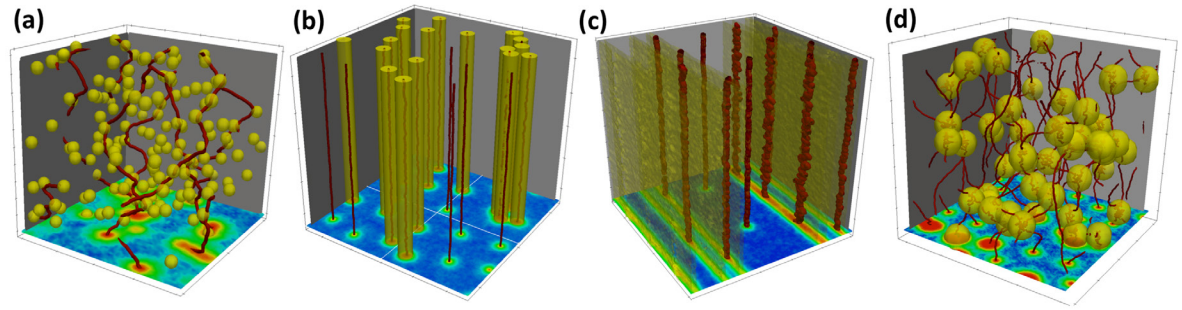

Figure 5. 3D Illustration of vortex matter (red) in defect structures (yellow) of different dimensionality. (a) Random atomic / pointlike defects, (b) linear defects (irradiation induced tracks, synthesited self-assembled nanorods, dislocations), (c) planar defects (twin boundaries, stacking faults, layered structure), (d) large random defects (rare earth oxide precipitates, irradiation collision cascades, defect clusters, voids). All figures created using time-dependent Ginzburg–Landau equations, see section 4.2. The bottom plane-cuts show the distribution of the superconducting order parameter amplitude or condensate density (blue: high, red: low).

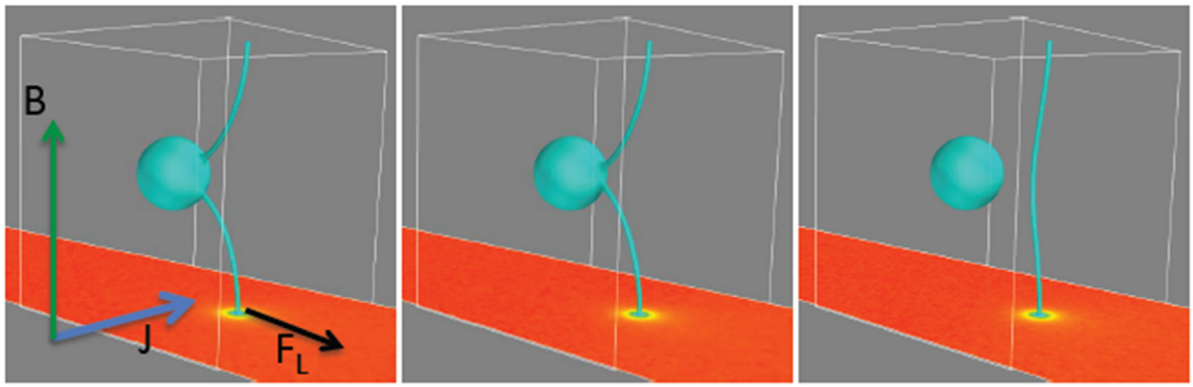

Figure 6. Visualization of depinning of a vortex line from a large-size defect obtained from simulations using the time-dependent Ginburg-Landau model. Magnetic field (**B**), applied current (**J**) and resulting Lorentz force ($\mathbf{F}_L$) are indicated.

The electronic scattering induced by atomic defects also determines their vortex-pinning properties. Defects that cause pair-breaking scattering, which suppresses T_c yield so-called δT_c-pinning, i.e. the pinning potential of these impurities can be phenomenologically described by spatial variations of T_c, see equation (1). Non pair-breaking potential impurities in s-wave superconductors give rise to the so-called δl pinning, where l is the electron mean-free path. Phenomenologically, the pinning potential in this case is caused by random variations of the coefficient in the gradient term of the Ginzburg–Landau energy, equation (1). A defect can be characterized by the pinning energy, u_p, range r_p and pinning force $f_p \sim u_p/r_p$. In the case of atomic impurities the effective range r_p is close to the coherence length ξ. The relation between pinning strength of atomic defects and their scattering properties was derived from the microscopic theory in Thuneberg *et al* (1984). Similar results from simpler considerations were obtained in Blatter *et al* (1994).

2.4.2. Large-size defects. Large-size defects of several coherence lengths are particularly important as they produce strong pinning. In this section, we analyze the parameters describing the interaction of vortices with large-size pinning centers. We consider an insulating spheroid with axes b and b_z as a model for such a pinning site. When a vortex line is located on this spheroid, a piece of the vortex core with length b_z is eliminated. This leads to so-called core pinning, because the condensation energy in the normal core of this vortex segment is recovered. Using the vortex line energy (2), the pinning energy u_p can be evaluated as

$$u_p \approx 2 b_z \varepsilon_0 \ln(b/\xi). \tag{7}$$

Another key parameter is the pin-breaking force f_p. This is the maximum force with which the defect pinning site can act on the vortex and for a large-size inclusion, has a nontrivial origin. With increasing external force, the tips of the vortex slide along the surface of the inclusion until an instability develops which leads to the reconnection of the tips near the equator of the spheroid and subsequent depinning of the vortex, as illustrated in figure 6. In this scenario, the pin-breaking force is determined mostly by the line tension of the vortices rather than by the defect pinning parameters, contrary to small defects. The evaluation of the external force at which the sliding vortex tips meet near the equator gives the following estimate

$$f_p \approx 2\frac{\varepsilon_0}{\gamma} \ln \frac{b_z}{\xi_c}, \tag{8}$$

where ξ_c is the c-axis coherence length.

An important feature is that the interaction of the vortex line with a remote pin is long-ranged. This long-range interaction appears due to the perturbation of the supercurrent around the vortex caused by the inclusion. In the case $b_z \gg b/\gamma$ and

for distances between the vortex and pin r within the range $b \ll r \ll \lambda$, the interaction energy is given by

$$U_i(r) \approx -\frac{2\varepsilon_0 V_p}{\pi r^2}, \quad (9)$$

where $V_p = (4\pi/3)b_z b^2$ is the volume of the pinning site. This long-range interaction facilitates the trapping of vortices by the pins.

2.4.3. Magnetic inclusions. Ferromagnetic inclusions carrying a magnetic moment may have additional benefits for efficient pinning.[8] A magnetic particle generates circulating screening supercurrents around it leading to an additional long-range interaction with vortex lines acting on the length scale of the London penetration depth, λ (Snezhko *et al* 2005). If the particle magnetization M is too large, it can generate generate vortex loops by itself (Doria *et al* 2007). For a spherical particle with radius b, vortex loops are created when the particle magnetization exceeds the critical value, $4\pi M_{cr} = \Phi_0/\pi b^2$. We limit ourselves to the case $M < M_{cr}$ here. For a particle with radius $b \ll \lambda$ magnetized along the z direction, the screening current at distance ρ from the particle center can be approximately expressed as (Snezhko *et al* 2005)

$$j_\varphi(\rho,\theta) \approx \frac{cMb^3}{3\lambda^2\rho^2}\left(1+\frac{\rho}{\lambda}\right)\exp\left(-\frac{\rho-b}{\lambda}\right)\sin\theta, \quad (10)$$

where φ and θ are the polar angles. Hence a straight vortex line along the z axis at a distance r from the particle within the range $b < r \ll \lambda$, experiences a magnetic interaction force given by

$$f_M(r) = \frac{\Phi_0}{c}\int_{-\infty}^{\infty} j_\varphi[\rho(r,z),\theta(r,z)]\mathrm{d}z \approx \frac{2\Phi_0 M b^3}{3\lambda^2 r}. \quad (11)$$

This force decays very slowly as $1/r$ with distance. In contrast, as follows from equation (9), the core-pinning force decays much faster, as $1/r^3$. The maximum magnetic pinning force at $r \sim b$ can be estimated as

$$f_{M,p} \lesssim \frac{\Phi_0 M b^2}{\lambda^2}. \quad (12)$$

For large-size particles and/or large M, the above equation probably overestimates the pinning force, because it neglects deformations of the vortex line caused by the interaction with the particle. The magnetic pinning energy for the vortex line located at the particle is approximately

$$u_{M,p} \approx \frac{2\Phi_0 M b^3}{3\lambda^2}\ln(\lambda/b). \quad (13)$$

As expected, for $M = M_{cr}$ it is approximately given by the energy of the vortex segment inside the particle, $u_{M,p}^{max} \approx \varepsilon_0 b$, similar to the core-pinning energy, equation (7).

The above results are obtained for the optimal configuration when the particle magnetization is aligned with the direction of the magnetic field. In this case, the direct benefit of the particle's magnetic moment is enhancement of the pin-breaking force and pinning energy. Furthermore, the long-range tail in the interaction should improve pinning efficiency as it allows particles to capture moving vortices at larger distances. At small magnetic fields, this should increase the fraction of pin sites trapping the vortex lines. One can also expect the long-range interactions to suppress the vortex creep rate.

Experimental studies of magnetic pinning were initiated in pioneering papers on Fe particles in Hg-In alloy (Alden and Livingston 1966a, 1966b) and Gd particles in Nb (Koch and Love 1969, Palau *et al* 2007). Later, pinning by Ni and Fe particle has been studied in practically important NbTi wires (Rizzo *et al* 1996). More recently, bulk magnetic pinning has been extensively investigated in MgB_2 containing different magnetic nanoparticles (Prozorov *et al* 2003, Snezhko *et al* 2005, Sandu and Chee 2014, Novosel *et al* 2015). As for cuprate HTS, magnetic pinning has been studied in thin films (Wimbush *et al* 2010) and in bulk polycrystalline materials (Tsuzuki *et al* 2011, Dong *et al* 2014). It was found that a small amount of magnetic particles enhances the critical currents. However, this enhancement is typically quite moderate and it is challenging to prove experimentally that the enhancement is a direct result of the particles' magnetism. We should also note that, at present, record-high critical currents in the best high-performance superconducting materials are achieved using nonmagnetic inclusions, as it will be discussed below in section 3. Nevertheless, magnetic pinning remains a viable route to increasing critical currents in practical superconductors.

2.5. Basic pinning scenarios

The emergence of macroscopic pinning forces from the collective action of multiple randomly-located pins is a long-standing nontrivial problem (Campbell and Evetts 1972). Consider random pins with density n_p, where each pin is characterized by the pinning energy u_p, the maximum pinning force f_p and the typical range r_p (for atomic pins $r_p \approx \xi$). Depending on these pinning parameters and vortex density set by the magnetic field, many regimes can be realized. Two major scenarios are known as *collective pinning* and *strong pinning*[9] and each of them can be further subdivided into single-vortex or lattice regimes.

In the lattice regime for small n_p, the transition between the collective and strong pinning scenarios follows from the consideration of the interaction of an isolated pin with the lattice (Blatter *et al* 2004). The pin located at distance r from the nearest vortex line causes the displacement of this line by $u(r)$. If the pin is weak then the function $u(r)$ is single valued and the formal averaging over all pin positions gives zero bulk pinning force. In this collective regime, a nonzero macroscopic pinning force appears due to fluctuations of the macroscopic disorder potential arising from many impurities (Larkin and

[8] We focus here only on bulk magnetic pinning and do not consider pinning by external magnetic structures in patterned superconductor-ferromagnet bilayers, which is a separate extended field, see, e.g. reviews (Lyuksyutov and Pokrovsky 2005, Aladyshkin *et al* 2009).

[9] To avoid confusion, we note that in this context the term 'strong pinning' refers to pinning by a dilute array of strong defects, and not to pinning landscapes leading to high critical currents.

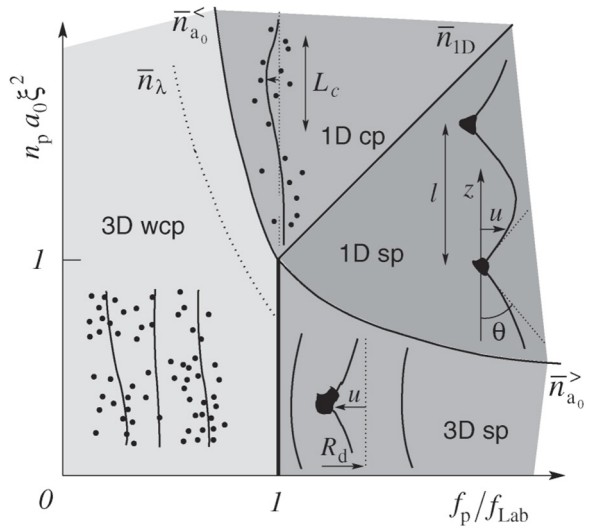

Figure 7. Pinning diagram delineating the various regimes involving collective versus individual pinning and 1D-line versus 3D-bulk pinning (f_{Lab} denotes the Labusch force): 3D wcp, bulk weak collective pinning; 1D cp, collective line pinning; 1D sp, strong line pinning; 3D sp, bulk strong pinning. Lines refer to crossovers. (Reprinted figure with permission from Blatter *et al* (2004). Copyright (2004) by the American Physical Society.)

Ovchinnikov 1979), as discussed in detail in the next section. For a sufficiently strong pin, the function $u(r)$ becomes multi-valued within some range of r. This happens when the pinning force satisfies the so-called Labusch criterion

$$f_p > f_{Lab} = r_p \sqrt{\frac{4\pi B}{\Phi_0} \varepsilon_0 \varepsilon_1}. \tag{14}$$

In this case for a dynamically trapped vortex lattice, the averaging over pins yields a finite bulk pinning force. In the strong-pinning lattice regime, the pins act independently such that the bulk pinning force is proportional to their density n_p.

The phase diagram of figure 7 from Blatter *et al* (2004) summarizes the possible pinning regimes at fixed magnetic field. The lattice collective pinning regime (3D wcp) is realized at small f_p. For $f_p > f_{Lab}$ and small pin densities, the system is in the lattice strong-pinning regime (3D sp). With increasing n_p, the system first crosses into the single-line strong-pinning regime (1D sp). Further increase of n_p causes another crossover into the single-line collective-pinning regime (1D cp). In the following sections, we discuss the behavior of critical currents in the different parts of this phase diagram, as its importance will be apparent when addressing the critical currents of high-performance superconductors at various magnetic fields.

2.5.1. Collective pinning. In this section, for completeness, we briefly review the collective pinning caused by large numbers of weak pinning centers (Larkin and Ovchinnikov 1979, Blatter *et al* 1994). As mentioned above, a finite pinning force in this case appears due to fluctuations of the disorder potential. The lattice splits into independently pinned regions called Larkin domains. On the scale of the domain, the disorder-induced lattice displacements from the equilibrium positions are of the order of the pinning potential range r_p. The domain size is set by the *Larkin lengths* which are determined by the interplay between disorder fluctuations and elasticity. The key observation is that the softer lattice adjusts more easily to the pinning potential and results in higher critical currents.

We consider first the *single-vortex regime*. A straight vortex can lower its energy by adjusting to the random pinning potential via smooth deformations. If a vortex segment with length L is displaced by a distance r_p, the typical variation of the random energy can be estimated as $\sqrt{N(L)}\,u_p$, where $N(L) = n_p L r_p^2$ is the average number of pins in the volume $L r_p^2$. This gain in the random energy must be compared with the loss of the elastic energy $\varepsilon_1 r_p^2/L$ so that the total variation of energy can be estimated as

$$\delta E(L) = \varepsilon_1 \frac{r_p^2}{L} - \sqrt{n_p L r_p^2}\, u_p. \tag{15}$$

Minimizing this energy with respect to L gives the following estimate for the Larkin length

$$L_{c0} \approx \left(\frac{\varepsilon_1 r_p}{\sqrt{n_p}\, u_p} \right)^{2/3}. \tag{16}$$

The critical current is proportional to the typical random force per unit length acting on the vortex section with length equal to the Larkin length $\sqrt{N(L_c)}\,u_p/r_p L_{c0} = \sqrt{n_p/L_{c0}}\,u_p$ and leads to the following well-known result

$$\frac{\Phi_0}{c} J_c = \frac{\sqrt{n_p}\, u_p}{\sqrt{L_{c0}}} = \left(\frac{n_p^2 u_p^4}{\varepsilon_1 r_p} \right)^{1/3}.$$

The pinning is collective when the volume $L_{c0} r_p^2$ contains many impurities $n_p L_{c0} r_p^2 \gg 1$ giving the following condition

$$n_p \gg \frac{u_p}{\varepsilon_1 r_p^4}.$$

This corresponds to the line separating '1D sp' and '1D cp' regions in the phase diagram, figure 7.

In the *lattice regime*, the Larkin domain has two typical dimensions, one along the field, L_c and the other in the transverse direction, $R_c > a$. Collective pinning estimates for this regime are complicated by the dispersion of the tilt modulus, equation (6). We limit ourselves to the local case when the Larkin length R_c is larger than the London penetration depth. Estimates for the general case can be found, e.g. in the review (Blatter *et al* 1994). As $C_{66} \ll C_{11}$, the lattice adjusts to the random potential mostly by shear deformations. Therefore the typical energy variation due to the displacement of the volume LR^2 by a distance r_p is given by

$$\delta E(L,R) = \left(C_{66} \frac{r_p^2}{R^2} + C_{44}^{(0)} \frac{r_p^2}{L^2} \right) LR^2 - \sqrt{n_p L r_p^2 n_v R^2}\, u_p.$$

Here, the combination under the square root is the total number of pins in the vortex cores within the considered volume and $C_{44}^{(0)} = B^2/4\pi$ is the small-k tilt modulus. Minimization with respect to R and L gives

Table 1. Dependences of the critical current on magnetic field and pin density in different pinning regimes for $B \ll H_{c2}$.

			Strong pinning		
	Collective		Direct collision	Trapping instability	All pins occupied
Single-vortex	$n_p^{2/3}$		$\sqrt{n_p}$	$n_p^{4/9}$	
Lattice	$R_c < \lambda$	$R_c > \lambda$	$n_p/\sqrt{B}$	$n_p B^{-5/8}$	n_p/B
	$\exp(-\alpha B^{3/2}/n_p)$	n_p^2/B^3			

Note: In the strong-pinning regime trappings of vortices by direct collisions with pinning centers or due to instability caused by long-range interactions lead to somewhat different dependences (see text).

$$L_c = \frac{C_{66}C_{44}^{(0)}r_p^2}{n_p n_v u_p^2} \tag{17}$$

$$R_c = \frac{C_{66}^{3/2}\sqrt{C_{44}^{(0)}}\,r_p^2}{n_p n_v u_p^2}. \tag{18}$$

The critical current is determined by the typical random force within the Larkin domain giving the following estimate

$$J_c \approx \frac{c n_v^2 n_p^2 u_p^4}{B C_{66}^2 C_{44}^{(0)} r_p^3}. \tag{19}$$

As $C_{66} \propto B$ and $C_{44}^{(0)} \propto B^2$, the critical current decreases as B^{-3} in this regime. This rapid decrease of J_c is caused mostly by the stiffening of the lattice with increasing magnetic field. In the intermediate regime where $a < R_c < \lambda$ and nonlocality of the tilt stiffness is essential, the collective pinning theory predicts even faster exponential decrease of the critical current with increasing magnetic field, $J_c \propto \exp[-\gamma^3 L_{c0}^3 (B/\Phi_0)^{3/2}]$. The dependences of J_c on B and n_p for the collective pinning are summarized in the table 1.

The ideas of collective pinning are very appealing and play a very important role in condensed-matter physics. On the other hand, a strong-pinning scenario, i.e. pinning by dilute array of strong defects, is more important from a practical point of view. In the next section, we review estimates of critical currents for this scenario.

2.5.2. Strong pinning. For a dilute array of strong defects, pinning occurs via trapping of vortex segments (Ovchinnikov and Ivlev 1991) with typical length L between two pins, as illustrated in figure 8. The critical current is determined by this typical length of the trapped segment L and the pin-breaking force f_p,

$$\frac{\Phi_0}{c} J_c \approx \frac{f_p}{L}. \tag{20}$$

Therefore, in the strong-pinning regime, the critical-current problem is reduced to the evaluation of the trapped-segment length L, which is the result of a complex interplay between the vortex-pin interaction, the line tension and the interaction between the vortex lines.

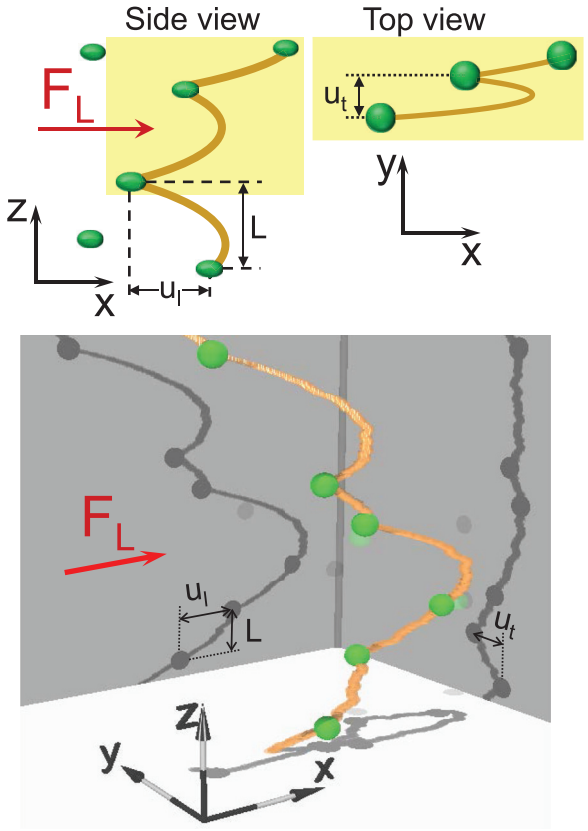

Figure 8. *Upper figures* illustrate a dynamically trapped vortex line (side and top views). The typical displacement in the direction of motion u_l is much larger than the displacement in the transversal direction u_t. *Lower figure* is a visualization of the pinned line configuration obtained from a Langevin dynamics simulation, see section 4.1. Shadow projections on the axis planes illustrate line displacements in the different directions. The definitions of the trapping parameters L and $u_{l,t}$ are also illustrated. (Adapted with permission from Koshelev and Kolton (2011). Copyright (2011) by the American Physical Society.)

Single vortex. In this section, we evaluate the critical current for an isolated vortex interacting with strong pinning centers (Blatter *et al* 2004, Koshelev and Kolton 2011). The motion of the vortex line stops when the driving force drops below the critical value. The following two considerations determine the structure of the pinned vortex line: (i) when the vortex passes near the pinning center, it may be trapped and (ii) the vortex remains trapped as long as the force transmitted by the trapped segment onto the pin does not exceed the pin-breaking force. When a moving vortex line is trapped, the typical trapping distance between the neighboring pins in the direction of motion, u_l, is much larger than the corresponding distance in the transverse direction, u_t, see figure 8. The longitudinal trapping distance, u_l, is determined by the pin-breaking condition,

$$\varepsilon_l \frac{u_l}{L} = f_p. \tag{21}$$

While the transverse displacement between the pins u_t is determined by the condition for trapping. The simplest assumption is that trapping typically occurs when the vortex lines directly collide with the pins (Blatter *et al* 2004) giving $u_t \approx b$. The trapped-segment length L and distances $u_{l,t}$ are connected by the geometrical relation

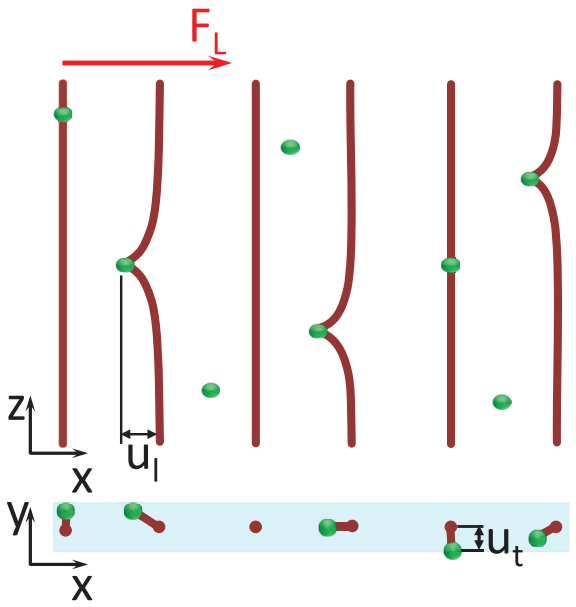

Figure 9. Schematic configuration of one row of the vortex lattice pinned by dilute strong centers. Only pin sites close to the lattice positions are occupied.

$$n_{\rm p} L u_{\rm l} u_{\rm t} = 1 \tag{22}$$

where $n_{\rm p}$ is the pin density. Using the above two equations, we obtain estimates for $u_{\rm l}$ and L

$$u_{\rm l} = \sqrt{\frac{f_{\rm p}}{n_{\rm p}\varepsilon_{\rm l} b}}\,,\quad L = \sqrt{\frac{\varepsilon_{\rm l}}{n_{\rm p} b f_{\rm p}}}\,. \tag{23}$$

This corresponds to the following result for the critical current

$$\frac{\Phi_0}{c} J_{\rm c} = C_j f_{\rm p}^{3/2} \sqrt{\frac{n_{\rm p} b}{\varepsilon_{\rm l}}}\,. \tag{24}$$

with $C_j \sim 1$.

The simplest assumption $u_{\rm t} \approx b$, however, may underestimate $u_{\rm t}$. Due to the long-range pin-vortex interaction (9), a pinning center may capture the vortex line even without direct collisions. Consideration of the trapping instability (Koshelev and Kolton 2011) leads to the following estimate $u_{\rm t} = (\varepsilon_0 L V_{\rm p}/\varepsilon_{\rm l})^{1/4}$. The corresponding estimate for critical current suggests that it should scale with pin density as $J_{\rm c} \propto n_{\rm p}^{4/9}$. However, the numerical simulations (Koshelev and Kolton 2011) actually agree better with the simple estimate (24) and yield the numerical constant, $C_j \approx 1.9$.

Vortex lattice. With increasing magnetic field the interactions between the vortices become important and they start to compete for pinning sites. This leads to a decrease of the critical current with magnetic field. We consider pinning of the vortex lattice by dilute strong pinning sites (Ovchinnikov and Ivlev 1991). In the pinned state at moderate magnetic fields, only pin sites close to the ideal lattice positions are occupied with vortices, see figure 9. These sites are located within the so-called trapping area. As in the single-vortex case, due to its dynamic origin, this area is highly anisotropic. The trapping distance in the direction of motion, $u_{\rm l}$, is much larger than the trapping distance in the transverse direction, $u_{\rm t}$. If we again assume that the vortex line is trapped when it directly collides with the pinsite, then the transverse trapping distance is given by the pin size, $u_{\rm t} \approx b$. The longitudinal distance $u_{\rm l}$ is determined by the condition for detrapping, which is stronly influenced by the vortex interactions. The elastic force acting on a vortex point displaced by a distance u from the equilibrium position is $\bar{C}u$. The spring constant $\bar{C}$ is related to the elastic moduli as

$$\bar{C}^{-1} = \frac{1}{2}\int \frac{{\rm d}^3\mathbf{k}}{(2\pi)^3}\left(\frac{1}{C_{11}(\mathbf{k})k_\parallel^2 + C_{44}(\mathbf{k})k_z^2} + \frac{1}{C_{66}k_\parallel^2 + C_{44}(\mathbf{k})k_z^2}\right) \approx \frac{5}{4}\sqrt{\frac{\Phi_0}{4\pi B\varepsilon_0\varepsilon_{\rm l}}} \tag{25}$$

where the integration over the in-plane wave vector $\mathbf{k}_\parallel$ is performed over the Brillouin zone of the vortex lattice. Therefore, the pinsite can hold the vortex line as long as $u < u_{\rm l} \approx f_{\rm p}/\bar{C}$.

The critical current is related to the trapping area $u_{\rm l}u_{\rm t}$ by

$$\frac{\Phi_0}{c} J_{\rm c} \approx f_{\rm p} n_{\rm p} u_{\rm l} u_{\rm t}. \tag{26}$$

Using the above estimates for $u_{\rm l,t}$, we obtain

$$J_{\rm c} \approx \frac{c n_{\rm p} f_{\rm p}^2 b}{\Phi_0 \bar{C}}. \tag{27}$$

Since $\bar{C} \propto \sqrt{B}$, the critical current in this regime decreases as $1/\sqrt{B}$.

On general grounds, however, we again can expect that the value $u_{\rm t} \sim b$ underestimates $u_{\rm t}$, because the pinsite can trap remote vortices due to the long-range interaction (9). A more elaborate evaluation of $u_{\rm t}$, taking into account the trapping instability (Ovchinnikov and Ivlev 1991) gives $u_{\rm t} \propto a^{1/4}$, which leads to a larger power exponent $J_{\rm c} \propto B^{-5/8}$.

The fraction of pin sites occupied by vortices slowly increases with magnetic field. Above a certain field, all pin sites become occupied, marking the crossover to a new regime. In this regime, one arrives at a simple estimate of the critical current

$$J_{\rm c} = C_{\rm l} c n_{\rm p} f_{\rm p}/B \tag{28}$$

with $C_{\rm l} \lesssim 1$.

We can conclude that the signature of the strong pinning scenario is the existence of two field regimes, where the critical current decays according to a power-law with the exponents ~ 0.5 and 1. Table 1 summarizes dependences of the critical current on magnetic field and pin density for both collective and strong pinning regimes. Note, however, that the high-field estimates presented in this section assume pinning of the regular vortex lattice, which is only justified for low pin density. Currently, there are no good analytical descriptions for the important cases when defects occupy a noticeable volume fraction of the material. However, these cases can be investigated using large-scale numerical simulations, as described below in section 4.

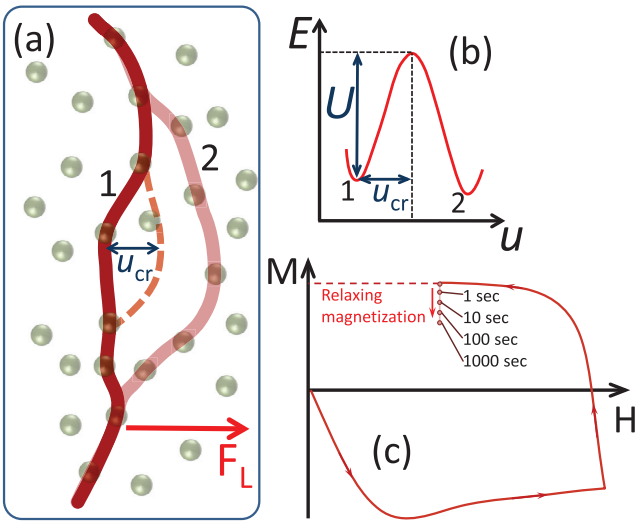

Figure 10. (a) Illustration of two metastable states of a pinned vortex (marked by 1 and 2) separated by the potential barrier U. Jump from the initial state 1 into the next state 2 may occur because of thermal noise. Such a jump is only possible after a rare strong fluctuation in the form of a critical nucleus is generated (dashed line). Slow creep motion of vortices is due to such jumps. (b) The dependence of the energy E on the vortex displacement u from the initial state. (c) Schematic magnetization loop for a strong-pinning superconductor showing pronounced hysteresic behavior. The arrows mark the magnetic-field sweep direction. In the case of strong pinning the equilibrium magnetization is usually small as compared to the hysteretic magnetization. When the applied field is held constant, the magnetization relaxes towards the equilibrium magnetization (vertical red arrow) via vortex creep. The small circles track time evolution of the relaxed magnetization.

2.6. Thermal creep

A key property of the pinned vortex state is the existence of multiple metastable states that are separated by potential barriers, see figures 10(a) and (b). At finite temperatures, the vortex lattice can move between these states via rare thermally activated jumps. As a consequence, vortices can move even for currents below the nominal critical current. This slow motion is known as vortex *creep*. The average vortex velocity v and voltage are determined by the creep barrier U which depends on current and magnetic field, $v \propto \exp[-U(B,J)/k_BT]$. In addition, U also decreases with temperature due to the temperature dependence of the superconducting parameters. The creep barrier is determined by the size and shape of the critical nucleus for the typical metastable state which is necessary to trigger a single jump event, see figure 10. The critical nucleus may contain a single vortex or several vortices (vortex bundle). The key property of the glass states is the divergence of the barriers for $J \to 0$, which is caused by the growth of the critical nucleus with decreasing current (Blatter *et al* 1994). The collective creep theory (Feigel'man *et al* 1989, Blatter *et al* 1994) suggests a power-law divergence of the creep barrier,

$$U(J) = U_0(J_c/J)^{\mu} \tag{29}$$

where the index μ depends on the creep regime ($\mu = 1/7$ for single-line creep, $\mu = 3/2$ for bundles smaller that the London penetration depth λ, and $\mu = 7/9$ for bundles larger than λ).

Experimentally, creep manifests itself in the time decay of the irreversible magnetization $M(t)$ (see figure 10(c)). This magnetization is proportional to the persistent current J flowing in the sample, $M(t) \propto J(t)$, which relaxes due to slow motion of the vortices with the relaxation rate being determined by the creep barrier, $\mathrm{d}J/\mathrm{d}t \propto -\exp[-U(J)/k_BT]$. For small changes of the persistent currents, one can expand the barrier (but not the exponent!), $U(J) \approx U_0 + \mathrm{d}U/\mathrm{d}J[J(t) - J(0)]$ with $\mathrm{d}U/\mathrm{d}J < 0$. Such approximation gives a logarithmic time dependence of the magnetization (Anderson and Kim 1964), $[M(t) - M(0)]/M(0) = -S\ln(t/t_0)$, where the creep rate S is related to the barrier $U(J)$ as

$$S = -\frac{k_BT}{J}\left(\frac{\mathrm{d}U}{\mathrm{d}J}\right)^{-1}. \tag{30}$$

This logarithmic law holds as long as the relative changes of the magnetization are small.

Due to the large amplitude of thermal fluctuations, thermal creep in HTSs is much stronger than in conventional superconductors (Yeshurun *et al* 1996). In the typical HTS creep experiment, the initial persistent current is already relaxed to values which are much smaller than the nominal pre-creep critical current. This experimental persistent current is determined by the condition $U(J) = C_Tk_BT$, where $C_T \approx \ln(t_{exp}/t_0) \sim 20$–$30$ is a large constant which is determined by the macroscopic time scale needed to prepare the initial state, $t_{exp} \sim 10$–30 s, and the microscopic time related to the attempt frequency, $t_0 \sim 10^{-8} - 10^{-6}$ s. This means that for the power-law barrier (29) the creep rate (30) can be estimated as $S = 1/(\mu C_T)$ and only weakly depends on temperature. This reasoning naturally explains the temperature dependence of the creep rate which typically exhibits a wide plateau where $S = 0.02$–0.04 (Yeshurun *et al* 1996). An interpolation formula was proposed to describe the low-temperature region, where creep has only a small influence on the apparent critical current (Malozemoff and Fisher 1990),

$$S = k_BT/[U_0 + \mu k_BT\ln(t_{exp}/t_0)]. \tag{31}$$

This formula qualitatively describes the behavior of creep rates in high-temperature superconductors.

In general, for multiple defects, the current dependence of the creep barrier may not have a simple form. The magnetic-relaxation data for different temperatures may be used to restore the current dependence of the creep barrier. A well-known method for such restoration is the Maley analysis (Maley *et al* 1990), which is based on the observation that as $|\mathrm{d}M/\mathrm{d}t| = C_M\exp(-U/k_BT)$, the barrier U can be expressed by

$$U = -k_BT\ln(|\mathrm{d}M/\mathrm{d}t|) + k_BT\ln C_M. \tag{32}$$

The current-dependent barrier can be obtained by plotting $k_BT\ln|\mathrm{d}M/\mathrm{d}t|$ versus $M \propto J$ for different temperatures and selecting the factor $\ln C_M$ so that all pieces collapse into a single curve. The higher-temperature pieces provide the lower-current regions of the dependence $U(J)$. Strictly speaking, this procedure only works if the explicit temperature dependence of the barrier can be neglected. This is a reasonable approximation for $T < T_c/2$. One can take into account the temperature

dependence of the barrier if it can be represented in a simple factorizable form (Polat *et al* 2011), $U(J, T) = U(J, 0)G(T)$. In this case equation (32) can be modified as

$$U(J,0) = \frac{-k_B T \ln(|\mathrm{d}M/\mathrm{d}t|) + k_B T \ln C_M}{G(T)}. \tag{33}$$

This approach is justified if a reasonably simple functional form of $G(T)$ provides a good collapse of the different-temperature pieces into a single smooth curve, as it was found for $G(T) = (1 - T/T_c)^2$ in Polat *et al* (2011).

Alternatively, one can restore the barrier directly from the temperature-dependent creep rate $S(T)$. Using the relation $U(J) = C_T k_B T$ together with equation (30) results in the following relation

$$\ln\left(\frac{J(T)}{J(T_0)}\right) = C_T \int_{T_0}^{T} S(T')\frac{\mathrm{d}T'}{T'} \tag{34}$$

where numerical evaluation of the integral on the left-hand side, followed by replacement $T \to U/C_T k_B$ gives implicitly the current-dependent barrier.

In addition to relaxing the hysteretic magnetization, vortex creep strongly influences the transport properties. Since a finite voltage exists for all applied currents, the critical current at finite temperature does not have an exact meaning and is sensitive to the voltage criterion which is used to define it. Due to the high creep rates in HTSs, the apparent critical current is typically strongly suppressed by vortex creep. In fact, the commonly-used criterion for the determination of critical current in transport measurements, $E \sim 1\ \mu\mathrm{V\ cm}^{-1}$, corresponds to the creep regime where the voltage is mostly determined by the barrier $U(J)$, $E \propto \exp[-U(J)/k_B T]$. In this range of currents, the common experimental way to describe the shape of the current–voltage (IV) dependences is to fit them to a power law $E \propto J^n$ with the temperature dependent exponent $n \gg 1$. If the power-law dependence would hold in the entire range of currents, it would correspond to the logarithmically diverging barrier, $U = U_0 \ln(J_c/J)$ and $n = U_0/k_B T$. A fit of a simple power-law to the current is usually only possible within a narrow current interval. More precisely, the exponent n has to be interpreted as the logarithmic derivative $n = \mathrm{d}\ln E/\mathrm{d}\ln J$ at the current where the fit is done. In this case n is related to the creep rate as $n \approx 1/S$. The typical voltages probed in transport measurements are 5–6 orders of magnitude larger than voltages probed in magnetization relaxation measurements meaning that these experiments explore very different parts of the current–voltage curve and give the creep barrier $U(J)$ for different currents.

The most prominent consequence of large creep in high-temperature superconductors is the strong suppression of the apparent critical current. Therefore, mitigating vortex creep is one of the most important routes to enhance the practical current-carrying capabilities of HTS materials.

2.7. Columnar defects

Extended one-dimensional defects with lateral sizes larger than the coherence length are the most efficient pinning centers for small magnetic fields aligned with them because such defects are capable of trapping individual vortices over their entire length. Examples of physical realizations of one-dimensional defects are dislocations, heavy-ion irradiation tracks, and self-assembled nanorods. The latter two will be described in more detail in the following sections. The density of columnar defects, n_d, is commonly characterized by the dose-matching field $B_\Phi = \Phi_0 n_d$, where at $B = B_\Phi$ there is one columnar defect per vortex line. In this section we only discuss the relatively simple case of a small magnetic field $B < B_\Phi$. Behavior at high magnetic fields is considered in Blatter *et al* (1994).

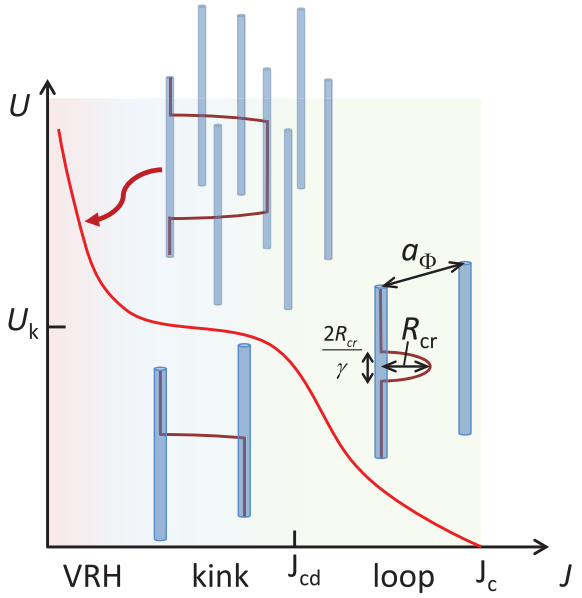

Figure 11. The schematic current dependence of the creep barrier for an array of parallel columnar defects in the case of an isolated vortex line. The crossovers between vortex loop, kink and variable-range hopping (VRH) regimes are illustrated.

For a single vortex line pinned by a cylindrical insulating defect with radius $b > \xi$ the pinning energy per unit length, $U_p = \epsilon_0 \ln(b/\xi)$, is comparable with the line energy ϵ_l. In this case the critical current J_c required to tear the vortex line away from the defect at low temperatures is close to the depairing current J_{dp}. At finite temperatures, the vortex line can escape from the columnar defect for $J < J_c$. To overcome the barrier, a critical nucleus has to be formed. For an isolated defect, the critical nucleus has the shape of an elliptical vortex half loop with the vertical semi-axis γ times smaller than the horizontal semi-axis, as illustrated in figure 11. The energy of such a half loop contains contributions from the loss of pinning energy, elastic tension, and interaction with the current

$$U_{\mathrm{loop}}(R) \approx \epsilon_0 \frac{R}{\gamma} \ln\frac{b}{\xi} + \pi\frac{\epsilon_0}{\gamma} R \ln\frac{R}{\xi} - \frac{\Phi_0}{c}\frac{\pi R^2}{2\gamma} J,$$

where R is the horizontal size of the half loop. The barrier is given by the maximum of $U_{\mathrm{loop}}(R)$, which corresponds to the critical half loop. We can see that for $R \gg b$ the pinning-energy term is smaller than the elastic-tension term and can be neglected. Finding the maximum gives the critical size of the half loop

$$R_{\rm cr} \approx \frac{c\epsilon_0}{\Phi_0 J} \ln \frac{R_{\rm cr}}{\xi}$$

and the barrier

$$U(J) = \frac{\pi c \epsilon_0^2}{2\Phi_0 \gamma J} \left(\ln \frac{R_{\rm cr}}{\xi} \right)^2, \tag{35}$$

which in this regime increases as $1/J$.

The critical half-loop size $R_{\rm cr}$ increases with decreasing current. For a finite density of columns, $R_{\rm cr}$ becomes comparable with the typical distance between the columns a_Φ at the current

$$J_{cd} \approx \frac{c\epsilon_0}{\Phi_0 a_\Phi} \ln \frac{R_{\rm cr}}{\xi}$$

marking the crossover to a new vortex kink regime. Below this current, the vortex lines move by forming kinks between neighboring columnar defects, see figure 11. These kinks then freely slide along the column direction. The barrier in this regime is given by the kink energy

$$U_{\rm k} \approx \frac{\epsilon_0 a_\Phi}{\gamma} \ln \frac{a_\Phi}{\xi}, \tag{36}$$

which depends only weakly on the current. These sliding kinks significantly reduce the pinning efficiency of the columnar defects, since they allow for sliding vertical motion.

The kink mechanism assumes that the pinning energies of all columnar defects are identical and therefore it is always energetically favorable to transfer a vortex to the neighboring column in the direction of the Lorentz force. In reality, however, there are always small variations of the pinning energies from defect to defect, $\delta U_{\rm p}$. One reason for such variations is the long-range interaction between columns and vortices. At sufficiently small current, $\Phi_0 J/c < \delta U_{\rm p}/a_\Phi$, these variations become essential. At small currents the vortex line cannot simply jump to the neighboring defect but must find a remote optimal column which has a lower energy (Blatter *et al* 1994). This regime of motion is somewhat similar to the Mott variable-range hopping mechanism in disordered semiconductors. Estimates based on the same qualitative arguments (Blatter *et al* 1994) yield a barrier which diverges with decreasing current as $U \propto J^{-1/3}$. This divergence implies a glassy ground state of the system which is called the Bose glass (Nelson and Vinokur 1993).

As the creep rate is proportional to the inverse derivative of $U(J)$, equation (30), figure 11 suggests the occurrence of a pronounced maximum in S at the temperature $T_k \approx U_k/C_T$ in the kink-dominated regime. Creep measurements (Thompson *et al* 1997) on YBCO crystals that have been irradiated with heavy ions to create columnar defects indeed reveal a strong maximum in $S(T)$ near 20 K, a temperature at which the circulating currents tune the system into the kink-regime.

2.8. Benefits of mixed pinning landscapes

In previous sections we considered model systems when only one type of pinning center was present. Real materials typically have multiple defects differing in dimensionality and size. A quantitative description of such mixed pinning landscapes is not available. In many situations, effects of several types of defects on the vortices are not additive, and some examples will be discussed in section 4.2.

On general grounds, one may expect that combining different defects can improve pinning efficiency and suppress creep. In several cases, the benefits of combining different defects are straightforward. For example, for parallel columnar defects, dissipation may be significantly enhanced due to mobile vortex kinks formed between neighboring columns. These kinks may be pinned by adding pointlike defects leading to the suppression of vortex creep within some current range (Maiorov *et al* 2009), see figure 12(a). On the other hand, point defects can reduce the kink energy and facilitate

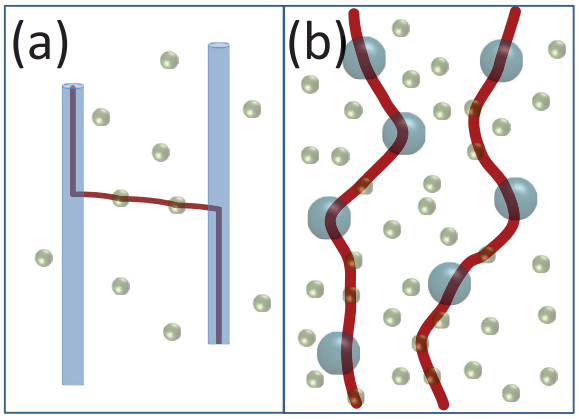

Figure 12. Examples of mixed-pinning landscapes: (a) columnar and pointlike defects with pinned vortex kink and (b) two types of spherical inclusions.

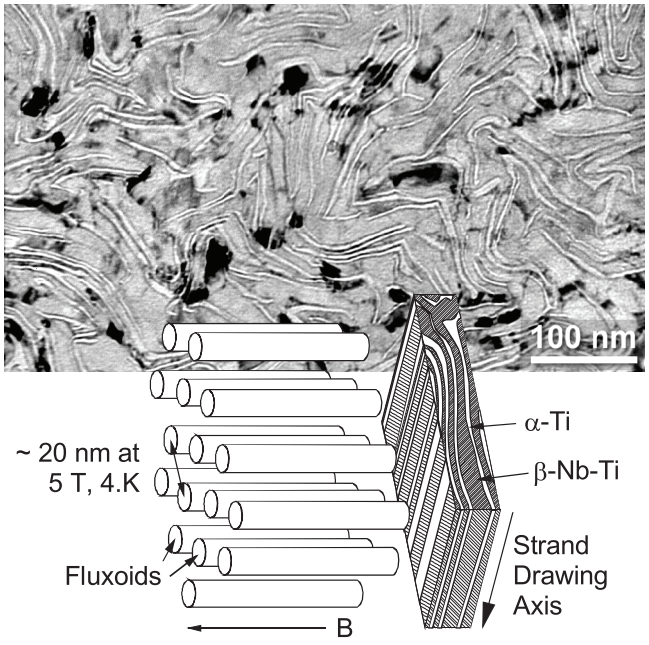

Figure 13. Microstructure of NbTi consisting of α-Ti lamellae (white) and superconducting β-NbTi (grey). The schematic highlights the match between the pin sites and vortices in a field of 5 T at 4 K (taken from Lee and Larbalestier (2001)).

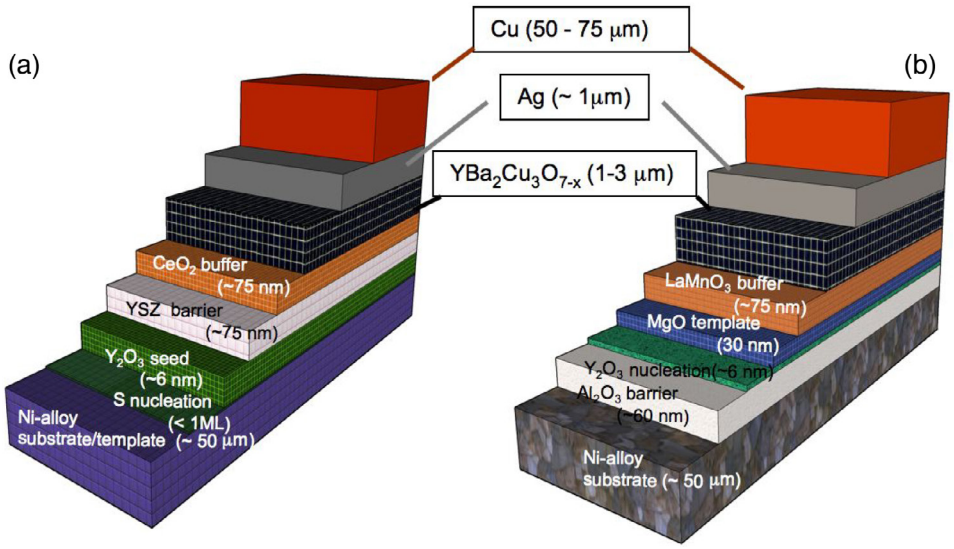

Figure 14. Schematics of the layered structure of REBCO coated conductors. Various buffer layers and diffusion barriers are deposited onto flexible metal substrates. The superconducting REBCO layer, typically 1–2μm in thickness, is grown onto the buffer layers and covered with a silver cap layer for protection. Electro-deposited Cu-layers serve for thermal stabilization of the conductors. (a) Rolling-assisted biaxially textured substrates (RABiTS) (b) Ion-beam-assisted deposition (IBAD) (taken from US Dept. of Energy (2006)).

kink formation. Finding the optimal point-defect parameters in this situation is not a trivial problem.

It also may be beneficial to combine defect inclusions with different sizes, see figure 12(b). Small-size defect inclusion can pin segments of free-vortices traversing between large defect particles and further enhance the critical current. Moreover, defects with a fixed size may be most efficient within certain magnetic field range, as demonstrated directly by numerical simulations (Koshelev *et al* 2016) described in section 4.2. As a consequence, for pinning landscapes composed of inclusions with a spread in size, one can expect a weaker decrease of the critical current with increasing magnetic field. Samples containing two types of pointlike defects have been prepared using proton (Jia *et al* 2013) or oxygen-ion irradiation on HTS films containing self-assembled nanoparticles, as described in section 3.2. A combination of different pinning sites may be the most probable route to the ultimate optimization of the critical current.

3. Tailoring pinning landscapes

3.1. High-performance superconductors

A major emphasis of applied superconductor research is devoted to the creation of the most effective pinning microstructure for a particular magnetic field and temperature environment. A well-known example for this approach is the fabrication of NbTi-wires. A sequence of heating and extrusion/drawing steps results in a microstructure composed of nm-scale α-Ti lamellae embedded in the superconducting β-NbTi phase (Lee and Larbalestier 2001) (figure 13). The dimensions of the α-Ti inclusions and their density match well with the superconducting coherence length and the vortex density in magnetic fields of several Tesla. NbTi-wires are fabricated on the industrial scale with great control and predictability; they are the workhorse for the vast majority of present superconducting applications.

The high-temperature superconducting cuprates and the iron-based superconductors are not amenable to the traditional approaches of alloying and drawing. Furthermore, the detrimental effects of grain boundaries in Fe-based SCs (Lee *et al* 2009, Katase *et al* 2010, 2011, Durrell *et al* 2011) and particularly in cuprates (Dimos *et al* 1988, 1990, Hilgenkamp and Mannhart 2002) necessitate new conductor architectures. A conductor lay-out that is scalable to industrial levels and has yielded the highest critical current densities, J_c, to date is the so-called coated conductor (CC) geometry schematically shown in figure 14. Various industrial approaches, which differ in substrate material and substrate treatment, composition of buffer layers and superconductor deposition methods, have been demonstrated (Senatore *et al* 2014); however, all share the overall rationale to grow essentially epitaxial superconducting films on flexible metallic substrates. Most work on coated conductors has been devoted to YBCO, or more generally REBCO (RE = rare earth), conductors (Malozemoff 2012, Shiohara *et al* 2012, Obradors and Puig 2014, Senatore *et al* 2014).

'Pristine' REBCO films contain a variety of defects that can serve as vortex pin sites (Foltyn *et al* 2007) such as point defects, dislocations, stacking faults or twin boundaries. However, critical currents are not sufficient for high-power applications. Additional pin sites are typically introduced into the REBCO matrix by tuning precursor chemistry and growth conditions such that non-superconducting precipitates of various sizes and shapes appear during the growth process that provide strong pinning (Matsumoto and Mele 2009, Obradors *et al* 2012). A wide variety of synthesis strategies has been developed including *in situ* deposition (i.e. pulsed laser deposition (PLD)) in which deposition and phase formation occur in one step, or *ex situ* deposition (i.e. solution growth or metal-organic deposition(MOD)) in which several

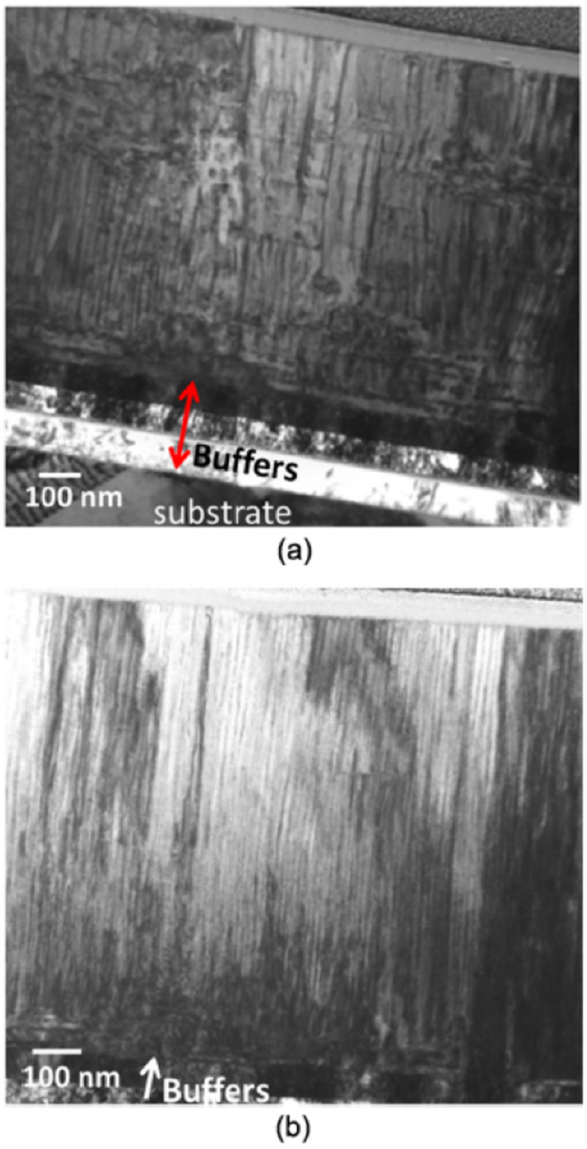

Figure 15. Transmission electron microscopy cross sections of REBCO coated conductors containing BZO nanorods (dark grey vertical lines). (a) shows BZO nanorods that are disrupted by other crystal defects such as stacking faults, whereas in (b) growth conditions have been optimized to yield nanorods that extend through the entire superconductor. The buffer layers and the substrate are indicated (Reprinted with permission from Selvamanickam *et al* (2015d). Copyright 2015, IOP Publishing Ltd.).

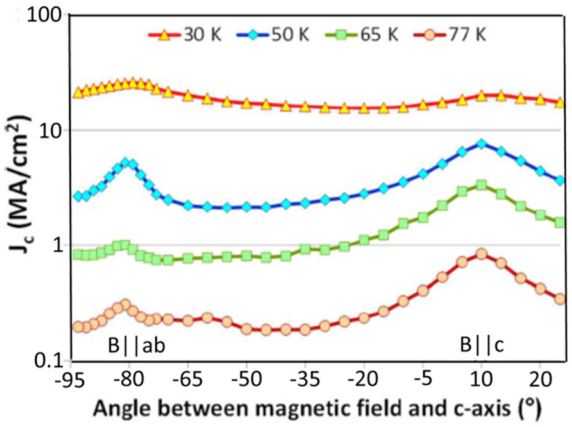

Figure 16. Field angle dependence of the critical current density of a REBCO coated conductor containing 25 mol.% Zr in a field of 3 T and at various temperatures. At high-temperatures a pronounced maximum in J_c around the *c*-axis due to pinning by *c*-axis oriented BZO nanorods is evident whereas at low temperatures J_c becomes almost angle independent (Reprinted with permission from Selvamanickam *et al* (2015a). Copyright 2015, AIP Publishing LLC.).

steps are required. For an extensive review we refer the reader to Obradors *et al* (2011). Significant enhancements of J_c have been achieved with the incorporation of RE_2O_3 (Rupich *et al* 2004, Gapud *et al* 2005), $YBa_2Cu_3O_5$ (Haugan *et al* 2004), $BaZrO_3$ (MacManus-Driscoll *et al* 2004, Gutierrez *et al* 2007, Miura *et al* 2011) nanoparticles.

A major advance in the synthesis of high-performance REBCO coated conductors was the discovery that under certain deposition conditions the addition of excess metal oxides such as $BaZrO_3$ (Goyal *et al* 2005, Kang *et al* 2006, Maiorov *et al* 2009, Xu *et al* 2012, Horide *et al* 2013, Selvamanickam *et al* 2013, 2015a, 2015c, 2015d, Xu *et al* 2014, Abraimov *et al* 2015), $BaSnO_3$ (Mele *et al* 2008) or $BaHfO_3$ (Awaji *et al* 2015) results in the formation of self-assembled nanorods largely oriented along the *c*-axis of the YBCO structure with lengths of hundreds of nm and diameters of ∼10 nm. Figure 15 shows transmission electron microscopy (TEM) images of a REBCO film containing $BaZrO_3$ nanorods. Their geometry makes them ideal pinning sites, particularly in aligned magnetic fields, and indeed, in recent years remarkable advances in performance of research-scale REBCO CCs has been achieved by increasing the Zr-content (Selvamanickam *et al* 2013, Xu *et al* 2014, Abraimov *et al* 2015, Selvamanickam *et al* 2015a, 2015c, 2015d) and perfecting the structure of the BZO nanorods (Selvamanickam *et al* 2015d). Strong pinning by correlated, i.e. anisotropic, pinning sites, such as these BZO nanorods, leaves characteristic fingerprints in the angular dependence of J_c, $J_c(\theta)$. As an example, figure 16 displays $J_c(\theta)$ of a 25 mol.% Zr REBCO coated conductor in a field of 3 T (Selvamanickam *et al* 2015a). At 77 K, a dominant broad maximum in $J_c(\theta)$ for fields applied around the *c*-axis identifies pinning by the BZO nanorods, whereas a smaller maximum for in-plane fields is caused by pinning due to the layered crystal structure (intrinsic pinning) and *ab*-oriented defects such as stacking faults or $YBa_2Cu_3O_5$ precipitates. With decreasing temperature, the maximum in $J_c(\theta)$ due to BZO nanorods becomes less pronounced, and the overall anisotropy of J_c, that is, the ratio of the maximum and minimum values in $J_c(\theta)$, decreases, until at 30 K $J_c(\theta)$ is almost independent of angle. The strong isotropic pinning seen in figure 16 at low temperatures has been attributed to the presence of nanoparticles residing between the nanorods (Abraimov *et al* 2015, Selvamanickam *et al* 2015a) and to strain fields (Gutierrez *et al* 2007, Xu *et al* 2012) as the lattice mismatch between $BaZrO_3$ and REBCO is large, ∼8%. Extensive work on solution-grown YBCO films has shown that strain-fields associated with nano-particles can give rise to strong isotropic pinning (Gutierrez *et al* 2007, Puig *et al* 2008, Llordés *et al* 2012). The angular dependence of J_c is an

Figure 17. Cross-sectional TEM image of a $Ba(Fe_{1-x}Co_x)_2As_2$ film grown on a LSAT/STO substrate. The vertical lines are self-assembled *c*-axis oriented $BaFeO_2$ nanorods. The inset shows an electron diffraction pattern revealing the crystalline structure of the film. (Reprinted with permission from Zhang *et al* (2011). Copyright 2011, AIP Publishing LLC.)

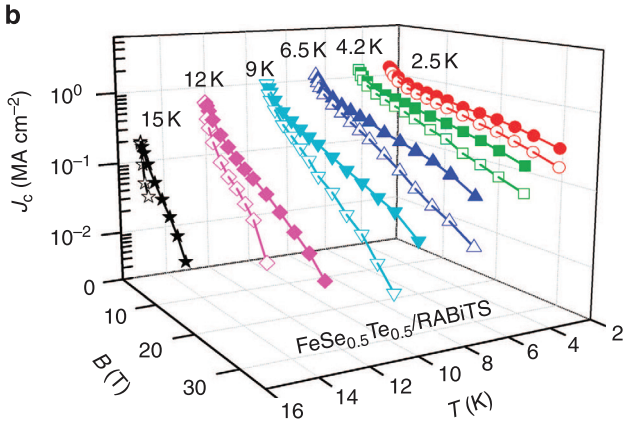

Figure 18. Magnetic field dependence at different temperatures of the critical current density for a $FeSe_{0.5}Te_{0.5}$ film grown on a RABiTS substrate. Open and closed symbols correspond to magnetic fields applied along the *c*-axis and parallel to *ab* plane, respectively. (Reprinted figure with permission from Macmillan Publishers Ltd: Si *et al* (2013) (figure 3b). Copyright (2013).)

important characteristic, since in applications, such as solenoids or motors, the magnetic field acting on the conductors varies in size and orientation. Thus, it is the smallest value of $J_c(\theta, H)$ that ultimately limits the performance, and the evolution shown in figure 16 is highly desirable. These data are also an example of a mixed-pinning landscape in which defects with different pinning characteristics are combined in synergistic ways to yield optimum performance. Here, the mixed-pinning landscape represents a combination of figures 5(b) and (d). In short-length samples of highly doped REBCO conductors, critical current densities as high as $\sim$7 MA cm^{-2} at 30 K and 9 T applied parallel to *c*-axis have been reported (Selvamanickam *et al* 2015a, 2015c, 2015d); or, as recently pointed out (Haugan 2015): the performance of these new samples at 50 K roughly equals that of current 7.5%-Zr commercial production line conductors at 4.2 K. The transfer of these advances into a reliable large-scale production process is a time consuming process currently being pursued.

The recently discovered iron-based superconductors (Kamihara *et al* 2008, Rotter *et al* 2008, Johnston 2010, Hosono and Kuroki 2015) display materials characteristics that make them very appealing for potential applications (Shimoyama 2014, Hosono *et al* 2015, Ma 2015). Their reasonably high values of the superconducting transition temperature, very high upper critical magnetic fields, and generally low anisotropy enable operation in economically interesting temperature-field ranges and, at the same time, minimize thermal fluctuations that affect the cuprate superconductors (Gurevich 2011, 2014). Thus, approaches that have proven so effective for the cuprates have also been applied to Fe-based superconductors. For example, $BaFe_2(As_{0.66}P_{0.33})_2$ films containing BZO nanoparticles were synthesized using pulsed laser deposition onto MgO substrates from a BZO-doped target (Miura *et al* 2013). On these samples, enhanced irreversibility fields and enhanced critical currents over the entire field and angular range were observed. O-rich starting materials have yielded the growth of c-aligned $BaFeO_2$-nanorods on $SrTiO_3$ (STO) templated $(La,Sr)(Al,Ta)O_3$ (LSAT) substrates, which induce strongly enhanced J_c, particularly for *c*-axis fields (see figure 17(a)) (Lee *et al* 2010, Zhang *et al* 2011, Tarantini *et al* 2012). The formation of the nanorods is attributed to a compressive strain mismatch between the $BaFeO_2$ and the $SrTiO_3$ buffer layer. Recently, coated conductors based on $Ba(Fe_{1-x}Co_x)_2As_2$ (Iida *et al* 2011, Trommler *et al* 2012a, 2012b), $FeSe_{0.5}Te_{0.5}$ (Si *et al* 2011, 2013) and NdFeAs(O,F) (Iida *et al* 2014) on flexible metal substrates have been fabricated. These conductors have displayed promising high-field performance. For instance, on $FeSe_{0.5}Te_{0.5}$ film with $T_c \approx 18$ K, J_c values of ≈ 0.1 MA cm^{-2} in magnetic fields of 30 T along the *c*-axis have been reported, see figure 18.

3.2. Defect formation via particle irradiation

The synthesis of desired pinning structures such as nanorods requires carefully tuned chemistry and growth parameters. However, their stable implementation for industrial fabrication of long-length conductors has proven a challenge. Furthermore, the growth of nanorods is not a practical option for solution-grown REBCO films. An alternative to modifying the chemical synthesis in order to generate the desired pinning structure is afforded by particle irradiation, which is a generic technique applicable to all superconducting materials. Depending on the mass and energy of the ions and the properties of the target material, irradiation enables the creation of defects with well-controlled density and topology, such as points, clusters or tracks. Irradiation of superconductors to induce tailored defects to raise their critical current has so far remained in the realm of fundamental research. However, recent studies have shown that rapid reel-to-reel irradiation of post-production commercial coated-conductors may actually be a viable option for creating uniform pinning structures over long length (Rupich *et al* 2015).

An important parameter describing radiation damage is the spectrum of recoil energies imparted by the incoming particle on the primary knock-on atom (Kinchin and Pease 1955, Robinson and Torrens 1974, Averback *et al* 1978, Robinson 1994). If this energy exceeds the threshold energy describing

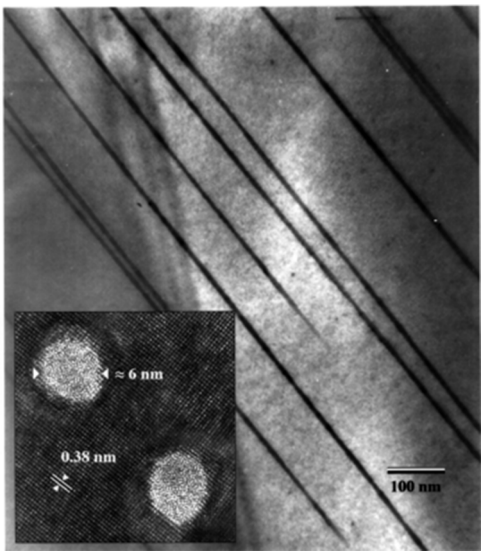

Figure 19. Transmission electron microscopy cross section of irradiation tracks in an YBCO single crystal due to 1.4 GeV Pb-ions. The inset shows a plan view of the tracks (courtesy Wheeler and Kirk).

the binding of the atom to its lattice site, typically tens of eV, the atom will be displaced leaving a vacancy behind. If the recoil energy is high enough, the displaced atom itself can displace another atom and so on until the recoil energy drops below the threshold, resulting in collision cascades. For well-separated displacement events a linear cascade arises, whereas energetic incoming particles in dense target materials cause overlapping collisions and a thermal spike (Ziegler and Biersack 1985, Averback and de la Rubia 1997, Nordlund *et al* 1998, Krasheninnikov and Nordlund 2010). Typically, thermal spikes produce a predominance of vacancies near the core and interstitials at the periphery. Owing to their small mass, irradiation with electrons generally produces point defects in the form of pairs of vacancies and interstitials separated by a few inter-atomic distances. In contrast, irradiation with MeV protons, neutrons and light ions produces recoils with energies of tens of keV and thus a mix of point defects and linear and thermal spike cascades is expected. In addition, vacancies may migrate at elevated temperatures to form clusters in the form of dislocation loops (Jäger and Merkle 1988). While point defects cannot be imaged in TEM, anisotropic clusters and cascades with sizes of 2–4 nm have been imaged by TEM on proton and neutron irradiated YBCO crystals (Kirk 1993, Kirk and Yan 1999). The final defect structure is also dependent on pre-existing defects, which may serve as sinks for irradiation-induced defects, or promote their migration and recombination (Vlcek *et al* 1993).

The irradiation with energetic (hundreds of MeV to GeV) heavy ions (such as Pb, Au, Xe, U) produces extended defects (Fleischer *et al* 1965). Depending on the electronic energy transfer per travel distance, energy and mass of the projectile as well as parameters of the target material (thermal and electrical conductivity, specific heat) continuous or discontinuous amorphous irradiation tracks can be created along the projectile path as a consequence of Coulomb explosion and thermal spike (Toulemonde *et al* 1994, Bringa and Johnson 2002, Lang *et al* 2015). Figure 19 shows TEM images of irradiation tracks in YBCO due to 1.4 GeV Pb-ions. Extensive electron microscopy work on irradiation tracks in YBCO has shown that the tracks are surrounded by additional damage in the form of strain fields, micro-twinning, oxygen deficiency and possibly stacking faults (Zhu *et al* 1993, Yan and Kirk 1998).

Irradiation with electrons, protons, neutrons, alpha particles, and light and heavy ions of various energies has been extensively utilized to generate vortex pinning sites and to probe the superconducting ground state, most notably in cuprates (Clark *et al* 1987, Umezawa *et al* 1987, Clark *et al* 1988, Iwase *et al* 1988, White *et al* 1988a, 1988b, Willis *et al* 1988, Xiong *et al* 1988, Roas *et al* 1989, Civale *et al* 1990, Civale *et al* 1991, Hardy *et al* 1991, Konczykowski *et al* 1991, Thompson *et al* 1992, Schuster *et al* 1993, Civale 1997, Swiecicki *et al* 2012) such as YBCO and in iron-based superconductors (Brandt 1995, Eisterer *et al* 2009, Nakajima *et al* 2009, 2010, Kim *et al* 2010, Prozorov *et al* 2010, Fang *et al* 2011, 2012, 2013, Maiorov *et al* 2012, Tamegai *et al* 2012, Kihlstrom *et al* 2013, Murphy *et al* 2013, van der Beek *et al* 2013, Yeninas *et al* 2013, Salovich *et al* 2013, Mizukami *et al* 2014, Prozorov *et al* 2014, Haberkorn *et al* 2015a, Massee *et al* 2015).

Particle irradiation creates defects on random arrays whose average density can be controlled via the irradiation dose whereas the morphology of the defect (points, cascades and their size, linear tracks) can be controlled by the choice of the incoming particle. Furthermore, irradiation allows combining defects with different characteristics or adding to already existing ones at densities that are interesting for vortex pinning. This occurs without changing the chemistry of the sample thereby controllably creating mixed-pinning landscapes that are very effective in vortex pinning. This potential is highlighted in figure 20 showing the enhancement of the critical current density of REBCO coated conductors following irradiations with heavy ions, protons, and combined proton and heavy-ion irradiation. Even though the pristine sample displays a sizable zero-field J_c of 20 MA cm^{-2} (figure 20(a)), irradiation-induced pinning results in substantial additional enhancements of the *in-field* J_c. Heavy-ion induced tracks yield the strongest J_c enhancement in moderate field around 2 T, whereas *p*-irradiation induced defects are most effective in high fields. Thus, their synergistic combination results in a doubling of J_c over a large field range.

Irradiation of single crystal samples with rather low initial pinning generally yields substantial enhancements of J_c over wide ranges in applied magnetic field and temperature. However, it is *a priori* not obvious what the effect of particle irradiation will be on high-performance coated conductors that already contain optimized pinning microstructures. Below we highlight both limits with examples of industrial REBCO coated conductors and $Ba_{0.6}K_{0.4}Fe_2As_2$ crystals.

3.3. Cuprate coated conductors

Only recently has the potential for improving the performance of coated conductors through particle irradiation been recognized (Matsui *et al* 2012, Jia *et al* 2013, Leonard *et al* 2013a,

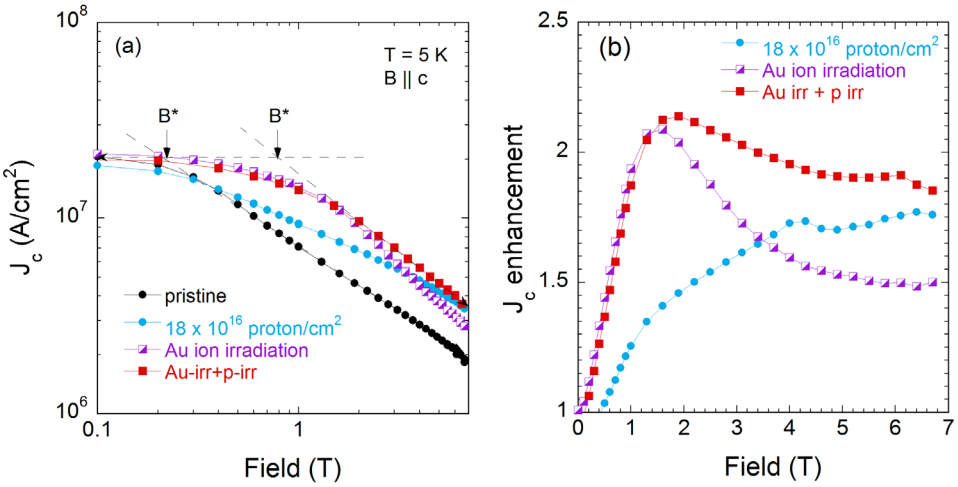

Figure 20. (a) Magnetic field dependence of J_c at 5 K of REBCO coated conductors in the pristine state and following irradiations with 250 MeV gold ions to a dose matching field of 3 T, with 3 MeV protons to a dose of 18×10^{16} p cm^{-2}, and combined proton and heavy-ion irradiation to doses 4×10^{16} p cm^{-2} and 3 T, respectively. The arrows mark the cross-over field B^* between an almost field independent J_c and a power-law decay. (b) Corresponding magnetic field dependence of J_c enhancement.

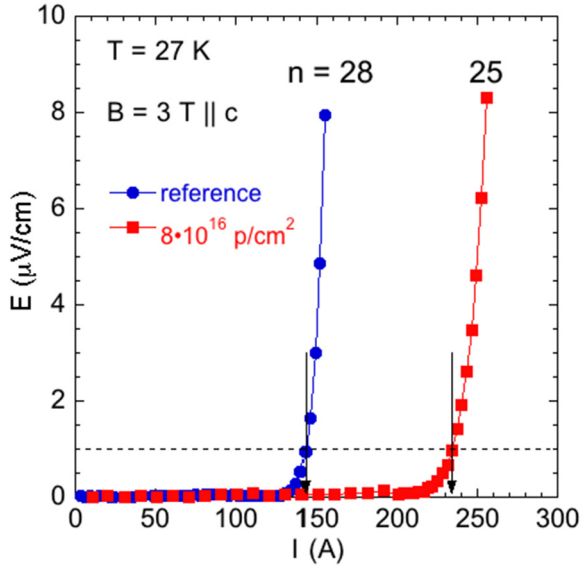

Figure 21. Current–voltage curves at 27 K in a *c*-axis field of 3 T of REBCO coated conductors patterned in 2.5 mm wide bridges. Data for a pristine sample and a proton-irradiated sample reveal the strong increase of the critical current upon irradiation. The *n*-values describing the shape of the IV-curves are indicated (Reproduced with permission from Jia *et al* (2013). Copyright 2013, AIP Publishing LLC.).

2013b, 2014, Matsui *et al* 2014, Gapud *et al* 2015, Haberkorn *et al* 2015b, Leroux *et al* 2015, Prokopec *et al* 2015, Rupich *et al* 2015). In particular, it was demonstrated (Jia *et al* 2013) that the in-field critical current density of production-line coated conductors can be doubled using irradiation with 4 MeV protons. Figure 21 displays a comparison of the electric field versus current (E-I) curves at 27 K and 3 T || c for the reference sample and a sample irradiated to a fluence of 8×10^{16} p cm^{-2}. The almost parallel shift of the curves reveals a substantial increase of I_c from 143.6 A to 234.5 A. At the same time, the E-I curves hardly broaden as evidenced by the slight decrease of the *n*-value (in $E \sim I^n$) from 28 for the reference sample to 25 for the irradiated sample demonstrating that the sample does not degrade upon proton irradiation (see below). At the same time, the suppression of T_c amounts to only ~1.5 K after a relatively high irradiation dose of $\sim 8 \times 10^{16}$ p cm^{-2}. The proton dose for achieving optimal pinning enhancement is around 15×10^{16} p cm^{-2}, which requires long irradiation times thus prohibiting an application of this technique on the industrial scale. However, the irradiation with heavier ions such as oxygen, nickel or gold produces significantly more defects per incident particle than in the case of protons, enabling post-synthesis irradiation times that are suitable for production scale. Figure 22(a) shows on log–log scales the field dependence of J_c before and after irradiation with 3.5 MeV O^{3+} ions to a dose of 0.3×10^{13} O cm^{-2}. The samples were irradiated through the silver layer and there was no copper stabilizer, see figure 14. SRIM simulations (Ziegler and Biersack 1985) reveal that at this energy the highest defect production occurs near the middle of the REBCO layer.

The salient feature of irradiation with O-ions is the pronounced enhancement of the critical current J_c at high magnetic fields. In a field of ~6 T, the enhancement of J_c approaches a factor of two (see figures 22(a) and (c)). As shown in figure 22(a) the field dependence above ~1 T can be well described by a power-law of the form $J_c \sim B^{-\alpha}$. The exponent α strongly decreases with irradiation dose (see figure 22(b)) accounting for the stronger enhancement of J_c at high applied magnetic fields. This result directly addresses a persisting challenge in coated conductor development, namely that their critical current density decreases significantly even in modest applied magnetic fields. The evolution of $J_c(B)$ and α with O-ion irradiation dose shown in figures 22(a) and (b) is also representative of results obtained for a variety of MeV-particle irradiations (Strickland *et al* 2009, Jia *et al* 2013, Haberkorn *et al* 2015b, Rupich *et al* 2015). The optimal irradiation dose depends on field and temperature (figure 22(c)): with decreasing temperature and increasing magnetic field, the peak enhancement requires a higher

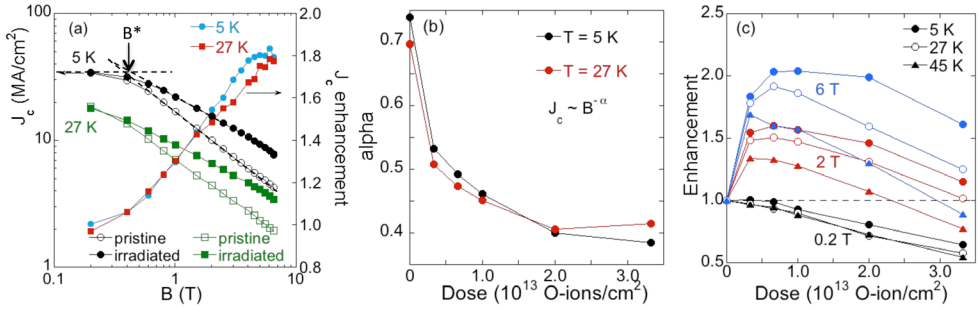

Figure 22. (a) Field dependence of J_c and its enhancement following irradiation with 3.5 MeV oxygen ions to a dose of 0.3×10^{13} O cm^{-2}. The vertical arrow marks the cross-over field B^*. (b) Dose dependence of the power α in $J_c \sim B^{-\alpha}$ describing the in-field suppression of J_c. Upon irradiation, α is strongly reduced resulting in significant enhancement of J_c in high fields. (c) Enhancement factor of J_c at various fields and temperatures as function of irradiation dose (adapted with permission from Leroux *et al* (2015). Copyright 2015, AIP Publishing LLC.).

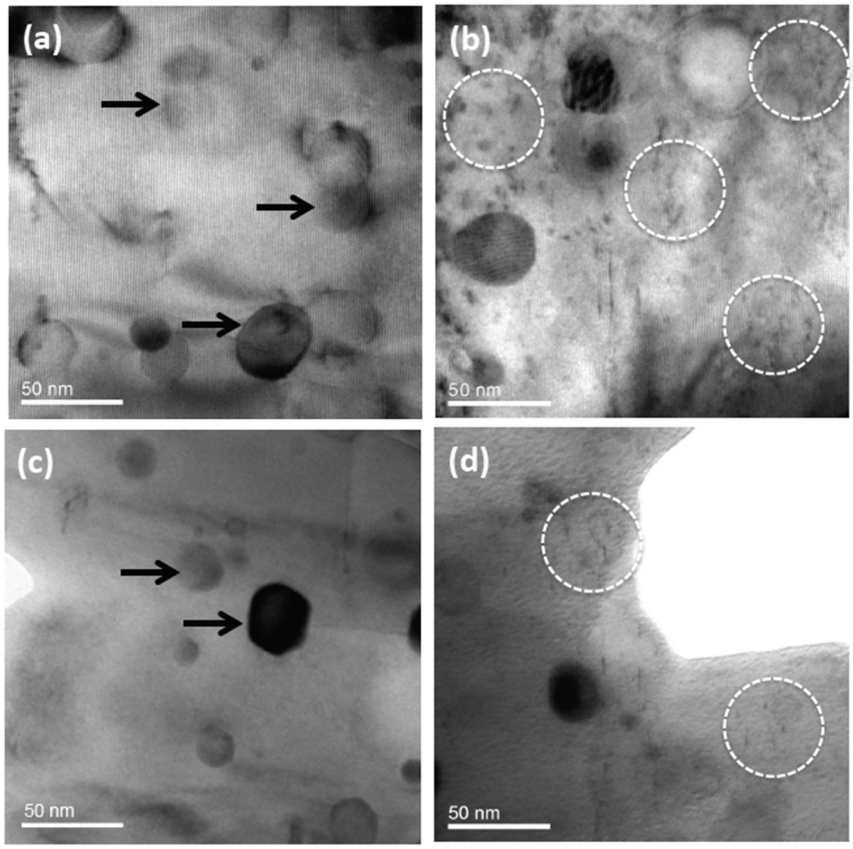

Figure 23. Diffraction contrast TEM images using scattering vectors of (002) in panels (a) and (b) and (200) in panels (c) and (d). Shown is the microstructure of the pristine coated conductor (a) and (c), and of the oxygen-ion irradiated sample (b) and (d). The pristine sample is characterized by Rare Earth Oxide precipitates as marked by black arrows. Upon irradiation a large number of finely dispersed defects of ~5 nm size appear as highlighted by the white circles in (b) and (d) (adapted with permission from Leroux *et al* (2015). Copyright 2015, AIP Publishing LLC.).

irradiation dose, similar to results on proton irradiated samples and in agreement with recent simulations of vortex pinning in random arrays of spherical nanoparticles (Koshelev *et al* 2016) (see also figure 33(a)). Also included in figure 22(a) is the field B^* which marks the cross-over from an almost field independent $J_c(B)$ to the power-law decay. At low temperature, B^* increases slightly from 0.3 T to 0.4 T. However, the effect of MeV-ion irradiation on B^* is generally rather weak as compared to the substantial enhancements seen upon introduction of correlated defects via heavy ion-irradiation (compare figures 20(a) and 25). We note that the irradiation of a ~0.8 cm^2 sample to near optimal dose could be achieved in about 1 s. Furthermore, recently, the doubling of J_c of long-lengths (80 m long and 46 mm wide) production tape has been demonstrated using Au-ion irradiation in a reel-to-reel set-up at a speed of ~0.3 cm s^{-1} (Rupich *et al* 2015). Thus, the irradiation with MeV-ions can be a viable industrial process to tune the pinning microstructure in a post film-synthesis process that results in doubling of the in-field critical current density at high fields.

TEM images on a typical RABiTS commercial coated conductor show that pristine coated-conductor samples contain

mostly rare-earth oxide nanoparticles, several tens of nanometer in diameter and a few stacking faults (see figures 23(a) and (c)). Twin boundaries and dislocations are not visible in the field of view under the chosen imaging conditions for this particular TEM image. Similar to proton irradiation, oxygen irradiation creates a large number of finely dispersed anisotropic small defects approximately 5 nm in diameter, as shown in figures 23(b) and (d). As in the case of irradiated YBCO crystals (Kirk 1993, Kirk and Yan 1999), they are most likely collision cascades and/or defect clusters. In addition, point defects (interstitials and vacancies) are created that are not visible in TEM. The images in figure 23 are suggestive of a mixed-pinning landscape composed of a large number of relatively small irradiation-induced defects coexisting with large pre-existing rare-earth oxide precipitates, twin boundaries, and point defects as sketched in figure 12(b).

At low fields, all vortices are considered strongly pinned by the large oxide particles. In this single-vortex regime J_c is approximately field-independent and the irradiation-induced defects do not contribute to additional vortex pinning. With increasing field, J_c is expected to initially vary approximately as $B^{-1/2}$ and then as B^{-1} when all pin sites are occupied (see equations (27) and (28)). The presented data roughly follow this trend although α of the pristine sample does not reach the value of $\alpha = 1$ at high fields, but instead acquires values of $\alpha \sim 0.7$. Similar α-values have been reported for a broad range of coated conductors (Miura *et al* 2011). With increasing field the finely dispersed irradiation induced defects effectively pin vortex sections between strong pin sites accounting for the observed enhancement of J_c in high fields, as illustrated in figure 12(b). Furthermore, the pinning of interstitial vortices becomes more efficient when more small defects are introduced, thus α should decrease with increasing irradiation dose, as is seen in figure 22(b). Recent numerical simulations of vortex dynamics in pinning structures such as shown in figure 12(b) reveal that the addition of small random pin sites does indeed reduce the value of α (Sadovskyy *et al* 2016b) (see figure 35).

Initial studies of the effect of irradiation on the angular dependence of J_c reveal complex behavior. Measurements in a field of 1 T and at 77 K showed that irradiation of metal-organic deposited films with 70 MeV Ag-ions yields an enhancement of J_c for $B \| c$ and a reduction for $B \| ab$ (Strickland *et al* 2009). This general trend was also obtained after irradiation with 5 MeV Ni and 25 MeV Au-ions (Leonard *et al* 2013a). Measurements at 64 K and 4 T following neutron-irradiation of chemical vapor deposited films showed a pronounced dip of J_c around the in-plane directions (Chudy *et al* 2015). The angular dependence of J_c depends sensitively on temperature, field, defect structure, and balance between isotropic and anisotropic pinning (Civale *et al* 2004, MacManus-Driscoll *et al* 2004, Goyal *et al* 2005, Matsumoto *et al* 2005, Yamada *et al* 2005, Puig *et al* 2008, Maiorov *et al* 2009, Palau *et al* 2011, Selvamanickam *et al* 2012, Choi *et al* 2013, Miura *et al* 2013, Abraimov *et al* 2015, Mishev *et al* 2015). Thus, further investigations on carefully characterized sample are required in order to fully understand the evolution with irradiation.

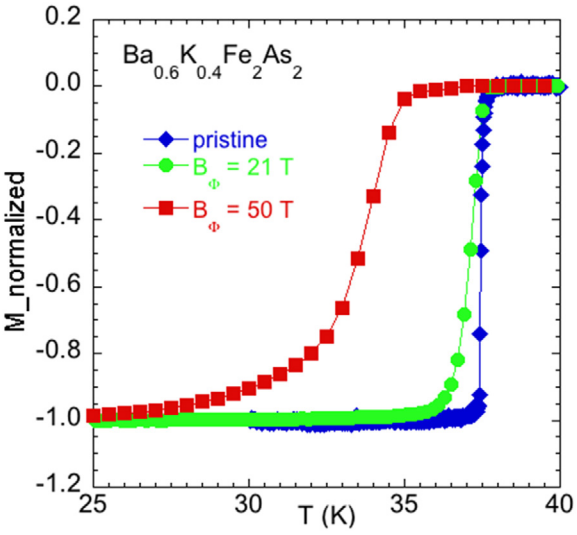

Figure 24. Variation of T_c of a $Ba_{0.6}K_{0.4}Fe_2As_2$ crystal due to irradiation with 1.4 GeV Pb-ions to doses corresponding to dose matching fields of 21 T and 50 T.

3.4. Iron-based superconductors

Iron-based superconductors are comparatively tolerant to a high degree of disorder introduced by particle irradiation while incurring only a modest reduction in T_c. This tolerance enables exploring the interaction of various pin sites in mixed-pinning landscapes over a large range of defect concentration, and to design pinning microstructures that yield very high, almost field-independent critical current densities that come close to those reported for REBCO coated conductors.

Figure 24 shows the superconducting transitions of a series of optimally doped $Ba_{0.6}K_{0.4}Fe_2As_2$ crystals after various stages of irradiation with 1.4 GeV Pb-ions along the crystal c-axis (Fang *et al* 2012) measured in a field of 10 G $\|$ c after zero-field cooling. The crystals had the shape of thin plates such that the Pb-ions penetrate through the entire sample. The irradiation dose is quantified in terms of dose-matching fields of $B_\phi = 4, 6, 10, 21$ and 50 T. The transition temperature and transition width do not change for doses up to 21 T. At $B_\phi = 50$ T, T_c is suppressed by $\sim$2 K and the transition broadens significantly. In comparison, the suppression of T_c in $YBa_2Cu_3O_{7-\delta}$ due to similar Pb-ion irradiation is considerably larger (Goeckner *et al* 2003).

Z-contrast images obtained in STEM (scanning transmission electron microscopy) reveal that the irradiation produces segmented amorphous tracks with an average diameter of 3.7 nm (Fang *et al* 2012). Segmented tracks were also observed in $Ba(Fe_{0.93}Co_{0.07})_2As_2$ following irradiation with 200 MeV Au-ions (Tamegai *et al* 2012). This track size is considerably smaller than 6–8 nm typically observed in heavy-ion irradiated cuprate high-T_c superconductors (Zhu *et al* 1993, Toulemonde *et al* 1994, Yan and Kirk 1998) (see also figure 19), and consistent with the observation that tracks with radius of less than $\sim$1.8 nm tend to be discontinuous (Toulemonde *et al* 1994).

The heavy-ion irradiated $Ba_{0.6}K_{0.4}Fe_2As_2$ displays a remarkable retention of high J_c values in high magnetic fields

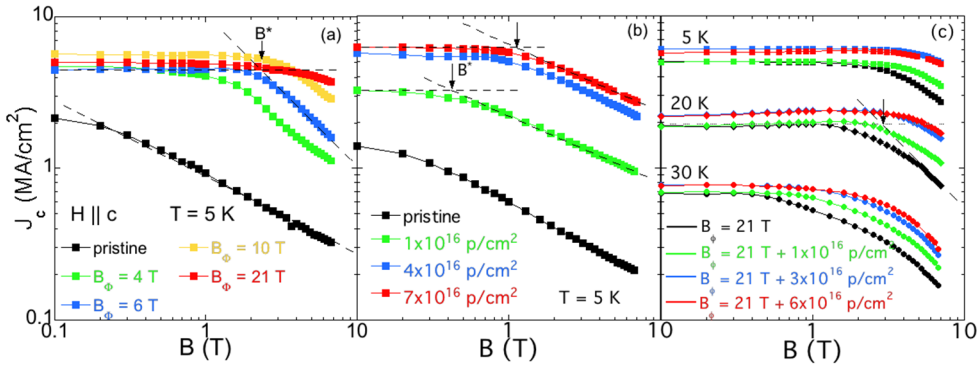

Figure 25. (a) Field dependence of J_c at 5 K of a $Ba_{0.6}K_{0.4}Fe_2As_2$ crystal at various stages of irradiation with 1.4 GeV Pb-ions. An extended field range of almost field independent J_c arises upon irradiation, labeled by B^*. (b) Enhancement of J_c of a $Ba_{0.6}K_{0.4}Fe_2As_2$ crystal due to irradiation with 4 MeV protons. (c) Behavior of J_c in a mixed-pinning landscape composed of irradiation tracks such as in panel (a) and random pins such as in panel (b). By adding various doses of p-irradiation induced random pins to irradiation tracks corresponding to a dose matching field of 21 T, the range of field-independent J_c can be significantly extended. A comparison with panels (a) and (b) directly shows that pinning actions are not simply additive. (Adapted with permission from Fang *et al* (2012) and Kihlstrom *et al* (2013). Copyright 2012 and 2013, respectively, AIP Publishing LLC.)

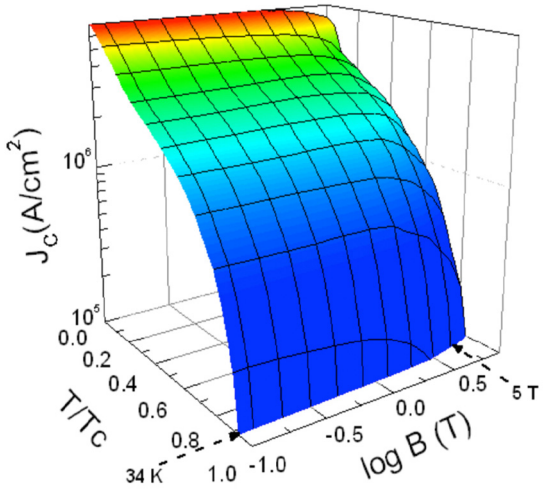

Figure 26. Contour plot of $J_c(B, T)$ of the sample after heavy ion irradiation to a dose matching field of 21 T. One notes that at 5 K and high-field J_c of the irradiated $Ba_{0.6}K_{0.4}Fe_2As_2$ crystal is similar to that of REBCO coated conductors.

and at high temperatures as summarized in figures 25(a) and 26. Figure 25(a) shows the critical current density J_c in magnetic fields along the *c*-axis at 5 K and several irradiation doses. The extraordinary feature is the field independence of J_c at high levels of ∼5 MA cm^{-2} up to fields that exceed 5 T for the $B_\phi = 21$ T-irradiated sample. Consequently, these J_c values in high fields are comparable to those reported for REBCO coated conductors (compare figure 22). They are also significantly higher than those of present iron-selenide (Si *et al* 2013) and iron-arsenide (Katase *et al* 2011) coated conductors indicating that there remains a large headroom in improving the performance of these coated conductors.

At 5 K, the pristine sample has a low-field $J_c \sim 2$ MA cm^{-2} which in fields larger than 0.3 T decreases as $B^{-0.5}$, indicative of pinning by sparse strong pinning sites, see equation (27). The low-field J_c undergoes a modest increase by a factor of 2–3 due to irradiation and shows no systematic dependence on the irradiation dose whereas in high fields the enhancement of J_c exceeds an order of magnitude. The dose-independence of J_c at low fields may be expected when all vortices are strongly pinned and a further increase in pinning sites will not increase J_c. This scenario is analogous to the dose-independence of the low-field J_c of REBCO coated conductors (figure 22(a)). An essentially field-independent J_c is the quintessential signature of this single-vortex strong-pinning regime (see section 2.5.2). At the same time, the field range of constant J_c increases strongly with irradiation dose, demonstrating that this phenomenon is not a self-field effect (Däumling and Larbalestier 1989, Conner and Malozemoff 1991, Hengstberger *et al* 2010), but represents enhanced field-independent strong pinning induced by heavy-ion irradiation. In high fields when vortices appear between the irradiation tracks, J_c decreases as $1/B$, probably due to plastic depinning.

Irradiated $Ba_{0.6}K_{0.4}Fe_2As_2$ also retains high J_c on increasing temperature, figure 26. J_c of the pristine sample is rapidly reduced by a factor of ∼ 40 on increasing the temperature from 4.2 K to 30 K ($T/T_c = 0.81$). In contrast, the reduction is more gradual and amounts to only a factor of ∼7 for the sample irradiated to a dose of $B_\phi = 21$ T maintaining a value of $J_c = 0.32$ MA cm^{-2} in 5 T at 30 K. These observations are in line with theoretical expectations that vortex pinning by strong correlated defects such as heavy-ion tracks is thermally more robust than pinning by point disorder (Nelson and Vinokur 1993).

Figure 25(b) shows the effect of 4 MeV proton irradiation on the critical current density of a $Ba_{0.6}K_{0.4}Fe_2As_2$ crystal. With increasing dose, J_c increases significantly in a uniform fashion. In particular, the low-field J_c increases about 5-fold with a dose of 7×10^{16} p cm^{-2} and the range of field-independent J_c increases from ∼ 0.2 T to 1 T. At the same time, the functional form of the field-dependence of J_c in high fields does not change, $J_c \sim 1/B^{1/2}$, indicating that in the pristine and irradiated samples the same pinning mechanism is active, namely pinning by isolated strong pins. Currently, there are no TEM investigations of *p*-irradiated iron-based superconductors. However, it is likely that a mix of point defects, collision cascades and clusters is generated, in analogy to the behavior seen in YBCO crystals.

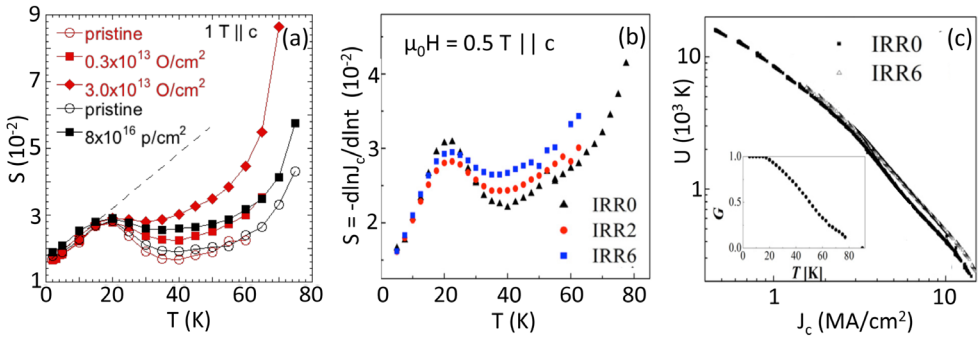

Figure 27. (a) Normalized flux creep rate of a REBCO coated conductors in the pristine state and after various stages of irradiation with protons (black) and oxygen ions (red) (after Leroux *et al* (2015)), (b) Normalized flux creep rate of a coated conductor in the pristine state and after proton irradiation to 2×10^{16} p cm^{-2} and 6×10^{16} p cm^{-2}, respectively. (c) Current dependence of the pinning barrier of the pristine (black) and of the 6×10^{16} p cm^{-2} sample (grey) obtained using the Maley analysis. The inset shows the function $G(T)$ used in the Maley analysis (see equation (33)). (Reprinted with permission from Haberkorn *et al* (2015b). Copyright 2015, IOP Publishing Ltd.)

Thus, defects similar to those shown in figure 23 may serve as irradiation-induced strong pin-sites. Since the field range of field-independent J_c varies in proportion with the low-field J_c, self-field effects are likely to play a role (Däumling and Larbalestier 1989, Conner and Malozemoff 1991, Hengstberger *et al* 2010). Nevertheless, the low-field J_c increases approximately as the square root of the irradiation dose, consistent with the prediction for strong pinning, equation (24).

Samples such as those shown in figures 25(a) and (b) form an ideal basis for creating mixed-pinning landscapes composed of random strong pins and correlated 1D pins in a controlled fashion (combination of figures 5(b) and (d)). For example, figure 25(c) shows the effect of adding *p*-irradiation induced defects to irradiation tracks caused by 21 T heavy ion irradiation. In contrast to figure 25(b), *p*-irradiation of the sample containing irradiation tracks does not increase the low-field J_c, presumably because strong pinning by the irradiation tracks already immobilizes all vortices. However, *p*-irradiation clearly extends the field-range of field-independent J_c. Since the low-field J_c does not change, this enhanced range is not a self-field effect, but instead the signature of a mixed-pinning landscape in which the random defects pin vortices that are not trapped on irradiation-induced tracks in high fields, as schematically shown in figure 12(a). These data also show that the pinning action of multiple pin sites is in general not simply additive.

3.5. Vortex creep in high-performance superconductors

Thermal fluctuations and the ensuing relaxation (creep) in non-equilibrium vortex configurations are defining characteristics of high-temperature superconductors. Creep phenomena have strong influence on high-performance superconductors as they limit the critical current density that can actually be achieved at a given magnetic field and temperature. Experimentally, flux creep manifests itself in the decay with time of the hysteretic magnetization as quantified by the logarithmic relaxation rate $S = \mathrm{d}\ln M/\mathrm{d}\ln t$ and in the form of the current–voltage (I–V) curves. Both quantities yield information on the dependence of the vortex pinning potential U on current, temperature and magnetic field (see section 2.6). The I–V curves of high-temperature superconductors can frequently be described by a power law $V = V_c(I/I_c)^n$ (Brandt 1996, Yamasaki and Mawatari 1999, Thompson *et al* 2008, Polat *et al* 2011, Chudy *et al* 2015) (compare figure 21). This form of the I–V curve corresponds to a current dependent pinning potential of the form $U = U_0 \ln(J_c/J)$ with $n = U_0/k_BT \gg 1$ and $S \approx 1/n$. Measurements over a wide range in voltage reveal deviations from the power-law I–V characteristics, which are caused by the collective nature of vortex pinning and the glassiness of the vortex matter (Yeshurun *et al* 1996) (see section 2.6).

Figure 27(a) shows the temperature dependence of the relaxation rate S for oxygen and proton irradiated samples of REBCO coated conductors in a field of 1 T ∥ c. It is remarkable that the creep rate for all samples approaches a common, almost linear, temperature dependence at temperatures below 20 K. A similar finding has been reported for coated conductors grown using different synthesis routes including pulsed-laser deposition and metal-organic deposition (Haberkorn *et al* 2012b), solution grown YBCO films containing BZO and Ba_2YTaO_6 nanoparticles (Rouco *et al* 2014), as well as for *p*-irradiated $GdBa_2Cu_3O_7$ films (see figure 27(b)) (Haberkorn *et al* 2015b). A linear $S(T)$-relation of the form $S = k_BT/U_0$ is reminiscent of the classic Anderson–Kim model of vortex creep. From the data in figure 27, one estimates $U_0 \sim 1200$ K for all samples, independent of the irradiation state. This suggests that vortex dynamics is dominated by strong pre-existing pinning, i.e. rare earth nanoparticles such as seen in figures 23(a) and (c), twin boundaries or BZO nanorods. For comparison, for the $T_c = 40$ K superconductor, MgB_2, in a field of 1 T, $U_0 \sim 4000$ K and the creep rate is approximately one order of magnitude lower, consistent with much smaller fluctuation effects in this material. $S(T)$ in figures 27(a) and (b) does not extrapolate to zero, indicative of a contribution due to quantum creep at very low temperatures.

Above 20 K, all samples show a clear departure from the almost linear $S(T)$ dependence, pointing to a fundamental change in the vortex dynamics. $S(T)$ of the pristine sample is non-monotonic with a minimum around 40 K almost reaching the zero-temperature value, and the creep rate strongly

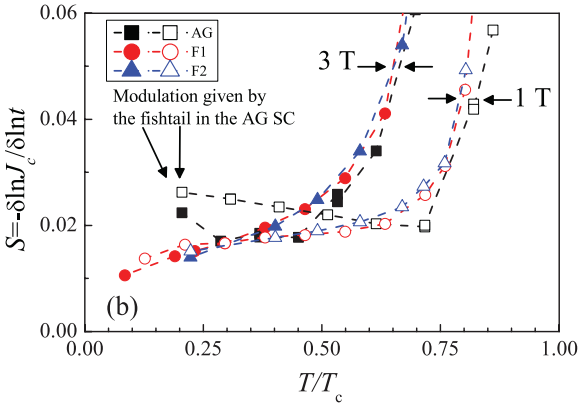

Figure 28. Normalized flux creep rate of $Ba(Fe_{0.925}Co_{0.075})_2As_2$ crystals in the pristine state (labeled as AG), after irradiation with 3 MeV protons to a dose of 1×10^{16} p cm^{-2} (F1) and 2×10^{16} p cm^{-2} (F2) in fields of 1 T ‖ c (open symbols) and 3 T ‖ c (closed symbols). The analysis is complicated by the fishtail effect (non-monotonic field dependence) in J_c observed for the pristine sample. (Reprinted figure with permission from Haberkorn *et al* (2012a) (figure 4). Copyright (2012) by the American Physical Society.)

increases with irradiation dose. A minimum in $S(T)$ has also been observed in other YBCO films with pinning dominated by large nanoparticles and is likely due to the large pinning energy of these defects (Haberkorn *et al* 2012b).

In the field range of 0.5 T to 1 T, particle irradiation does not strongly affect J_c. Depending on temperature and irradiation dose, a small increase or decrease in J_c have been observed (Jia *et al* 2013, Haberkorn *et al* 2015b, Leroux *et al* 2015, Eley *et al* 2016). However, the creep rate at temperatures above 20 K strongly and systematically increases with both oxygen and proton irradiation dose (figures 27(a) and (b)), consistent with a scenario in which pinning and creep become progressively dominated by smaller, irradiation induced defects. In contrast, the creep rate of YBCO single crystals in 1 T ‖ c decreases over the entire temperature range following irradiation with 3 MeV protons to a dose of 1×10^{16} p cm^{-2}, while at lower doses the effects on S are weak (Civale *et al* 1990, Thompson *et al* 1993). This behavior supports the notion that it is competing effects arising in a mixed-pinning landscape such as sketched in figure 12(b) that are responsible for the increase in S in particle irradiated coated conductors. Figure 27(c) shows the current dependence of the pinning barrier obtained from the data in figure 27(b) using the Maley-analysis (Maley *et al* 1990, Polat *et al* 2011) (see also equations (32) and (33)). The $U(J)$-dependence of the pristine sample displays a steep variation at intermediate currents, that is, at intermediate temperatures, which, according to equation (30) corresponds to a low value of S. Upon irradiation, the section of low pinning potentials at high currents, low temperatures, is slightly raised thereby removing the steep $U(J)$ dependence. As a result, the creep rates increase. Physically, the presence of a large number of irradiation-induced defects between the rare-earth oxide particles promotes wandering of vortices away from the particles, see section 2.8. The evolution of the creep rate with irradiation (figure 27(a)) is consistent with the IV-curves shown in figure 21. Namely, upon irradiation the n-value slightly decreases from 28 to 25 and according to the relation $S \approx 1/n$ would correspond to an increase in S.

Vortex creep and the effect of particle irradiation have been investigated for various Fe-based superconductors such as Co-doped $BaFe_2As_2$ irradiated with protons (Haberkorn *et al* 2012a, Taen *et al* 2012) and heavy ions (Tamegai *et al* 2012), proton-irradiated $Na_{1-x}Ca_xFe_2As_2$ (Haberkorn *et al* 2014), $Ba_{0.6}K_{0.4}Fe_2As_2$ (Taen *et al* 2015) and FeSe (Sun *et al* 2015a, 2015b). Generally, the creep rates observed in single-crystal samples are high, comparable to those seen in YBCO-samples, $S \sim 0.02$, which is indicative of low pinning barriers. Particle irradiation causes substantial increases of J_c in all reports (see also figure 25), but the effect on the creep rate varies from material to material. For instance, proton irradiation of $Ba(Fe_{0.925}Co_{0.075})_2As_2$ has only a weak effect on S (see figure 28). In contrast, the irradiation with heavy ions such as 200 MeV Au-ions, 800 MeV Xe-ions or 2.6 GeV U-ions induces a clear decrease of S (Tamegai *et al* 2012). A reduction in S has also been reported for p-irradiated $Na_{1-x}Ca_xFe_2As_2$ (Haberkorn *et al* 2014) and $Ba_{0.6}K_{0.4}Fe_2As_2$ (Taen *et al* 2015). In the latter case, the pristine crystal is characterized by a non-monotonic $S(T)$-dependence, analogous to figures 27(a) and (b), with a maximum of ~ 0.04 near 5 K and a minimum of ~ 0.025 near 15 K. Upon p-irradiation, $S(T)$ acquires a slowly rising linear dependence with a value of 0.01 at 5 K.

To summarize this section, the field dependence at 4.2 K of the critical current density J_c of industrial-scale and research-scale REBCO coated conductors (CCs), of iron-based superconductors, and of industrial NbTi and Nb_3Sn superconductors is illustrated in figure 29 with the help of several examples; data on conductors from other sources can be found in recent overviews, e.g. Selvamanickam *et al* (2015b). Particularly in REBCO coated conductors very high values of J_c have been realized attesting to the successful implementation of effective mixed-pinning landscapes either through chemical synthesis means (UH, Bruker HTS) or via post-synthesis particle irradiation (AMSC). For long-length industrial-scale samples, the low-field J_c now approaches $\sim 15\%$ of the depairing current density, $J_{dp} \sim 300$ MA cm^{-2} for YBCO. The corresponding numbers for Nb_3Sn and NbTi wires are $< 1\%$ and 5–10%, respectively (Larbalestier *et al* 2001). The J_c-values of iron-based superconductors are generally significantly lower than those of REBCO coated conductors. However, the introduction of a mixed-pinning landscape into $Ba_{0.6}K_{0.4}Fe_2As_2$ crystals via combined heavy-ion and proton irradiation demonstrates that this material can carry enormous currents, especially in high fields where it reaches the performance of REBCO coated conductors. J_c-values for NbTi and Nb_3Sn are comparatively low. In figure 29 the critical current density J_c is presented since this quantity is directly related to the vortex pinning mechanisms, the subject of this review. However, for applications the important quantity is the *engineering* current density, J_e, which is the total current *per wire cross-section* at a given temperature and magnetic field. Owing to the complex layered structure of the coated conductor geometry (see figure 14) the superconductor fraction is low and J_e of present REBCO coated conductors amounts to only 1–5% of J_c.

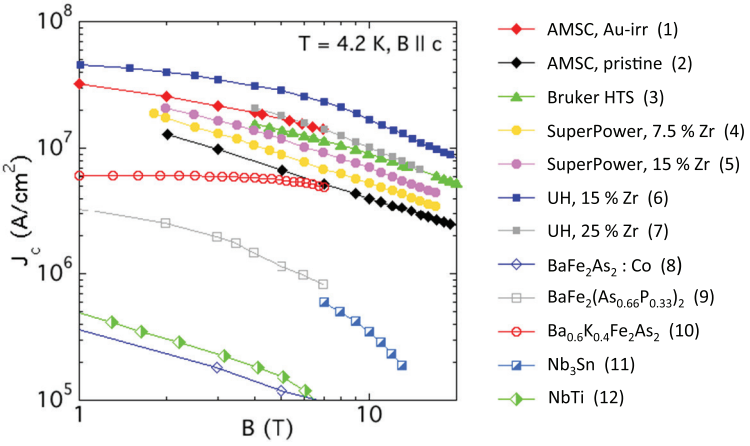

Figure 29. Field dependence of J_c (critical current per superconductor cross section) for various industrial-scale and research-scale REBCO coated conductors (filled symbols), iron-based superconductors (open symbols) and conventional superconductors (half-filled symbols). (1) REBCO CC from American Superconductor Corp irradiated with 16 MeV Au-ions to a dose of 6×10^{11} Au cm^{-2}, 1.2 μm thickness (Rupich *et al* 2015), (2) pristine AMSC CC, 1.2 μm (Rupich *et al* 2015); (3) REBCO CC from Bruker HTS, 2 μm (Abraimov *et al* 2015); (4), REBCO CCs from SuperPower Corp with 7.5% Zr and 1.7 μm (Hazelton *et al* 2015); (5) REBCO CCs from SuperPower Corp with 15% Zr, 2 μm (Hazelton *et al* 2015); (6) REBCO CC from the University of Houston containing 15% Zr-doping, 1 μm (Xu *et al* 2014); (7) REBCO CC from the University of Houston containing 25% Zr-doping, 3.3 μm (Selvamanickam *et al* 2015b); (8) $BaFe_2As_2$: Co CC, 0.15 μm (Katase *et al* 2011); (9) $BaFe_2(As_{0.66}P_{0.33})_2$ thin film doped with 3% BZO, 0.1 μm (Miura *et al* 2013); (10) $Ba_{0.6}K_{0.4}Fe_2As_2$ crystal irradiated to 21 T + 3×10^{16} p cm^{-2} as shown in figure 25(c), magnetization at 5 K; (11) Nb_3Sn ITER type, Mitsubishi internal tin process (Lee and Larbalestier 2008); (12) NbTi, data from High-field National Laboratory webpage (2015).

In contrast, this ratio is much higher for Nb_3Sn and NbTi. This ratio is also high for round wires made of $Bi_2Sr_2CaCu_2O_{8-x}$ (Bi2212). This material has a low J_c due to poor grain alignment, but a high J_e, which makes it interesting particularly for high magnetic field applications (Larbalestier *et al* 2014). Application targets are usually expressed in terms of J_e. For example, power transmission targets require $J_e \sim 500$ A cm^{-1}-width at 77 K and self-field, whereas for generators and motors the target values are 1500 A cm^{-1}-width at 25–50 K in 1.5–3 T‖c and for high-energy particle accelerators, $J_e \sim 600$ A mm^{-2} at 4.2 K and 20 T are desired (Rupich and Zhang 2015). High J_e can be achieved by increasing the superconductor fill-factor and/or by enhancing J_c, and these targets are now coming into range with optimized mixed-pinning structures in long-length conductors. The identification of what microstructures constitute optimized pinning landscapes for high-field or high-temperature applications is an important issue in future work, in which large-scale numerical simulations described in the next section will play a central role.

4. Vortex pinning simulations

Predicting the behavior of large-scale arrays of vortices in different pinning landscapes and evaluating critical currents are fundamental challenges of high practical value. As discussed in section 2, analytical approaches can give qualitative predictions of critical currents only for simple model systems. Large-scale numerical simulations are required to develop a quantitative description of vortex behavior in realistic mixed-pinning landscapes.

The value of numerical modeling in exploring and understanding vortex matter was recognized long ago (Brandt 1983a, 1983b). Several approaches have been used to model vortex states in superconductors, the choice being determined by a trade-off between complexity and fidelity. All vortex-matter simulations can be loosely divided into two groups: (i) on the equilibrium phase diagram and (ii) on dynamics and pinning. In this review we mostly focus on the second group. There is overlap between these two groups for disordered systems because vortex dynamics actually provides the most revealing probe of the phase diagram.

In the following sections, we review studies of the behavior of vortex lines using the Langevin-dynamics approach, followed by a review of more realistic and powerful vortex-matter simulations based on the time-dependent Ginzburg–Landau formulation. We conclude this section on the current state of vortex-matter simulations by highlighting the emerging concept of 'critical current by design', which will allow the prediction of optimal pinning configurations in high-performance superconductors.

4.1. Langevin-dynamics simulations

As displacements of the vortices are the softest perturbations in the mixed state, a natural minimal approach is to keep only the vortex degrees of freedom and neglect all other perturbations of the superconducting order parameter. This approximation provides a reasonable description of the vortex state at low fields, when the distance between vortices is much larger than the coherence length, and for a low density of pinning centers when they occupy a small volume fraction of the material.

A relatively simple situation is realized in thin superconducting films when the distance between vortices exceeds the film thickness. In this case bending of the vortex lines can be neglected and they can be treated as interacting pointlike

objects moving in random potential created by pinning centers (two-dimensional (2D) case). The dynamics of such objects can be described by an overdamped equation of motion taking into account thermal Langevin forces. We present here a short overview of these 2D simulations as this is not the main focus of the review. The two-dimensional simulations of vortex matter were initiated by Brandt (Brandt 1983a, 1983b) and later extended by many authors revealing the rich dynamic behavior of this system (Jensen *et al* 1988, Koshelev 1992, Koshelev and Vinokur 1994, Grønbech-Jensen *et al* 1996, Moon *et al* 1996, Olson *et al* 1998, Cao *et al* 2000, Fangohr *et al* 2001, Fruchter 2002, Fily *et al* 2010, Scala *et al* 2012). The studied issues include scaling of critical current with strength and density of pins (Brandt 1983a, 1983b), crossover between elastic and plastic regimes (Koshelev 1992, Cao *et al* 2000, Scala *et al* 2012), thermal depinning (Koshelev 1992), ordering of vortex lattice at large velocities (Koshelev and Vinokur 1994, Moon *et al* 1996), and the critical behavior near the onset of motion slightly above the threshold (Fily *et al* 2010). The universal feature observed in many simulation studies is the formation of one-dimensional channels where vortices flow plastically (Jensen *et al* 1988, Koshelev 1992, Grønbech-Jensen *et al* 1996, Fruchter 2002, Fily *et al* 2010).

In this review we mostly focus on the case of pinning in bulk materials relevant for applications. In the three-dimensional case, the description of vortex matter is complicated by the bending of the vortex lines and they have to be treated as elastic strings (Ertaş and Kardar 1996, van Otterlo *et al* 2000, Bustingorry *et al* 2007, Luo and Hu 2007, 2010, Koshelev and Kolton 2011, Dobramysl *et al* 2013). An additional complication is that both the single-vortex elasticity and intervortex interactions are nonlocal for the coordinate along the magnetic field. This complication is usually ignored and both energy contributions are replaced by approximate local forms with the assumption that this does not qualitatively change the properties of the system.

The dynamics of a single vortex line in a random potential has been investigated in Ertaş and Kardar (1996) and Koshelev and Kolton (2011). This single-vortex regime corresponds to a superconductor in very small magnetic fields. The configuration of an isolated line is defined by the two-dimensional vector **u** depending on the coordinate along the magnetic field z and time t. The equation describing vortex-line dynamics in a random potential has the following form

$$\eta\frac{\partial \mathbf{u}}{\partial t} = \varepsilon_1\frac{\partial^2 \mathbf{u}}{\partial z^2} + \sum_j \mathbf{F}_{\rm vp}(\mathbf{u}-\mathbf{R}_j)\delta(z-z_j) + \mathbf{f} + \mathbf{F}_T(z,t). \quad (37)$$

Here η is the viscosity coefficient, ε_1 is the line tension, **f** is the driving force from the current, $(\mathbf{R}_j, Z_j)$ are the random pin coordinates, $\mathbf{F}_{\rm vp}(\mathbf{u})$ is the vortex-pin interaction force, $\mathbf{F}_T(z,t)$ is the Langevin thermal force

$$\left\langle F_{T,\alpha}(z,t)F_{T,\alpha'}(z',t')\right\rangle = 2\eta T\delta_{\alpha\alpha'}\delta(t-t')\delta(z-z').$$

The dynamical critical behavior of a vortex line near the depinning threshold has been studied in Ertaş and Kardar (1996). The long-range wandering of the line was assumed to follow the scaling law

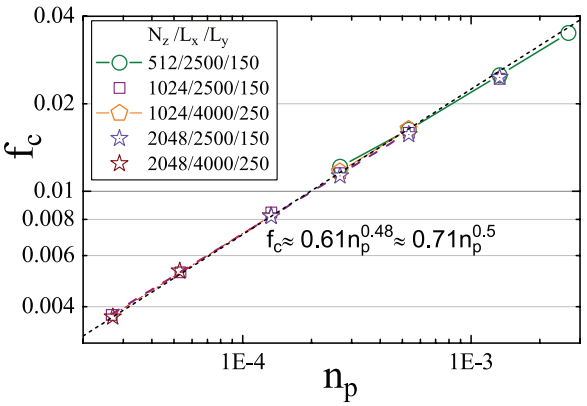

Figure 30. The dependence of the critical force on the pin density for different system sizes, the legend shows the line lengths N_z, sizes in the direction of motion L_x, and in the transversal direction L_y. (Reproduced figure with permission from Koshelev and Kolton (2011). Copyright 2011 by the American Physical Society.)

$$\langle [u_{\rm l,t}(z) - u_{\rm l,t}(0)]^2\rangle \propto z^{\zeta_{\rm l,t}}, \quad (38)$$

where $u_{\rm l}(z)$ and $u_{\rm t}(z)$ are line displacements along the driving force and in the transverse direction, respectively. Typically, $u_{\rm l}(z) \gg u_{\rm t}(z)$ meaning that the line is deformed stronger along the direction of motion, see figure 8. Numerical results showed that $\zeta_{\rm l} \approx 1$ and $\zeta_{\rm t} \approx 0.5$, in agreement with renormalization-group analysis. The value $\zeta_{\rm l} = 1$ is, in fact, the maximum possible power index in the long-range displacements marking the breakdown of linear elasticity. More complete information is contained in the structure factors $S_{\rm l,t}(q) = \langle [u_{\rm l,t}(q)]^2\rangle$, where $u_{\rm l,t}(q)$ are the Fourier transforms of $u_{\rm l,t}(z)$. For $\zeta_{\rm l,t} < 1$, the scaling in equation (38) corresponds to $S_{\rm l,t}(q) \propto q^{1+2\zeta_{\rm l,t}}$. The analysis of the structure factor allows treatment of the case $\zeta_l > 1$, as described below.

The strong pinning of individual vortex lines by randomly arranged nanoparticles has been explored in Koshelev and Kolton (2011). It was found that the critical current grows roughly as the square root of the pin density, as suggested by qualitative estimates, equation (24), see figure 30. The system sizes $L_{x,\,y}$ are measured in units of pin range $r_{\rm p}$. The units of pinning force f_c and pin density $n_{\rm p}$ are set by $\varepsilon_{\rm l}$, $r_{\rm p}$, and the pinning energy of an isolated pin $U_{\rm p}$ as $f_{c0} = U_{\rm p}^2/\varepsilon_{\rm l} r_{\rm p}^3$ and $n_{p0} = U_{\rm p}/\varepsilon_{\rm l} r_{\rm p}^4$. The strong pinning scenario corresponds to $n_{\rm p} \ll n_{p0}$, see figure 7. The configurations of pinned vortex lines in the critical region is strongly anisotropic; that is, displacements in the driving direction are much larger than in the transverse direction, see figure 8. The analysis of the structure factors $S_{\rm l,t}(q)$ gave indices $\zeta_{\rm l} \approx 1.14$ and $\zeta_{\rm t} \approx 0.45$ which somewhat differ from those obtained in Ertaş and Kardar (1996) using long-range displacements. In particular, the value of $\zeta_{\rm l} > 1$ implies that the assumed elastic approximation is not self-consistent in the thermodynamic limit. It was also established that the dominant effect of thermal fluctuations is the suppression of the pin-breaking forces of the individual pins. This leads to a strong reduction of the apparent critical current by thermal noise and a straightening of the vortex lines in the critical region.

The pinning properties of interacting lines have been studied in van Otterlo *et al* (2000), Bustingorry *et al* (2007), Luo and Hu (2007, 2010) and Dobramysl *et al* (2013). The dynamics of driven vortex matter is described by the coupled equations for the line coordinates $\mathbf{u}_s(z,t)$

$$\eta\frac{\partial \mathbf{u}_s}{\partial t} = \varepsilon_1\frac{\partial^2 \mathbf{u}_s}{\partial z^2} + \sum_{s'}\mathbf{F}_{\rm vv}(\mathbf{u}_s-\mathbf{u}_{s'}) + \sum_j \mathbf{F}_{\rm vp}(\mathbf{u}_s-\mathbf{R}_j)\delta(z-Z_j) + \mathbf{f} + \mathbf{F}_{T,s}(z,t). \tag{39}$$

Here, $\mathbf{F}_{\rm vv}(\mathbf{u})$ is the vortex–vortex interaction force which is usually approximated by the expression strictly valid for straight lines, $\mathbf{F}_{\rm vv}(\mathbf{u}) = \varepsilon_0\nabla \mathrm{K}_0(u/\lambda)$, where λ is the London penetration depth.

van Otterlo *et al* (2000) studied the evolution of voltage-current dependences and critical currents for different temperatures and magnetic fields across the Bragg glass to vortex glass transition and across the melting line. The typical simulated system contained 7×7 vortices in 50 layers and they found a peak in the critical current for both cases. The unusual generic feature in the peak region is the crossing of I–V curves at different temperatures.

Luo and Hu (2007), (2010) studied depinning and creep of interacting vortex lines both in the Bragg glass and vortex glass regimes. The transition between the two glass states was induced by changing the strength of the pinning centers. The authors studied the scaling of the velocity-force dependences near the threshold force in the case of strong pinning (Luo and Hu 2007). Two different vortex creep exponents for the two glass regimes were extracted: $\mu = 0.5\pm 0.02$ for the Bragg glass and $\mu = 0.28\pm 0.02$ for the vortex glass (Luo and Hu 2010).

Extensive studies of the relaxation dynamics for interacting vortex lines were reported in Bustingorry *et al* (2007) and Dobramysl *et al* (2013). The observed dynamics reflects the glassy nature of this system.

The Langevin-dynamics description considered in this section has several important limitations: vortex–vortex and vortex-pin interactions can be treated only approximately, and possibilities of vortex cuttings and reconnections are completely neglected. Since the latter events are essential in the liquid phase, such models do not provide an adequate description for this state. Also, this simplified model cannot be used when pinning centers occupy a noticeable fraction of the superconductor's volume corresponding to strongest pinning. Therefore, it is desirable to probe the strong-pinning regime by more sophisticated models.

4.2. Large-scale Ginzburg–Landau simulations: critical current by design

A realistic description of the vortex dynamics in superconductors is the time-dependent Ginzburg–Landau (TDGL) approach, which describes the full behavior of the superconducting order parameter (Schmid 1966). This approach represents the most reasonable compromise between an approximate/phenomenological and an exact/microscopic description of vortex matter and provides a 'mesoscopic bridge' between micro and macro scales. It catches the most essential features of vortex matter and describes all pinning regimes from weak to strong pinning. Not only are all interaction energies for arbitrarily shaped vortices automatically taken into account, but also vortex-core structures and interaction with pinning centers are described realistically.

In a more general context, the TDGL formulation is one of the most successful physical models describing the behavior of many different physical systems (Aranson and Kramer 2002). The Ginzburg–Landau (GL) equations describe spatial variations of the superconducting order parameter ψ in the presence of an electromagnetic vector potential $\mathbf{A}$. Far from $T_{\rm c}$, the GL equations do not correctly reproduce the physics in the vortex core, but still describe the interaction between vortices correctly, see e.g. Aranson and Kramer (2002).

The TDGL equations are the dynamic generalization of the static equations obtained by minimizing the GL functional (1),

$$\Gamma\left(\partial_t + \imath\frac{2e}{\hbar}\mu\right)\psi = a_0\epsilon(\mathbf{r})\psi - b|\psi|^2\psi + \sum_\alpha \frac{1}{4m_\alpha}\left(\hbar\nabla_\alpha + \frac{2e}{\imath c}A_\alpha\right)^2\psi + \zeta(\mathbf{r},t), \tag{40}$$

$$\nabla\times(\nabla\times\mathbf{A}) = \frac{4\pi}{c}\left[\mathbf{J}_{\rm N}+\mathbf{J}_{\rm S}+\mathcal{I}(\mathbf{r},t)\right], \tag{41}$$

where μ is the scalar potential and Γ is a phenomenological dynamic parameter. The Langevin terms $\zeta(\mathbf{r},t)$ and $\mathcal{I}(\mathbf{r},t)$ describing thermal noise, have the correlators

$$\langle\zeta^*(\mathbf{r},t)\zeta(\mathbf{r}',t')\rangle = 2\Gamma T\,\delta(\mathbf{r}-\mathbf{r}')\delta(t-t') \tag{42}$$

$$\langle\mathcal{I}_\alpha(\mathbf{r},t)\,\mathcal{I}_\beta(\mathbf{r}',t')\rangle = 2T\sigma_\alpha\delta_{\alpha\beta}\,\delta(\mathbf{r}-\mathbf{r}')\delta(t-t'), \tag{43}$$

respectively, where σ_α are the normal conductivity components (we assume that $\sigma_x=\sigma_y=\sigma$ and $\sigma_z=\sigma/\gamma^2$).

Equation (41) is the Maxwell equation[10] governing the dynamics of $\mathbf{A}$, where $\mathbf{J}_{\rm N}$ and $\mathbf{J}_{\rm S}$ are the normal and superconducting currents, respectively. These currents are given by

$$J_{{\rm N},\alpha} = -\sigma_\alpha[(1/c)\,\partial_t A_\alpha + \nabla_\alpha\mu], \tag{44}$$

$$J_{{\rm S},\alpha} = -\frac{e}{2m_\alpha}\left[\psi^*\left(\imath\hbar\nabla_\alpha + \frac{2e}{c}A_\alpha\right)\psi + \text{c.c.}\right]. \tag{45}$$

The Landau gauge is typically used for the vector potential: $\nabla\mathbf{A}=0$. Correspondingly, the magnetic induction $\mathbf{B}$ and electric field $\mathbf{E}$ are determined by $\mathbf{B}=\nabla\times\mathbf{A}$ and $\mathbf{E}=-(1/c)\,\partial_t\mathbf{A}-\nabla\mu$.

Modeling of pinning centers of different types with TDGL, equation (40), requires different approaches. $\delta T_{\rm c}$ pinning (see section 2.4.1) can be modeled through small random modulation of the coefficient $\epsilon(\mathbf{r}) = [T_{\rm c}(\mathbf{r})-T]/T$. Extended regions of negative ϵ can be used for modeling of large-scale metallic pinning sites. δl pinning can be realized by (spatial)

[10] Note, that the term $(1/c)\,\partial_t\mathbf{E}$ in equation (41) is neglected because the time variation rates of $\mathbf{A}$ are much slower than the frequencies of the corresponding electromagnetic waves.

modifications of the effective mass components m_α. Modeling of strain fields, and dislocations requires both T_c and m_α modulation. Magnetic bulk defect (see section 2.4.3) can be introduced by choosing local dipolar magnetic fields, which modify the vector potential **A**, see e.g. Doria *et al* (2007). Finally, modeling of geometrical constraints and voids of various shapes is done by imposing appropriate internal boundary conditions within the integration domain or using unstructured grid discretizations. With respect to applications in high-performance superconductors, mostly spatial T_c modulation was studied so far.

Strictly speaking, these dynamic equations are microscopically justified only for gapless superconductors (Gor'kov and Éliashberg 1968). In other cases, the exact dynamic equations can be much more complicated and difficult for numerical implementation, see, e.g. Zhu *et al* (1998), where dynamic equations for superconductors with mixed *d*- and *s*-symmetry have been derived. Nevertheless, the TDGL description can be used to study problems, where the exact dynamics is not crucial. Vortex pinning is such a problem, since it only involves static or slowly moving vortex configurations.

For numerical simulations, equations (40) and (41) can be written in the dimensionless form

$$u(\partial_t+\imath\mu)\psi = \epsilon(\mathbf{r})\psi - |\psi|^2\psi + \sum_\alpha \eta_\alpha(\nabla_\alpha - \imath A_\alpha)^2\psi + \zeta(\mathbf{r},t), \tag{46}$$

$$\kappa^2\nabla\times(\nabla\times\mathbf{A}) = \mathbf{J}_N + \mathbf{J}_S + \mathcal{I}(\mathbf{r},t), \tag{47}$$

where $\eta_x=\eta_y=1, \eta_z=1/\gamma^2, u=\Gamma/a_0t_0$ with the unit of time $t_0=4\pi\sigma\lambda_0^2/c^2$. The zero-temperature coherence length ξ_0 is used for the unit of length. Correspondingly, the total current density $\mathbf{J}=\mathbf{J}_S+\mathbf{J}_N$ (in units of $J_0=\hbar c^2/8\pi e\lambda_0^2\xi_0 = (e\hbar/m\xi_0)\psi_0^2$) assumes the form[11]

$$J_\alpha = \eta_\alpha\{\mathrm{Im}[\psi^*(\nabla_\alpha-\imath A_\alpha)\psi] - (\nabla_\alpha\mu + \partial_t A_\alpha)\}, \tag{48}$$

where the magnetic field is measured in units of the upper critical field $H_{c2}(0)=\Phi_0/2\pi\xi_0^2$ at zero temperature and the electric field $\mathbf{E}=-\nabla\mu-\partial_t\mathbf{A}$ is measured in units of J_0/σ.

In order to study sufficiently large systems numerically, the implementation of the solver for the TDGL typically has to be highly efficient and parallelized. We will not review the different technical approaches to this problem. In most computational schemes used for TDGL, the system is discretized in space on a regular grid and integrated in time by using an explicit or implicit time integration scheme (see e.g. Gropp *et al* (1995), Crabtree *et al* (2000) and Gunter *et al* (2002)). A recent implementation using an underlying regular spatial mesh on modern graphics processing units is described in detail in Sadovskyy *et al* (2015). Irregular voids and internal boundary condition are most naturally discretized by irregular/unstructured discretization schemes, see, e.g. Du (1994), Gao and Sun (2015) and Li and Zhang (2015).

[11] The maximum supercurrent density which can flow without dissipation (depairing current density) is $J_{dp}=(2/3\sqrt{3})(1-T/T_c)^{3/2}\approx 0.385(1-T/T_c)^{3/2}$ in the reduced units.

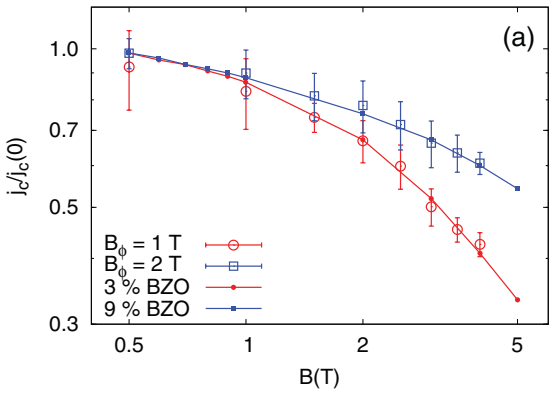

Figure 31. Calculated J_c (empty symbols) compared to experimental data (line points) when the simulation and sample contain nanorods. The simulation point is an average over several different pinscapes and the error bars are the standard deviations of those. (Reprinted figure with permission from Palonen *et al* (2012) (figure 4(a)). Copyright (2012) by the American Physical Society.)

The TDGL approach was used earlier to study different properties of the vortex state. In Gropp *et al* (1995) and Crabtree *et al* (2000) the numerical integration of the TDGL system received substantial attention and the dynamics of vortices was studied in different situations, such as plastic and elastic steady-state motion in the presence of a twin boundary, dynamics in systems with regular and irregular arrays of point defects, and vortices moving through an array of columnar defects. These studies were mostly illustrative and a meaningful exploration of larger systems was impeded by computational limitations. In two-dimensional simulations it has recently been possible to simulate the collective dynamics of up to a hundred vortices: in Palonen *et al* (2012) the authors studied the field dependence of the critical current, $J_c(B)$, in thin films with columnar defects aligned with the field and compared it to the critical current of a thin-film $YBa_2Cu_3O_{6+x}$ sample doped with $BaZrO_3$ nanoparticles and found good agreement, see figure 31. The experimental film was 15 nm thick such that the 2D approximation worked rather well. It is worth noting, that the authors of this work found no difference for $J_c(B)$ using κ-values of 10 or 100 (see figure 2 in Palonen *et al* (2012)).

Besides lower dimensional systems, vortex configurations in realistic mesoscopic samples arising from confinement effects were explored in Schweigert *et al* (1998), Schweigert and Peeters (1998), Baelus *et al* (2007) and Liu *et al* (2011). Recently, the dynamic response of narrow superconducting tapes and ribbons became of interest, where vortex structures are pinned by surface barriers and the third critical field, H_{c3}, plays an important role (Córdoba *et al* 2013, Vodolazov 2013).

A realistic description of the electromagnetic response of macroscopic three-dimensional superconductors was not possible until recently. A first step towards meaningful dynamics simulations of high-performance superconductors was conducted by Winiecki & Adams (Winiecki and Adams 2002b). Using a fast and reliable numerical method to approximate solutions of the TDGL equations (Winiecki and Adams 2002a), they simulated the vortex lattice motion in a moderately sized three-dimensional volume of size $(20\xi)^3$ and

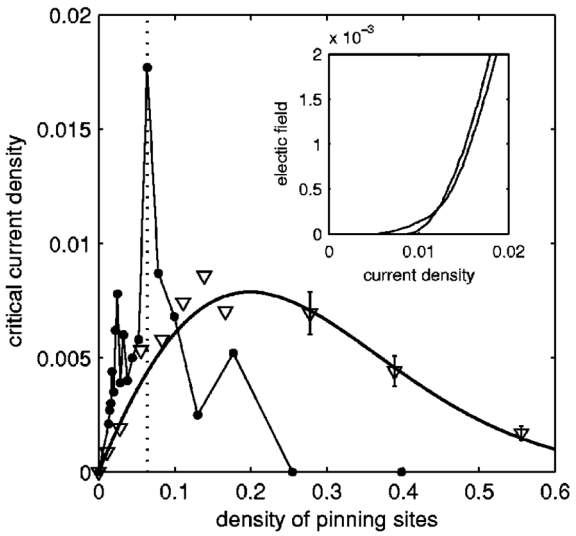

Figure 32. The critical current density as a function of the defect density (in units of ξ^2) for both random distributions (▽) and regular triangular arrays (Ш) for the 2D case. The data points are determined from an average of six random distributions. The error bars (shown for the high density distribution only) indicate the standard deviation. An example illustrating the effect of the distribution on the V–I curves is shown inset. The bold curve is a fit using the function $Ax\exp(-Bx)$, where A and B are fit parameters. The critical current density for a regular triangular array is a maximum when the pinning density is equal to vortex line density (indicated by the dotted line). (Reprinted figure with permission from Winiecki and Adams (2002b). Copyright (2002) by the American Physical Society.)

two-dimensional simulations (system size $60\xi \times 20\xi$) of random pinning sites and triangular lattices of pinning centers. Pinning was introduced by an artificial box/step potential in the Ginzburg–Landau free energy. Thermal fluctuations were not taken into account to ensure that the critical current has a well-defined value at the depinning transition. However, these efforts, carried out more than a decade ago, marked the beginning of numerical approaches to achieve large critical currents by predicting the underlying pinning configuration. In fact, Winiecki & Adams predicted the optimal density of pinning sites for a given type of pinning potential in the 2D case (see figure 32). The authors studied two different kind of pinning configurations: (i) random distribution of pinning centers of size 0.8ξ (potential height 2.0) and (ii) the same pinning centers arranged in a triangular array. The largest critical currents observed were 5% of the depairing current density in case (ii), but was sharply peaked around the corresponding defect density equal to the vortex line density. In the case (i) the optimal critical current was reduced by a factor of 2, and the maximum was more robust with respect to the defect density.

More recently, the optimal pinning by monodisperse spherical inclusions was investigated in Koshelev *et al* (2016). The simulated system size was $100\xi \times 100\xi \times 50\xi$ with $256 \times 256 \times 128$ mesh points. This system was much larger than any studied before, allowing for a more realistic simulation of the collective dynamics of the vortex matter and thermal fluctuations were taken into account as well. The current–voltage dependences for different particle sizes and densities were computed and used to evaluate the critical currents, J_c, which was defined by the criterion $E(J_c) = 0.02\rho_{ff}J_c$, where ρ_{ff} is the free flux-flow resistivity.

The pinning effectiveness of the particles was characterized by the volume fraction f occupied by them. At low densities the critical current always increased with f. Above a certain density, adding more particles started to degrade the critical current. This may be caused by jumping of vortex lines between the inclusions and/or by the reduction of the effective cross section available for the supercurrent due to the introduced normal fraction. Therefore, it is important to find the size and density of particles that maximizes the critical current.

Figure 33(a) shows the representative plots of the critical current J_c versus the particle volume fraction f for diameter $a = 4\xi$ and three magnetic fields. For every magnetic field, the critical current reaches a maximum at a certain volume fraction f. This optimal f increases with the magnetic field. Figure 33(b) shows the contour plot of the dependence of the critical current on the nonsuperconducting volume fraction f and particle diameter a for $B = 0.05H_{c2}$. One can see that the maximal critical current is realized at $a \approx 4.2\xi$ when approximately 20% of the total volume is replaced by the nonsuperconducting material. The optimal pinning parameters were determined for several magnetic fields. Figure 33(c) shows B-dependences of the optimal particle size a_{opt} and the maximum critical current $J_{c,max}$ achieved for the optimal parameters for $0.016H_{c2} < B < 0.2H_{c2}$. Within this range, the optimal diameter monotonically decreases with increasing magnetic field from $\sim 4.5\xi$ to $\sim 2.5\xi$. This indicates that the optimal scale of disorder has to be comparable with the typical distance between the vortices. The optimal volume fraction has a weak field dependence and stays within the range of 17–22% (not shown). Analysis of the pinned vortex configurations shows that at the optimal particle density only about 20% of the vortex-line length is located outside the particles. The maximum critical current drops from 12% of J_{dp} at smallest fields to 3% of J_{dp} at $B = 0.2H_{c2}$. A general observation is the absence of a universal optimal pinning configuration for all magnetic fields meaning that pinning landscapes should be designed taking into account the field range relevant for the specific applications.

Only a preliminary comparison of these results with experiment is possible at present since very few systematic studies of the particle density and size dependence of the critical current have been performed (Coll *et al* 2013, Miura *et al* 2013). While the particle density can be controlled by precursor composition, the particle size can only be changed within certain limits by tuning the fabrication process. It is clear that a clean scenario when only the particle density changes and everything else remains the same can never be realized in practice. In Coll *et al* (2013), pinning by Ba_2YTaO_6(BYTO) particles in solution derived YBCO films has been investigated. The particle size grows with density, from 15 nm for 3% molar percentage of BYTO to 40 nm for 15%. The diameter of 15 nm roughly corresponds to 4ξ at 77 K. A maximum pinning force at 77 K is realized at 6–10% of BYTO molar percentage (Coll *et al* 2013). The lower optimal density observed in experiment

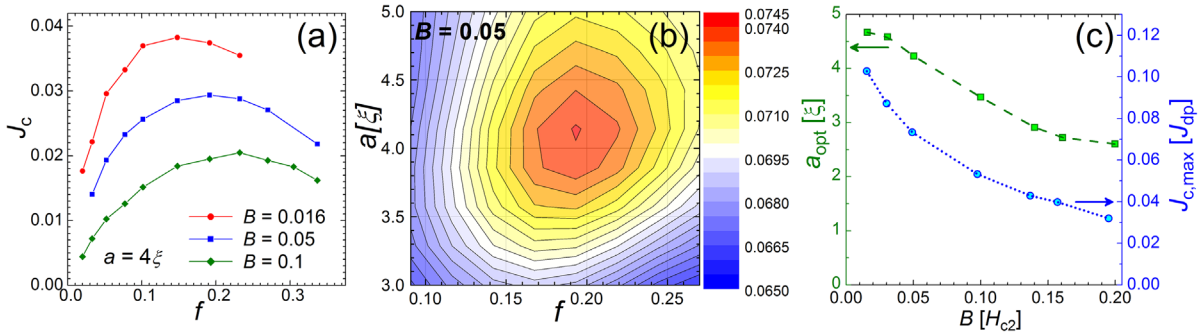

Figure 33. (a) The dependences of the critical current J_c on the particle volume fraction f for $a = 4\xi$ and three magnetic fields. (b) Contour plot of the critical current on the geometrical parameters f and a for $B = 0.05H_{c2}$. (c) The field dependence of the optimal particle diameter a_{opt} (right axis), and the maximum critical current $J_{c,max}$ realized for optimal parameters (left axis). The unit of current is the depairing current J_{dp}.

is most likely related to additional defects produced by the nanoparticles in the superconducting matrix, such as strain-induced dislocations or strain-distorted twin-boundaries (Guzman *et al* 2013). These defects pin the vortex segments outside the particles. Also, strain suppresses superconductivity. Both effects can contribute to the reduction of the optimal volume fraction with respect to theoretical values.

The pinning by $BaMO_3$ particles (M = Zr,Nb,Sn) in (Y,Gd)$Ba_2Cu_3O_y$ coated conductors has been investigated in Miura *et al* (2013). The average particle sizes vary for different compositions, ∼23 nm (∼6.2ξ at 77 K) for $BaZrO_3$, ∼41–43 nm (∼12ξ) for $BaSnO_3$, and ∼83 nm for $BaNbO_3$ (∼22ξ). Several particle densities were studied for each composition. The highest critical current has been observed for the smallest $BaZrO_3$ particles. For these particles, the critical current continued to grow with increasing particle density for all studied temperatures and fields (1 and 3 T for 65 K and 0.5 and 1 T for 77 K) indicating that the optimal density was not reached. However, the maximum volume fraction evaluated from their average size and density is rather small, only about 7.5%. We note also that the smallest particle size studied is still larger than the optimal size suggested by simulations.

Alternatively, the particlelike pinning centers in the form of defect clusters can be introduced by proton or ion irradiation, as described in section 3.2. Such defects are typically smaller than oxide nanoparticles, around 5 nm, and their concentration can be directly controlled by the irradiation dose. However, a systematic microstructural study of the shape and volume fraction of irradiation defects has not been performed yet. The critical current behaves nonmonotonically with irradiation dose and reaches a maximum at an optimal dose, see e.g. figure 22(c) for oxygen-ion irradiation. Furthermore, the optimal dose increases with increasing magnetic field and decreasing temperature. Note that the studied strong-pinning materials already contain many large-size pinning centers in the form of oxide precipitates, twin boundaries and dislocations. As a consequence, the irradiation defects only improve pinning at high magnetic fields and not at very high temperatures. Nevertheless the general trends of the optimal dose as function of magnetic field are in agreement with the simulated dependences on particle densities, see figure 33(a).

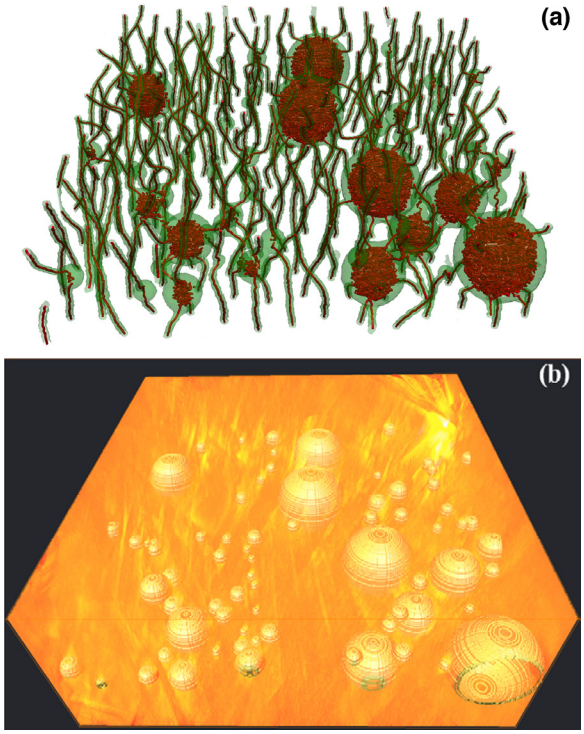

Figure 34. (a) Visualization of the vortex structure in a real sample obtained by large-scale TDGL simulations. Vortices (visualized by red tubes) were obtained using sophisticated detection methods (see Phillips *et al* (2015)). Inside inclusions, vortices cannot be uniquely defined anymore resulting in a dense arragement of loops. The semitransparent green isosurfaces represent a order parameter amplitude value of 0.3. The geometry of the defects matches the experimental one shown below. (b) Visualization of experimental sample volume together with the original reconstructed tomogram obtain by STEM tomography. (Reprinted from Ortalan *et al* (2009) (figure 5(b)). Copyright (2009), with permission from Elsevier.)

Using the same computational approach as in the paper mentioned above (described in Sadovskyy *et al* (2015)), it was recently possible to simulate the vortex dynamics in a 'real' pinning landscape. In Sadovskyy *et al* (2016b) large-scale TDGL simulations were combined with scanning transmission electron microscopy tomography of Dy-doped $YBa_2Cu_3O_{7-\delta}$. The latter allowed the reconstruction of the real three-dimensional pinning landscape of the experimentally

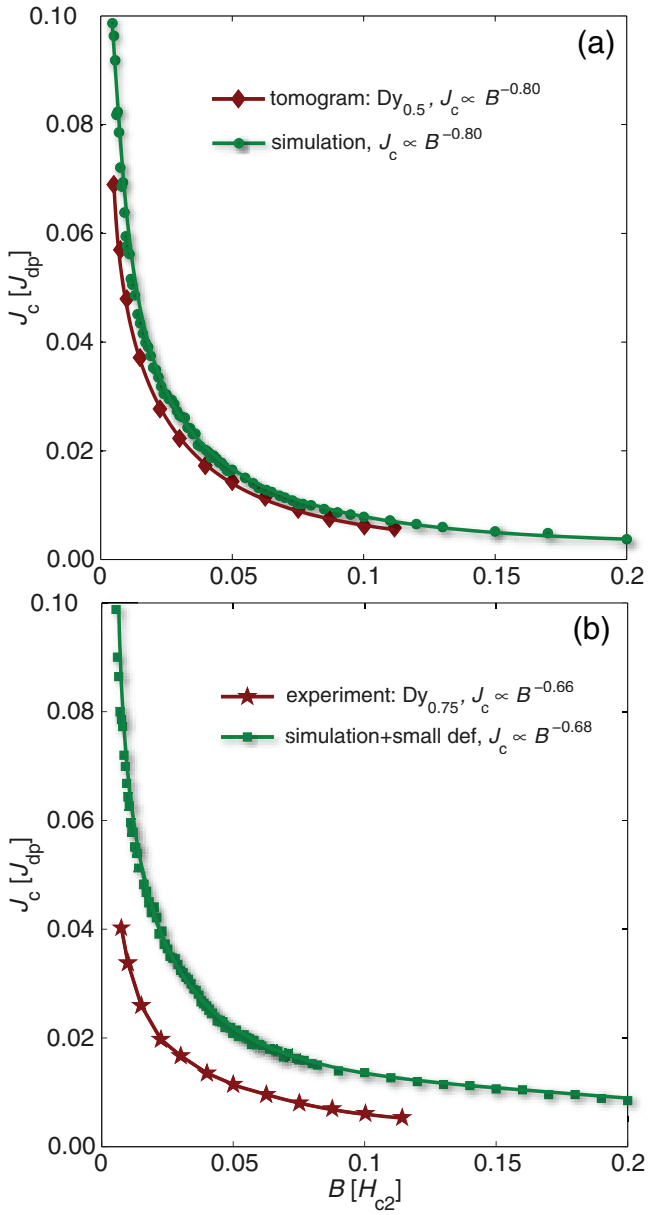

Figure 35. (a) Simulation results (green) for the field-dependence of the critical current of the sample in comparison to the experimentally obtained dependence (red). The simulation uses the defect geometry presented in Ortalan *et al* (2009) with Dy concentration 0.5. The corresponding measured data (red) is taken from Herrera *et al* (2008) (figure 1(b)). (b) Simulation result for the same geometry as in (a), but with added smaller defects. This addition of smaller defects corresponds to a higher Dy concentration of 0.75 in the experiment (red) (data from figure 1 of Ortalan *et al* (2009)). The exponents of the field dependence fit are in excellent agreement in both cases. The offset of the experimental curves compared to the simulation can be explained by the different criteria for the definition of the critical currents (see text). The simulation data is taken from Sadovskyy *et al* (2016b).

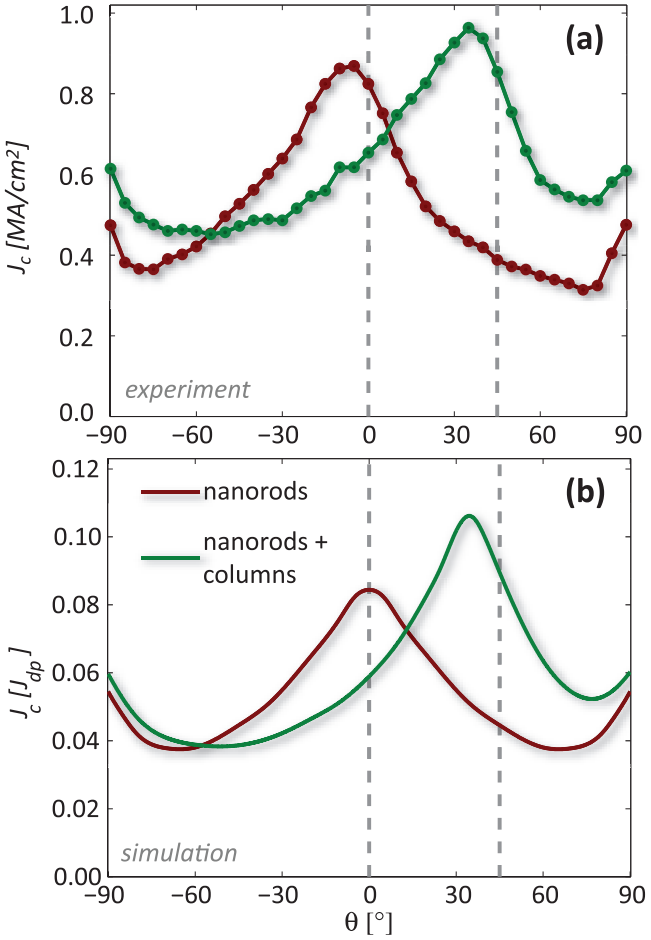

Figure 36. Angular field-dependence of the criticial current, J_c in REBCO coated conductor containing BZO nanorods (red curves). The broad peak in $J_c(\theta)$ around c-axis signals correlated pinning due to the nanorods. Upon heavy-ion irradiation at an angle of 45°, the enhanced pinning due to the BZO nanorods is wiped out and replaced by strong pinning due to irradiation tracks centered around 45° (green curves). (a) shows the experimental field-angle dependence of J_c and (b) corresponding TDGL simulations reproducing the dramatic non-additive change in pinning characteristics using realistic materials parameters. (See Sadovskyy *et al* (2016a))

measured sample (Herrera *et al* 2008, Ortalan *et al* 2009) (see figure 34(b)). This information was subsequently used to model the identical landscape as in the experimental system—down to the resolution limit of the tomography, using almost the same size as the sample.

The experimental system has a cuboid shape of size $534 \times 524 \times 129$ nm^3 and a Dy doping concentration of 0.5. Within this volume, seventy-one almost spherical particles with sizes ranging from 12.2 to 100 nm were reconstructed. The simulations were performed using a coherence length of $\xi = 4.2$ nm in the ab-plane, which is close to the experimental value at 77 K and an anisotropy factor of $\gamma = 5$ suitable for YBCO. The actual simulation volume was $L_x \times L_y \times L_z = 128\xi \times 128\xi \times 32\xi$, corresponding to $538 \times 538 \times 134$ nm^3, and is slightly larger than the real system. Sizes of the non-superconducting inclusions range from 2.90 to 23.8 (in units of ξ) and occupy about 8.1% of the simulated volume. Figure 34(a) shows a snapshot of the simulated vortex configuration of the sample at a fixed magnetic field.

Compared to the work on optimal pinning configurations for mono-disperse spherical particles (see above), one cannot expect that the simulated system in this case has an optimal

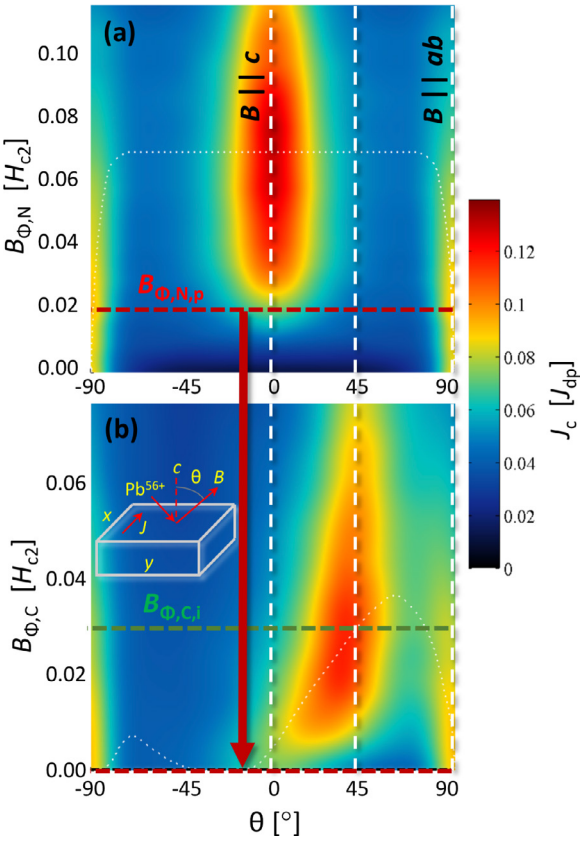

Figure 37. Prediction of the angular field-dependence of the critical current density obtained by TDGL simulations. (a) shows the dependence on the nanorod concentration, where the dashed red line indicates the concentration in the experiment ($B_{\phi,N,p}$), shown in figure 36 as red lines. (b) shows the dependence on the (irradiation) track concentration at a fixed $B_{\phi,N,p}$. The experimental concentration $B_{\phi,C,i}$, indicated by a dashed green line, corresponds to the green lines in figure 36. The inset shows the irradiation and measurement geometry. (See Sadovskyy *et al* (2016a))

pinning landscape—especially considering that the optimally-sized particles (3.5ξ to 4ξ) occupy only 0.8% of the volume. The main achievement of this work is that the simulated magnetic field dependence of the critical current is in good qualitative and almost quantitative functional agreement with the experimentally observed behavior, see figure 35(a). This work also suggests that more detailed STEM tomography studies could further improve the quantitative agreement—in particular if smaller defects could be detected, such as those introduced by higher Dy doping, then the measurements for a sample with Dy doping of 0.75 can be explained, see figure 35(b). Overall, this paper clearly shows that TDGL simulations are a valuable tool that can faithfully describe the dynamic properties of high-performance type-II superconductors with the potential for predictive capabilities and analysis.

Finally, we review numerical simulations of experiments on a commercial high-temperature superconducting tape containing well-controlled correlated defects (Sadovskyy *et al* 2016a). These rare earth barium copper oxide (REBCO) coated conductors contain pinning defects in the form of self-assembled barium zirconate (BZO) nanorods, see figure 15. There is a pronounced peak in the field-angle dependence of J_c around the *c*-axis (see figure 36(a) (red curve)) associated with the BZO nanorods. Such angular dependence of J_c can cause complications in applications such as motors and generators where the magnetic field orientation with respect to the windings are continuously changing. A potential remedy is to superimpose the pinning action of linear defects oriented at different angles to smooth out the angular dependence. To create such columnar defects at controlled angles, the sample was irradiated by 1.4 GeV Pb-ions at an angle of 45°. Surprisingly, the angular dependence of J_c resulting from the superposition of BZO nanorods and irradiation tracks is characterized by a single pronounced maximum at 45° due to the tracks and the pinning effect of the nanorods has been completely eliminated (figure 36(a) (green curve)).

The unexpected non-additive nature of the two types of pinning centers can be reproduced by TDGL simulations (figure 36(b)). Furthermore, the vortex mechanism responsible for this behavior can be visualized through simulations: vortices aligned with the BZO can easily jump from one nanorod to the next by sliding along the oblique columnar defects. This effect is directly responsible for the reduced critical current for magnetic field along the BZO nanorod direction.

The simulations go beyond reproducing the measured behavior—the concentration of BZO nanorods or columnar defects was varied in order to find optimal concentrations for the largest possible critical currents yielding 12–14% of J_{dp} in a limited angular range, see figure 37 ((a) shows the dependence on the nanorod concentration and (b) the dependence on the columnar track concentration). In the experiments ~1.5% of J_{dp} was reached, signaling significant headroom for further optimization. For all studied parameters, only a single peak in the critical current was observed rather than a superposition of the J_c-peaks due to the BZO nanorods at 0° and the irradiation tracks at 45°, indicating that mixed-pinning landscapes with different geometry—such as shown figure 12(a)—need to be implemented in order to alleviate the strong angular dependence of J_c.

The examples described above show that a quantitative prediction of the critical current of a superconductor from its microstructure is now within reach. These examples highlight the first steps towards this goal and demonstrate the emergence of a new paradigm: critical current by design. This concept suggests that TDGL simulations are a powerful method to design and predict optimal pinning landscapes that are robust with respect to small variations and can be used to further enhance the already high critical current density of high-performance superconductors (OSCon (2012–2017)).

5. Summary and outlook

In this review we demonstrate that a fundamental understanding of vortex matter in mixed-pinning landscapes requires a synergistic pursuit of theory, experiment and simulations. Recent studies indicate that particle irradiation that was used previously to probe vortex dynamics in single crystals can be an extremely useful tool to unravel the additive and competing vortex pinning effects among different defect morphologies

by tailoring the irradiation dose, the particle size and energy. Large-scale simulations are approaching levels whereby experimentally observed trends can be reproduced, thereby opening an avenue to identify the important factors in further optimizing vortex pinning and critical current. Furthermore, by relating experimental 3D TEM studies and bulk critical current measurements with large-scale time-dependent Ginzburg–Landau simulations on commercial HTS wires, a new paradigm has emerged in the form of 'critical current by design' which aims to provide predictive powers to determine the optimal vortex pinning landscape for targeted critical current in magnetic fields. These studies have so far revealed the non-additive interaction between correlated pinning defects in a mixed-pinning landscape, and their contribution to the macroscopic critical current. This provides the first step towards a solid formulation to design pinning landscapes with predictable critical currents for applications. From an applied perspective, recent work have demonstrated that the irradiation time to induce defects to enhance the critical current in commercial YBCO coated conductor wires can be greatly reduced, hinting at a viable reel-to-reel post production process to nearly double their critical current at high magnetic fields and at temperatures that are of interest in superconducting rotating machinery.

Acknowledgments

This work was supported by the U.S. Department of Energy (DOE), Office of Basic Energy Sciences, as part of the Center for Emergent Superconductivity Energy Frontier Research Center and by the Scientific Discovery through Advanced Computing (SciDAC) program funded by U.S. Department of Energy, Office of Science, Advanced Scientific Computing Research and Basic Energy Science. Some of the computational work presented here was performed on the GPU superconductors Cooley at the LCF at Argonne National Laboratory and on GAEA at Northern Illinois University.

References

Abraimov D *et al* 2015 Double disordered YBCO coated conductors of industrial scale: high currents in high magnetic field *Supercond. Sci. Technol.* **28** 114007

Abrikosov A A 1957 On the magnetic properties of superconductors of the second group *Sov. Phys.—JETP* **5** 1174 (Abrikosov A A 1957 *Zh. Eksp. Teor. Fiz.* 32 1442)

Abrikosov A A and Gor'kov L P 1960 Contribution to the theory of superconducting alloys with paramagnetic impurities *Zh. Eksp. Teor. Fiz.* **39** 1781 (Abrikosov A A and Gor'kov L P 1961 *Sov. Phys.—JETP* 12 1243)

Aladyshkin A Y, Silhanek A V, Gillijns W and Moshchalkov V V 2009 Nucleation of superconductivity and vortex matter in superconductor-ferromagnet hybrids *Supercond. Sci. Technol.* **22** 053001

Alden T H and Livingston J D 1966a Ferromagnetic particles in a type-II superconductor *J. Appl. Phys.* **37** 3551–6

Alden T H and Livingston J D 1966b Magnetic pinning in a type-II superconductor *Appl. Phys. Lett.* **8** 6–7

Anderson P W 1959 Theory of dirty superconductors *J. Phys. Chem. Solids* **11** 26

Anderson P W and Kim Y B 1964 Hard superconductivity: theory of the motion of Abrikosov flux lines *Rev. Mod. Phys.* **36** 39–43

Aranson I S and Kramer L 2002 The world of the complex Ginzburg–Landau equation *Rev. Mod. Phys.* **74** 99

Averback R and de la Rubia T D 1997 Displacement damage in irradiated metals and semiconductors *Solid State Phys.* **51** 281–402

Averback R S, Benedek R and Merkle K L 1978 Correlations between ion and neutron irradiations: defect production and stage I recovery *J. Nucl. Mater.* **75** 162–6

Awaji S, Yoshida Y, Suzuki T, Watanabe K, Hikawa K, Ichino Y and Izumi T 2015 High-performance irreversibility field and flux pinning force density in $BaHfO_3$-doped $GdBa_2Cu_3O_y$ tape prepared by pulsed laser deposition *Appl. Phys. Express* **8** 023101

Baelus B J, Sun D and Peeters F M 2007 Vortex structures in mesoscopic superconducting spheres *Phys. Rev.* B **75** 174523

Balatsky A V, Vekhter I and Zhu J-X 2006 Impurity-induced states in conventional and unconventional superconductors *Rev. Mod. Phys.* **78** 373–433

Barone A and Paterno G 1982 *Physics and Applications of the Josephson Effect* (New York: Wiley)

Bean C P 1964 Magnetization of high-field superconductors *Rev. Mod. Phys.* **36** 31–9

Blatter G and Geshkenbein V B 2003 *The Physics of Superconductors* (*Conventional and High-T_c Superconductors* vol 1) (Berlin: Springer)

Blatter G, Feigelman M V, Geshkenbein V B, Larkin A I and Vinokur V M 1994 Vortices in high-temperature superconductors *Rev. Mod. Phys.* **66** 1125

Blatter G, Geshkenbein V B and Koopmann J A G 2004 Weak to strong pinning crossover *Phys. Rev. Lett.* **92** 067009

Brandt E 1983a Computer simulation of vortex pinning in type II superconductors. I. Two-dimensional simulation *J. Low Temp. Phys.* **53** 41–70

Brandt E 1983b Computer simulation of vortex pinning in type II superconductors. II. Random point pins *J. Low Temp. Phys.* **53** 71–152

Brandt E H 1995 The flux-line-lattice in superconductors *Rep. Prog. Phys.* **58** 1465

Brandt E H 1996 Universality of flux creep in superconductors with arbitrary shape and current–voltage law *Phys. Rev. Lett.* **76** 4030–3

Bringa E M and Johnson R E 2002 Coulomb explosion and thermal spikes *Phys. Rev. Lett.* **88** 165501

Brown S P, Charalambous D, Jones E C, Forgan E M, Kealey P G, Erb A and Kohlbrecher J 2004 Triangular to square flux lattice phase transition in $YBa_2Cu_3O_7$ *Phys. Rev. Lett.* **92** 067004

Bustingorry S, Cugliandolo L F and Domínguez D 2007 Langevin simulations of the out-of-equilibrium dynamics of vortex glasses in high-temperature superconductors *Phys. Rev.* B **75** 024506

Campbell A M and Evetts J E 1972 Flux vortices and transport currents in type II superconductors *Adv. Phys.* **21** 199–428

Cao Y, Jiao Z and Ying H 2000 Numerical study on the dynamics of a driven disordered vortex lattice *Phys. Rev.* B **62** 4163–8

Choi S M, Lee J W, Shin G H, Lee J H, Hong G W, Moon S H and Yoo S I 2013 Characteristics of high- J_c GdBCO coated conductors fabricated by the RCE-DR process *IEEE Trans. Appl. Supercond.* **23** 8001004

Chudy M, Zhong Z, Eisterer M and Coombs T 2015 n-values of commercial YBCO tapes before and after irradiation by fast neutrons *Supercond. Sci. Technol.* **28** 035008

Civale L 1997 Vortex pinning and creep in high-temperature superconductors with columnar defects *Supercond. Sci. Technol.* **10** A11

Civale L *et al* 2004 Angular-dependent vortex pinning mechanisms in $YBa_2Cu_3O_7$ coated conductors and thin films *Appl. Phys. Lett.* **84** 2121–3

Clark G J, Marwick A D, Koch R H and Laibowitz R B 1987 Effects of radiation damage in ion-implanted thin films of metal-oxide superconductors *Appl. Phys. Lett.* **51** 139–41

Clark G, Marwick A, Legoues F, Laibowitz R, Koch R and Madakson P 1988 Radiation effects in thin films of high T_c superconductors *Nucl. Instrum. Methods Phys. Res.* B **32** 405–11

Civale L, Marwick A D, McElfresh M W, Worthington T K, Malozemoff A P, Holtzberg F H, Thompson J R and Kirk M A 1990 Defect independence of the irreversibility line in proton-irradiated Y-Ba-Cu-O crystals *Phys. Rev. Lett.* **65** 1164–7

Civale L, Marwick A D, Worthington T K, Kirk M A, Thompson J R, Krusin-Elbaum L, Sun Y, Clem J R and Holtzberg F 1991 Vortex confinement by columnar defects in $YBa_2Cu_3O_7$ crystals: enhanced pinning at high fields and temperatures *Phys. Rev. Lett.* **67** 648–51

Coll M, Ye S, Rouco V, Palau A, Guzman R, Gazquez J, Arbiol J, Suo H, Puig T and Obradors X 2013 Solution-derived $YBa_2Cu_3O_7$ nanocomposite films with a Ba_2YTaO_6 secondary phase for improved superconducting properties *Supercond. Sci. Technol.* **26** 015001

Conner L W and Malozemoff A P 1991 Calculations of the dimensional dependence of the critical state in disk-shaped superconductors *Phys. Rev.* B **43** 402–7

Córdoba R *et al* 2013 Magnetic field-induced dissipation-free state in superconducting nanostructures *Nat. Commun.* **4** 1437

Crabtree G W and Nelson D R 1997 Vortex physics in high-temperature superconductors *Phys. Today* **50** 38–45

Crabtree G W, Gunter D O, Kaper H G, Koshelev A E, Leaf G K and Vinokur V M 2000 Numerical simulations of driven vortex systems *Phys. Rev.* B **61** 1446–55

Däumling M and Larbalestier D C 1989 Critical state in disk-shaped superconductors *Phys. Rev.* B **40** 9350–3

De Wilde Y, Iavarone M, Welp U, Metlushko V, Koshelev A E, Aranson I, Crabtree G W and Canfield P C 1997 Scanning tunneling microscopy observation of a square Abrikosov lattice in $LuNi_2B_2C$ *Phys. Rev. Lett.* **78** 4273–6

Dimos D, Chaudhari P and Mannhart J 1990 Superconducting transport properties of grain boundaries in $YBa_2Cu_3O_7$ bicrystals *Phys. Rev.* B **41** 4038–49

Dimos D, Chaudhari P, Mannhart J and Legoues F K 1988 Orientation dependance of grain-boundary critical currents in $YBa_2Cu_3O_{7-\delta}$ bicrystals *Phys. Rev. Lett.* **61** 219

Dobramysl U, Assi H, Pleimling M and Täuber U 2013 Relaxation dynamics in type-II superconductors with point-like and correlated disorder *Eur. Phys. J.* B **86** 228

Dong X, An P, Zhang J, Zhang H, Li Y, Liu H, Ge X and Li Q 2014 Superconductivity enhancement in Fe_3O_4 doped $YBa_2Cu_3O_{7\delta}$ *J. Supercond. Novel Magn.* **27** 693–9

Doria M M, Romaguera A R de C, Milošević M V and Peeters F M 2007 Threefold onset of vortex loops in superconductors with a magnetic core *Europhys. Lett.* **79** 47006

Du Q 1994 Finite element methods for the time-dependent Ginzburg–Landau model of superconductivity *Comput. Math. Appl.* **27** 119–33

Durrell J H, Eom C-B, Gurevich A, Hellstrom E E, Tarantini C, Yamamoto A and Larbalestier D C 2011 The behavior of grain boundaries in the Fe-based superconductors *Rep. Prog. Phys.* **74** 124511

Eisterer M, Weber H W, Jiang J, Weiss J D, Yamamoto A, Polyanskii A A, Hellstrom E E and Larbalestier D C 2009 Neutron irradiation of $SmFeAsO_{1-x}F_x$ *Supercond. Sci. Technol.* **22** 065015

Eley S, Leroux M, Rupich M W, Miller D J, Sheng H, Niraula P M, Kayani A, Welp U, Kwok W-K and Civale L 2016 Decoupling and tuning competing effects of different types of defects on flux creep in irradiated $YBa_2Cu_3O_{7-\delta}$ coated conductors (arXiv:1602.04344)

Emig T, Bogner S and Nattermann T 1999 Nonuniversal quasi-long-range order in the glassy phase of impure superconductors *Phys. Rev. Lett.* **83** 400–3

Ertaş D and Kardar M 1996 Anisotropic scaling in threshold critical dynamics of driven directed lines *Phys. Rev.* B **53** 3520–42

Ertaş D and Nelson D R 1996 Irreversibility, mechanical entanglement and thermal melting in superconducting vortex crystals with point impurities *Physica* C **272** 79–86

Fang L *et al* 2012 High, magnetic field independent critical currents in $(Ba,K)Fe_2As_2$ crystals *Appl. Phys. Lett.* **101** 012601

Fang L *et al* 2013 Huge critical current density and tailored superconducting anisotropy in $SmFeAsO_{0.8}F_{0.15}$ by low-density columnar-defect incorporation *Nat. Commun.* **4** 2655

Fang L, Jia Y, Schlueter J A, Kayani A, Xiao Z L, Claus H, Welp U, Koshelev A E, Crabtree G W and Kwok W-K 2011 Doping- and irradiation-controlled pinning of vortices in $BaFe_2(As_{1-x}P_x)_2$ single crystals *Phys. Rev.* B **84** 140504

Fangohr H, Cox S J and de Groot P A J 2001 Vortex dynamics in two-dimensional systems at high driving forces *Phys. Rev.* B **64** 064505

Feigel'man M V, Geshkenbein V B, Larkin A I and Vinokur V M 1989 Theory of collective flux creep *Phys. Rev. Lett.* **63** 2303–6

Fily Y, Olive E, Di Scala N and Soret J C 2010 Critical behavior of plastic depinning of vortex lattices in two dimensions: molecular dynamics simulations *Phys. Rev.* B **82** 134519

Fisher M P A 1989 Vortex-glass superconductivity: a possible new phase in bulk high-T_c oxides *Phys. Rev. Lett.* **62** 1415–8

Fischer O, Kugler M, Maggio-Aprile I, Berthod C and Renner C 2007 Scanning tunneling spectroscopy of high-temperature superconductors *Rev. Mod. Phys.* **79** 353–419

Fleischer R L, Price P B and Walker R M 1965 Tracks of charged particles in solids *Science* **149** 383–93

Foltyn S R, Civale L, Macmanus-Driscoll J L, Jia Q X, Maiorov B, Wang H and Maley M 2007 Materials science challenges for high-temperature superconducting wire *Nat. Mater.* **6** 631–42

Fruchter L 2002 Transition to plastic motion as a critical phenomenon and anomalous interface layer of a 2D driven vortex lattice *Eur. Phys. J.* B **25** 313–7

Gao H and Sun W 2015 An efficient fully linearized semi-implicit Galerkin-mixed {FEM} for the dynamical Ginzburg–Landau equations of superconductivity *J. Comput. Phys.* **294** 329–45

Gapud A A, Greenwood N T, Alexander J A, Khan A, Leonard K J, Aytug T, List F A, Rupich M W and Zhang Y 2015 Irradiation response of commercial, high-T_c superconducting tapes: electromagnetic transport properties *J. Nucl. Mater.* **462** 108–13

Gapud A A, Kumar D, Viswanathan S K, Cantoni C, Varela M, Abiade J, Pennycook S J and Christen D K 2005 Enhancement of flux pinning in $YBa_2Cu_3O_{7-\delta}$ thin films embedded with epitaxially grown Y_2O_3 nanostructures using a multi-layering process *Supercond. Sci. Technol.* **18** 1502–5

Giamarchi T and Le Doussal P 1995 Elastic theory of flux lattices in the presence of weak disorder *Phys. Rev.* B **52** 1242–70

Goeckner H, Olson R, Kwok W, Claus H and Kouvel J 2003 Effects of Pb-ion irradiation on the vortex pinning in melt-textured $YBa_2Cu_3O_x$ *Physica* C **390** 291–5

Gor'kov L P 1959 Microscopic derivation of the Ginzburg–Landau equations in the theory of superconductivity *Sov. Phys.—JETP* **9** 1364–7

Gor'kov L P and Éliashberg G M 1968 Generalization of the Ginzburg–Landau equations for non-stationary problems in the case of alloys with paramagnetic impurities *Sov. Phys.—JETP* **27** 328

Goyal A *et al* 2005 Irradiation-free, columnar defects comprised of self-assembled nanodots and nanorods resulting in strongly enhanced flux-pinning in $YBa_2Cu_3O_{7-\delta}$ films *Supercond. Sci. Technol.* **18** 1533–8

Grønbech-Jensen N, Bishop A R and Domínguez D 1996 Metastable filamentary vortex flow in thin film superconductors *Phys. Rev. Lett.* **76** 2985–8

Gropp W D, Kaper H G, Leaf G K, Levine D M, Palumbo M and Vinokur V M 1995 Numerical simulation of vortex dynamics in type-II superconductors *J. Comput. Phys.* **123** 254–66

Gunter D O, Kaper H G and Leaf G K 2002 Implicit integration of the time-dependent Ginzburg–Landau equations of superconductivity *SIAM J. Sci. Comput.* **23** 1943–58

Gurevich A 2011 To use or not to use cool superconductors? *Nat. Mater.* **10** 255–9

Gurevich A 2014 Challenges and opportunities for applications of unconventional superconductors *Annu. Rev. Condens. Matter Phys.* **5** 35–56

Gutierrez J *et al* 2007 Strong isotropic flux pinning in solution-derived $YBa_2Cu_3O_{7-x}$ nanocomposite superconductor films *Nat. Mater.* **6** 367–73

Guzman R, Gazquez J, Rouco V, Palau A, Magen C, Varela M, Arbiol J, Obradors X and Puig T 2013 Strain-driven broken twin boundary coherence in $YBa_2Cu_3O_{7-\delta}$ nanocomposite thin films *Appl. Phys. Lett.* **102** 081906

Gyorgy E M, van Dover R B, Jackson K A, Schneemeyer L F and Waszczak J V 1989 Anisotropic critical currents in $Ba_2YCu_3O_7$ analyzed using an extended bean model *Appl. Phys. Lett.* **55** 283–5

Haberkorn N *et al* 2012b High-temperature change of the creep rate in $YBa_2Cu_3O_{7-\delta}$ films with different pinning landscapes *Phys. Rev.* B **85** 174504

Haberkorn N, Kim J, Gofryk K, Ronning F, Sefat A S, Fang L, Welp U, Kwok W K and Civale L 2015a Enhancement of the critical current density by increasing the collective pinning energy in heavy ion irradiated Co-doped $BaFe_2$ As_2 single crystals *Supercond. Sci. Technol.* **28** 055011

Haberkorn N, Kim J, Maiorov B, Usov I, Chen G F, Yu W and Civale L 2014 Increment of the collective pinning energy in $Na_{1-x}Ca_xFe_2As_2$ single crystals with random point defects introduced by proton irradiation *Supercond. Sci. Technol.* **27** 095004

Haberkorn N, Kim J, Suárez S, Lee J-H and Moon S H 2015b Influence of random point defects introduced by proton irradiation on the flux creep rates and magnetic field dependence of the critical current density J_c of co-evaporated $GdBa_2Cu_3O_{7-\delta}$ coated conductors *Supercond. Sci. Technol.* **28** 125007

Haberkorn N, Maiorov B, Usov I O, Weigand M, Hirata W, Miyasaka S, Tajima S, Chikumoto N, Tanabe K and Civale L 2012a Influence of random point defects introduced by proton irradiation on critical current density and vortex dynamics of $Ba(Fe_{0.925}Co_{0.075})_2As_2$ single crystals *Phys. Rev.* B **85** 014522

Hardy V, Groult D, Hervieu M, Provost J, Raveau B and Bouffard S 1991 Latent track formation induced by high energy heavy ions in superconductive copper oxides *Nucl. Instrum. Methods Phys. Res.* B **54** 472–81

Haugan T 2015 Viewpoint on fast track communication by V Selvamanickam *et al* : critical current density above 15 MA cm^{-2} at 30 K, 3 T in 2.2 μm thick heavily-doped (Gd,Y) $Ba_2Cu_3O_x$ superconductor tapes *Supercond. Sci. Technol.* **28** 090502

Haugan T, Barnes P N, Wheeler R, Meisenkothen F and Sumption M 2004 Addition of nanoparticle dispersions to enhance flux pinning of the $YBa_2Cu_3O_{7-x}$ superconductor *Nature* **430** 867–70

Hazelton D, Zhang Y, Knoll A and Sakamoto H 2015 Continuous improvement at superpower of 2G HTS wire for demanding applications *CEC-ICMC (Tuscon, AZ, USA, 28 June–2 July 2015)*

Hengstberger F, Eisterer M and Weber H W 2010 Thickness dependence of the critical current density in superconducting films: a geometrical approach *Appl. Phys. Lett.* **96** 022508

Herrera M, Ortalan V, Morgan D G, Browning N D and Rupich M W 2008 Observation of the three-dimensional distribution of flux pinning centers in dy-doped $YBa_2Cu_3O_{7-x}$ coated conductors *J. Appl. Phys.* **103** 084301

High-field National Laboratory webpage 2015 Applied superconductivity center (https://nationalmaglab.org/magnet-development/applied-superconductivity-center/plots)

Hilgenkamp H and Mannhart J 2002 Grain boundaries in high-T_c superconductors *Rev. Mod. Phys.* **74** 485–549

Hoffman J E 2011 Spectroscopic scanning tunneling microscopy insights into Fe-based superconductors *Rep. Prog. Phys.* **74** 124513

Horide T, Kawamura T, Matsumoto K, Ichinose A, Yoshizumi M, Izumi T and Shiohara Y 2013 J_c improvement by double artificial pinning centers of $BaSnO_3$ nanorods and Y_2O_3 nanoparticles in $YBa_2Cu_3O_7$ coated conductors *Supercond. Sci. Technol.* **26** 075019

Hosono H and Kuroki K 2015 Iron-based superconductors: current status of materials and pairing mechanism *Physica* C **514** 399–422

Hosono H, Tanabe K, Takayama-Muromachi E, Kageyama H, Yamanaka S, Kumakura H, Nohara M, Hiramatsu H and Fujitsu S 2015 Exploration of new superconductors and functional materials, and fabrication of superconducting tapes and wires of iron pnictides *Sci. Technol. Adv. Mater.* **16** 033503

Houghton A, Pelcovits R A and Sudbø A 1989 Flux lattice melting in high-T_c superconductors *Phys. Rev.* B **40** 6763–70

Iida K *et al* 2011 Epitaxial growth of superconducting $Ba(Fe_{1-x}Co_x)_2As_2$ thin films on technical ion beam assisted deposition MgO substrates *Appl. Phys. Express* **4** 013103

Iida K *et al* 2014 Highly textured oxypnictide superconducting thin films on metal substrates *Appl. Phys. Lett.* **105** 1–4

Iwase A, Masaki N, Iwata T, Sasaki S and Nihira T 1988 Effect of 120 MeV O-16 ion irradiation at low temperatures on superconducting properties of $YBa_2Cu_3O_{(7-x)}$ and $La_{(1.8)}Sr_{(0.2)}CuO_4$ *Japan. J. Appl. Phys.* **27** L2071–4

Jäger W and Merkle K L 1988 Defect-cluster formation in high-energy-density cascades in gold *Phil. Mag.* A **57** 479–98

Jensen H J, Brass A and Berlinsky A J 1988 Lattice deformations and plastic flow through bottlenecks in a two-dimensional model for flux pinning in type-II superconductors *Phys. Rev. Lett.* **60** 1676–9

Jia Y *et al* 2013 Doubling the critical current density of high temperature superconducting coated conductors through proton irradiation *Appl. Phys. Lett.* **103** 122601

Johnston D C 2010 The puzzle of high temperature superconductivity in layered iron pnictides and chalcogenides *Adv. Phys.* **59** 803–1061

Kamihara Y, Watanabe T, Hirano M and Hosono H 2008 Iron-based layered superconductor $La[O_{1-x}F_x]FeAs$ ($x = 0.05$–0.12) with $T_c = 26$ K *J. Am. Chem. Soc.* **130** 3296–7

Kang S *et al* 2006 High-performance high-T_c superconducting wires *Science* **311** 1911–4

Katase T, Hiramatsu H, Matias V, Sheehan C, Ishimaru Y, Kamiya T, Tanabe K and Hosono H 2011 Biaxially textured cobalt-doped $BaFe_2As_2$ films with high critical current density over 1 MA cm^{-2} on MgO-buffered metal-tape flexible substrates *Appl. Phys. Lett.* **98** 242510

Katase T, Ishimaru Y, Tsukamoto A, Hiramatsu H, Kamiya T, Tanabe K and Hosono H 2010 Josephson junction in cobalt-doped $BaFe_2As_2$ epitaxial thin films on (La,Sr)(Al,Ta)O_3 bicrystal substrates *Appl. Phys. Lett.* **96** 142507

Kihlstrom K J *et al* 2013 High-field critical current enhancement by irradiation induced correlated and random defects in $(Ba_{0.6}K_{0.4})$ Fe_2As_2 *Appl. Phys. Lett.* **103** 202601

Kim H *et al* 2010 London penetration depth and superfluid density of single-crystalline $Fe_{1+y}(Te_{1-x}Se_x)$ and $Fe_{1+y}(Te_{1-x}S_x)$ *Phys. Rev.* B **81** 180503

Kinchin G H and Pease R S 1955 The displacement of atoms in solids by radiation *Rep. Prog. Phys.* **18** 1

Kirk M A 1993 Structure and flux pinning properties of irradiation defects in $YBa_2Cu_3O_{7-x}$ *Cryogenics* **33** 235–42

Kirk M and Yan Y 1999 Structure and properties of irradiation defects in $YBa_2Cu_3O_{7-x}$ *Micron* **30** 507–26

Koch C C and Love G R 1969 Superconductivity in niobium containing ferromagnetic gadolinium or paramagnetic yttrium dispersions *J. Appl. Phys.* **40** 3582–7

Konczykowski M, Rullier-Albenque F, Yacoby E R, Shaulov A, Yeshurun Y and Lejay P 1991 Effect of 5.3 GeV Pb-ion irradiation on irreversible magnetization in Y-Ba-Cu-O crystals *Phys. Rev.* B **44** 7167–70

Koshelev A 1992 Numerical simulation of thermal depinning for two-dimensional vortex system *Physica* C **198** 371–7

Koshelev A E and Kolton A B 2011 Theory and simulations on strong pinning of vortex lines by nanoparticles *Phys. Rev.* B **84** 104528

Koshelev A E and Nordborg H 1999 Universal properties for linelike melting of the vortex lattice *Phys. Rev.* B **59** 4358–63

Koshelev A E and Vinokur V M 1994 Dynamic melting of the vortex lattice *Phys. Rev. Lett.* **73** 3580–3

Koshelev A E, Sadovskyy I A, Phillips C L and Glatz A 2016 Optimization of vortex pinning by nanoparticles using simulations of the time-dependent Ginzburg–Landau model *Phys. Rev.* B **93** 060508

Krasheninnikov A V and Nordlund K 2010 Ion and electron irradiation-induced effects in nanostructured materials *J. Appl. Phys.* **107** 071301

Lang M, Devanathan R, Toulemonde M and Trautmann C 2015 Advances in understanding of swift heavy-ion tracks in complex ceramics *Curr. Opin. Solid State Mater. Sci.* **19** 39–48

Larbalestier D C *et al* 2014 Isotropic round-wire multifilament cuprate superconductor for generation of magnetic fields above 30 t *Nat. Mater.* **13** 375–81

Larbalestier D, Gurevich A, Feldmann D M and Polyanskii A 2001 High-T_c superconducting materials for electric power applications *Nature* **414** 368–77

Larkin A I and Ovchinnikov Y N 1979 Pinning in type II superconductors *J. Low Temp. Phys.* **34** 409

Larkin A I and Varlamov A A 2005 *Theory of Fluctuations in Superconductors* (Oxford: Oxford University Press)

Lee P J and Larbalestier D C 2001 Niobium–titanium superconducting wires: nanostructures by extrusion and wire drawing *Invited Presentation at Interwire (Atlanta, GA)*

Lee P J and Larbalestier D C 2008 Microstructural factors important for the development of high critical current density Nb_3Sn strand *Cryogenics* **48** 283–92 (special issue: Low-T_c superconducting materials)

Lee S *et al* 2009 Weak-link behavior of grain boundaries in superconducting $Ba(Fe_{1-x}Cox)_2As_2$ bicrystals *Appl. Phys. Lett.* **95** 2009–11

Lee S *et al* 2010 Template engineering of Co-doped $BaFe_2As_2$ single-crystal thin films *Nat. Mater.* **9** 397–402

Leonard K J, Aytug T, Gapud A A, List F A III, Greenwood N T, Zhang Y, Perez-Bergquist A G and Weber W J 2014 Irradiation response of next generation high temperature superconductors for fusion energy applications *Fusion Sci. Technol.* **66** 57

Leonard K J, Aytug T, List F A III, Perez-Bergquist A, Weber W J and Gapud A 2013a Irradiation response of next generation high temperature superconducting rare earth and nanoparticle-doped $YBa_2Cu_3O_{7-x}$ coated conductors for fusion energy applications *Fusion Reactor Materials Program (DOE/ER-0313/55, 31 December 2013)* vol 54, pp 125–34

Leonard K J, Aytug T, List F A III, Perez-Bergquist A, Weber W J and Gapud A 2013b Irradiation response of next generation high temperature superconducting rare earth and nanoparticle-doped $YBa_2Cu_3O_{7-x}$ coated conductors for fusion energy applications *Fusion Reactor Materials Program (DOE/ER-0313/55, 31 December 2013)* vol 55, p 54

Leroux M *et al* 2015 Rapid doubling of the critical current of $YBa_2Cu_3O_{7-\delta}$ coated conductors for viable high-speed industrial processing *Appl. Phys. Lett.* **107** 192601

Li B and Zhang Z 2015 A new approach for numerical simulation of the time-dependent Ginzburg–Landau equations *J. Comput. Phys.* **303** 238–50

Liu C-Y, Berdiyorov G R and Milošević M V 2011 Vortex states in layered mesoscopic superconductors *Phys. Rev.* B **83** 104524

Llordés A *et al* 2012 Nanoscale strain-induced pair suppression as a vortex-pinning mechanism in high-temperature superconductors *Nat. Mater.* **11** 329–36

Luo M B and Hu X 2007 Depinning and creep motion in glass states of flux lines *Phys. Rev. Lett.* **98** 267002

Luo M B and Hu X 2010 Creep of driven flux lines in type-II superconductors *J. Supercond. Novel Magn.* **23** 1055–7

Lyuksyutov I F and Pokrovsky V L 2005 Ferromagnet-superconductor hybrids *Adv. Phys.* **54** 67–136

Ma Y 2015 Development of high-performance iron-based superconducting wires and tapes *Physica* C **516** 17–26

MacManus-Driscoll J L, Foltyn S R, Jia Q X, Wang H, Serquis A, Civale L, Maiorov B, Hawley M E, Maley M P and Peterson D E 2004 Strongly enhanced current densities in superconducting coated conductors of $YBa_2Cu_3O_{7-x} + BaZrO_3$ *Nat. Mater.* **3** 439–43

Maiorov B, Baily S A, Zhou H, Ugurlu O, Kennison J A, Dowden P C, Holesinger T G, Foltyn S R and Civale L 2009 Synergetic combination of different types of defect to optimize pinning landscape using $BaZrO_3$-doped $YBa_2Cu_3O_7$ *Nat. Mater.* **8** 398–404

Maiorov B, Katase T, Usov I O, Weigand M, Civale L, Hiramatsu H and Hosono H 2012 Competition and cooperation of pinning by extrinsic point-like defects and intrinsic strong columnar defects in $BaFe_2As_2$ thin films *Phys. Rev.* B **86** 094513

Maley M P, Willis J O, Lessure H and McHenry M E 1990 Dependence of flux-creep activation energy upon current density in grain-aligned $YBa_2Cu_3O_{7-x}$ *Phys. Rev.* B **42** 2639–42

Malozemoff A P 2012 Second-generation high-temperature superconductor wires for the electric power grid *Annu. Rev. Mater. Res.* **42** 373–97

Malozemoff A P and Fisher M P A 1990 Universality in the current decay and flux creep of Y-Ba-Cu-O high-temperature superconductors *Phys. Rev.* B **42** 6784–6

Massee F, Sprau P O, Wang Y L, Davis J C S, Ghigo G, Gu G D and Kwok W-K 2015 Imaging atomic-scale effects of high-energy ion irradiation on superconductivity and vortex pinning in Fe(Se,Te) *Sci. Adv.* **1** e1500033

Matsui H, Ogiso H, Yamasaki H, Kumagai T, Sohma M, Yamaguchi I and Manabe T 2012 4-fold enhancement in the critical current density of $YBa_2Cu_3O_7$ films by practical ion irradiation *Appl. Phys. Lett.* **101** 232601

Matsui H, Ogiso H, Yamasaki H, Sohma M, Yamaguchi I, Kumagai T and Manabe T 2014 Influence of middle-energy ion-irradiation on the flux pinning properties of YBCO films: comparison between different synthesis methods *J. Phys.: Conf. Ser.* **507** 022019

Matsumoto K and Mele P 2009 Artificial pinning center technology to enhance vortex pinning in YBCO coated conductors *Supercond. Sci. Technol.* **23** 014001

Matsumoto K, Horide T, Ichinose A, Horii S, Yoshida Y and Mukaida M 2005 Critical current control in $YBa_2Cu_3O_{7-\delta}$ films using artificial pinning centers *Japan. J. Appl. Phys.* **44** L246

Mele P, Matsumoto K, Horide T, Ichinose A, Mukaida M, Yoshida Y, Horii S and Kita R 2008 Ultra-high flux pinning properties of $BaMO_3$-doped $YBa_2Cu_3O_{7-x}$ thin films (M = Zr, Sn) *Supercond. Sci. Technol.* **21** 032002

Mishev V, Zehetmayer M, Fischer D X, Nakajima M, Eisaki H and Eisterer M 2015 Interaction of vortices in anisotropic superconductors with isotropic defects *Supercond. Sci. Technol.* **28** 102001

Miura M, Maiorov B, Baily S A, Haberkorn N, Willis J O, Marken K, Izumi T, Shiohara Y and Civale L 2011 Mixed pinning landscape in nanoparticle-introduced $YGdBa_2Cu_3O_y$ films grown by metal organic deposition *Phys. Rev.* B **83** 184519

Miura M, Maiorov B, Kato T, Shimode T, Wada K, Adachi S and Tanabe K 2013 Strongly enhanced flux pinning in one-step deposition of $BaFe_2(As_{0.66}P_{0.33})_2$ superconductor films with uniformly dispersed $BaZrO_3$ nanoparticles *Nat. Commun.* **4** 2499

Miura M, Maiorov B, Willis J O, Kato T, Sato M, Izumi T, Shiohara Y and Civale L 2013 The effects of density and size of $BaMO_3$ (M = Zr, Nb, Sn) nanoparticles on the vortex glassy and liquid phase in $(Y,Gd)Ba_2Cu_3O_y$ coated conductors *Supercond. Sci. Technol.* **26** 035008

Mizukami Y, Konczykowski M, Kawamoto Y, Kurata S, Kasahara S, Hashimoto K, Mishra V, Kreisel A, Wang Y, Hirschfeld P J, Matsuda Y and Shibauchi T 2014 Disorder-induced topological change of the superconducting gap structure in iron pnictides *Nat. Commun.* **5** 5657

Moon K, Scalettar R T and Zimányi G T 1996 Dynamical phases of driven vortex systems *Phys. Rev. Lett.* **77** 2778–81

Murphy J, Tanatar M A, Kim H, Kwok W, Welp U, Graf D, Brooks J S, Bud'ko S L, Canfield P C and Prozorov R 2013 Effect of heavy-ion irradiation on London penetration depth in overdoped $Ba(Fe_{1-x}Cox)_2As_2$ *Phys. Rev.* B **88** 054514

Nakajima Y, Taen T, Tsuchiya Y, Tamegai T, Kitamura H and Murakami T 2010 Suppression of the critical temperature of superconducting $Ba(Fe_{1-x}Co_x)_2As_2$ by point defects from proton irradiation *Phys. Rev.* B **82** 220504

Nakajima Y, Tsuchiya Y, Taen T, Tamegai T, Okayasu S and Sasase M 2009 Enhancement of critical current density in Co-doped $BaFe_2As_2$ with columnar defects introduced by heavy-ion irradiation *Phys. Rev.* B **80** 012510

Nattermann T and Scheidl S 2000 Vortex-glass phases in type-II superconductors *Adv. Phys.* **49** 607–704

Nelson D R and Vinokur V M 1993 Boson localization and correlated pinning of superconducting vortex arrays *Phys. Rev.* B **48** 13060–97

Nordlund K, Ghaly M, Averback R S, Caturla M, Diaz de la Rubia T and Tarus J 1998 Defect production in collision cascades in elemental semiconductors and fcc metals *Phys. Rev.* B **57** 7556–70

Novosel N, Galić S, Pajić D, Zadro K and Babić E 2015 Enhancing superconducting properties of MgB_2 by addition of magnetic particles *J. Supercond. Novel Magn.* **28** 425–30

Obradors X and Puig T 2014 Coated conductors for power applications: materials challenges *Supercond. Sci. Technol.* **27** 044003

Obradors X, Puig T, Palau A, Pomar A, Sandiumenge F, Mele P and Matsumoto K 2011 *Comprehensive Nanoscience and Technology* vol 3 (Amsterdam: Elsevier) pp 303–49

Obradors X, Puig T, Ricart S, Coll M, Gázquez J, Palau A and Granados X 2012 Growth, nanostructure and vortex pinning in superconducting $YBa_2Cu_3O_7$ thin films based on trifluoroacetate solutions *Supercond. Sci. Technol.* **25** 123001

Olson C J, Reichhardt C and Nori F 1998 Nonequilibrium dynamic phase diagram for vortex lattices *Phys. Rev. Lett.* **81** 3757–60

Ortalan V, Herrera M, Rupich M W and Browning N D 2009 Three dimensional analyses of flux pinning centers in Dy-doped $YBa_2Cu_3O_{7-x}$ coated superconductors by STEM tomography *Physica* C **469** 2052–9

OSCon 2012–2017 *SciDAC partnership OSCon* (www.oscon-scidac.org/)

Ovchinnikov Y N and Ivlev B I 1991 Pinning in layered inhomogeneous superconductors *Phys. Rev.* B **43** 8024–9

Padamsee H S 2014 Superconducting radio-frequency cavities *Annu. Rev. Nucl. Part. Sci.* **64** 175–96

Palau A, Bartolomé E, Llordés A, Puig T and Obradors X 2011 Isotropic and anisotropic pinning in TFA-grown $YBa_2Cu_3O_{7-x}$ films with $BaZrO_3$ nanoparticles *Supercond. Sci. Technol.* **24** 125010

Palau A, Parvaneh H, Stelmashenko N A, Wang H, Macmanus-Driscoll J L and Blamire M G 2007 Hysteretic vortex pinning in superconductor-ferromagnet nanocomposites *Phys. Rev. Lett.* **98** 117003

Palonen H, Jäykkä J and Paturi P 2012 Modeling reduced field dependence of critical current density in $YBa_2Cu_3O_{6+x}$ films with nanorods *Phys. Rev.* B **85** 024510

Pastoriza H, Goffman M F, Arribére A and de la Cruz F 1994 First order phase transition at the irreversibility line of $Bi_2Sr_2CaCu_3O_8$ *Phys. Rev. Lett.* **72** 2951–4

Phillips C L, Peterka T, Karpeyev D and Glatz A 2015 Detecting vortices in superconductors: extracting one-dimensional topological singularities from a discretized complex scalar field *Phys. Rev.* E **91** 023311

Polat O, Sinclair J W, Zuev Y L, Thompson J R, Christen D K, Cook S W, Kumar D, Chen Y and Selvamanickam V 2011 Thickness dependence of magnetic relaxation and *E-J* characteristics in superconducting (Gd-Y)-Ba-Cu-O films with strong vortex pinning *Phys. Rev.* B **84** 024519

Prokopec R, Fischer D X, Weber H W and Eisterer M 2015 Suitability of coated conductors for fusion magnets in view of their radiation response *Supercond. Sci. Technol.* **28** 014005

Prozorov R, Kończykowski M, Tanatar M A, Thaler A, Bud'ko S L, Canfield P C, Mishra V and Hirschfeld P J 2014 Effect of electron irradiation on superconductivity in single crystals of $Ba(Fe_{1-x}Ru_x)_2As_2$ ($x = 0.24$) *Phys. Rev. X* **4** 041032

Prozorov T, Prozorov R, Snezhko A and Suslick K S 2003 Sonochemical modification of the superconducting properties of MgB2 *Appl. Phys. Lett.* **83** 2019–21

Prozorov R, Tanatar M A, Roy B, Ni N, Bud'ko S L, Canfield P C, Hua J, Welp U and Kwok W K 2010 Magneto-optical study of $Ba(Fe_{1-x}M_x)_2As_2$ (M = Co and Ni) single crystals irradiated with heavy ions *Phys. Rev.* B **81** 094509

Puig T, Gutiérrez J, Pomar A, Llordés A, Gázquez J, Ricart S, Sandiumenge F and Obradors X 2008 Vortex pinning in chemical solution nanostructured YbCo films *Supercond. Sci. Technol.* **21** 034008

Rizzo N D, Wang J Q, Prober D E, Motowidlo L R and Zeitlin B A 1996 Ferromagnetic artificial pinning centers in superconducting $Nb_{0.36}Ti_{0.64}$ wires *Appl. Phys. Lett.* **69** 2285–7

Roas B, Hensel B, Saemann-Ischenko G and Schultz L 1989 Irradiation-induced enhancement of the critical current density of epitaxial $YBa_2Cu_3O_{7-x}$ thin films *Appl. Phys. Lett.* **54** 1051–3

Robinson M T 1994 Basic physics of radiation damage production *J. Nucl. Mater.* **216** 1–28

Robinson M T and Torrens I M 1974 Computer simulation of atomic-displacement cascades in solids in the binary-collision approximation *Phys. Rev.* B **9** 5008–24

Rotter M, Tegel M and Johrendt D 2008 Superconductivity at 38 K in the iron arsenide $(Ba_{1-x}K_x)Fe_2As_2$ *Phys. Rev. Lett.* **101** 107006

Rouco V, Bartolomé E, Maiorov B, Palau A, Civale L, Obradors X and Puig T 2014 Vortex creep in TFA-YBCO nanocomposite films *Supercond. Sci. Technol.* **27** 115008

Rupich M W and Zhang Y 2015 private communications from AMSC (Rupich) and SuperPower (Zhang)

Rupich M W *et al* 2015 Engineered pinning landscapes for enhanced 2G coil wire *IEEE Trans. Appl. Supercond.* **26** 6601904 (EUCAS 2015)

Rupich M W, Verebelyi D T, Zhang W, Kodenkandath T and Li X 2004 Metalorganic deposition of YBCO films for second-generation high-temperature superconductor wires *MRS Bull.* **29** 572–8

Sadovskyy I A *et al* 2016a Toward superconducting critical current by design *Adv. Mater.* **28** 4593–600

Sadovskyy I A, Koshelev A E, Glatz A, Ortalan V, Rupich M W and Leroux M 2016b Simulation of the vortex dynamics in a real pinning landscape of $YBa_2Cu_3O_{7-\delta}$ coated conductors *Phys. Rev. Appl.* **5** 014011

Sadovskyy I, Koshelev A, Phillips C, Karpeyev D and Glatz A 2015 Stable large-scale solver for Ginzburg–Landau equations for superconductors *J. Comput. Phys.* **294** 639–54

Sakata H, Oosawa M, Matsuba K, Nishida N, Takeya H and Hirata K 2000 Imaging of a vortex lattice transition in YNi_2B_2C by scanning tunneling spectroscopy *Phys. Rev. Lett.* **84** 1583–6

Salovich N W *et al* 2013 Effect of heavy-ion irradiation on superconductivity in $Ba_{0.6}K_{0.4}Fe_2As_2$ *Phys. Rev.* B **87** 180502

Sandu V and Chee C Y 2014 Magnetic nanoparticles in MgB_2 *Physica* C **498** 30–7

Scala N D, Olive E, Lansac Y, Fily Y and Soret J C 2012 The elastic depinning transition of vortex lattices in two dimensions *New J. Phys.* **14** 123027

Schilling A, Fisher R A, Phillips N E, Welp U, Dasgupta D, Kwok W K and Crabtree G W 1996 Calorimetric measurement of the latent heat of vortex-lattice melting in untwinned $YBa_2Cu_3O_{7-\delta}$ *Nature* **382** 791–3

Schmid A 1966 A time dependent Ginzburg–Landau equation and its applications to a problem of resistivity in the mixed state *Phys. Kondens. Mater.* **5** 302

Schuster T, Kuhn H, Koblischka M R, Theuss H, Kronmüller H, Leghissa M, Kraus M and Saemann-Ischenko G 1993 Enhancement of critical current densities by heavy-ion irradiation in $YBa_2Cu_3O_{7-\delta}$ observed using the high-resolution Faraday effect *Phys. Rev.* B **47** 373–83

Schweigert V A and Peeters F M 1998 Phase transitions in thin mesoscopic superconducting disks *Phys. Rev.* B **57** 13817–32

Schweigert V A, Peeters F M and Deo P S 1998 Vortex phase diagram for mesoscopic superconducting disks *Phys. Rev. Lett.* **81** 2783–6

Selvamanickam V *et al* 2013 Enhanced critical currents in (Gd,Y) $Ba_2Cu_3O_x$ superconducting tapes with high levels of Zr addition *Supercond. Sci. Technol.* **26** 035006

Selvamanickam V *et al* 2015b Continuous improvement at superpower of 2G HTS wire for demanding applications *CEC-ICMC (Tuscon, AZ, USA, 28 June–2 July 2015)*

Selvamanickam V, Gharahcheshmeh M H, Xu A, Galstyan E, Delgado L and Cantoni C 2015a High critical currents in heavily doped (Gd,Y)$Ba_2Cu_3O_x$ superconductor tapes *Appl. Phys. Lett.* **106** 032601

Selvamanickam V, Gharahcheshmeh M H, Xu A, Zhang Y and Galstyan E 2015c Critical current density above 15 MA cm^{-2} at 30 K, 3 T in 2.2 μm thick heavily-doped (Gd,Y)$Ba_2Cu_3O_x$ superconductor tapes *Supercond. Sci. Technol.* **28** 072002

Selvamanickam V, Gharahcheshmeh M H, Xu A, Zhang Y and Galstyan E 2015d Requirements to achieve high in-field critical current density at 30 K in heavily-doped (Gd,Y)Ba_2 Cu_3 O_x superconductor tapes *Supercond. Sci. Technol.* **28** 104003

Selvamanickam V, Yao Y, Chen Y, Shi T, Liu Y, Khatri N D, Liu J, Lei C, Galstyan E and Majkic G 2012 The low-temperature, high-magnetic-field critical current characteristics of Zr-added (Gd,Y)$Ba_2Cu_3O_x$ superconducting tapes *Supercond. Sci. Technol.* **25** 125013

Senatore C, Alessandrini M, Lucarelli A, Tediosi R, Uglietti D and Iwasa Y 2014 Progresses and challenges in the development of high-field solenoidal magnets based on RE123 coated conductors *Supercond. Sci. Technol.* **27** 103001

Shimoyama J-i 2014 Potentials of iron-based superconductors for practical future materials *Supercond. Sci. Technol.* **27** 044002

Shiohara Y, Taneda T and Yoshizumi M 2012 Overview of materials and power applications of coated conductors project *Japan. J. Appl. Phys.* **51** 010007

Si W, Han S J, Shi X, Ehrlich S N, Jaroszynski J, Goyal A and Li Q 2013 High current superconductivity in $FeSe_{0.5}Te_{0.5}$-coated conductors at 30 tesla *Nat. Commun.* **4** 1347

Si W, Zhou J, Jie Q, Dimitrov I, Solovyov V, Johnson P D, Jaroszynski J, Matias V, Sheehan C and Li Q 2011 Iron-chalcogenide $FeSe_{0.5}Te_{0.5}$ coated superconducting tapes for high field applications *Appl. Phys. Lett.* **98** 262509

Snezhko A, Prozorov T and Prozorov R 2005 Magnetic nanoparticles as efficient bulk pinning centers in type-II superconductors *Phys. Rev.* B **71** 024527

Strickland N M, Talantsev E F, Long N J, Xia J A, Searle S D, Kennedy J, Markwitz A, Rupich M W, Li X and Sathyamurthy S 2009 Flux pinning by discontinuous columnar defects in 74 MeV Ag-irradiated $YBa_2Cu_3O_7$ coated conductors *Physica* C **469** 2060–7

Sun Y, Pyon S, Tamegai T, Kobayashi R, Watashige T, Kasahara S, Matsuda Y and Shibauchi T 2015a Critical current density, vortex dynamics, and phase diagram of single-crystal FeSe *Phys. Rev.* B **92** 144509

Sun Y, Pyon S, Tamegai T, Kobayashi R, Watashige T, Kasahara S, Matsuda Y, Shibauchi T and Kitamura H 2015b Enhancement of critical current density and mechanism of vortex pinning in H^+-irradiated FeSe single crystal *Appl. Phys. Express* **8** 113102

Swiecicki I, Ulysse C, Wolf T, Bernard R, Bergeal N, Briatico J, Faini G, Lesueur J and Villegas J E 2012 Strong field-matching effects in superconducting $YBa_2Cu_3O_{7-\delta}$ films with vortex energy landscapes engineered via masked ion irradiation *Phys. Rev.* B **85** 224502

Taen T, Nakajima Y, Tamegai T and Kitamura H 2012 Enhancement of critical current density and vortex activation energy in proton-irradiated Co-doped $BaFe_2As_2$ *Phys. Rev.* B **86** 094527

Taen T, Ohtake F, Pyon S, Tamegai T and Kitamura H 2015 Critical current density and vortex dynamics in pristine and proton-irradiated $Ba_{0.6}$ $K_{0.4}$ Fe_2 As_2 *Supercond. Sci. Technol.* **28** 085003

Tamegai T *et al* 2012 Effects of particle irradiations on vortex states in iron-based superconductors *Supercond. Sci. Technol.* **25** 084008

Tarantini C, Lee S, Kametani F, Jiang J, Weiss J D, Jaroszynski J, Folkman C M, Hellstrom E E, Eom C B and Larbalestier D C 2012 Artificial and self-assembled vortex-pinning centers in superconducting $Ba(Fe_{1-x}Co_x)_2As_2$ thin films as a route to obtaining very high critical-current densities *Phys. Rev.* B **86** 1–7

Thompson J R, Krusin-Elbaum L, Civale L, Blatter G and Feild C 1997 Superfast vortex creep in $YBa_2Cu_3O_{7-\delta}$ crystals with columnar defects: evidence for variable-range vortex hopping *Phys. Rev. Lett.* **78** 3181–4

Thompson J R, Polat A, Christen D K, Kumar D, Martin P M and Sinclair J W 2008 Wide-range characterization of current conduction in high-T_c coated conductors *Appl. Phys. Lett.* **93** 042506

Thompson J R, Sun Y R, Civale L, Malozemoff A P, McElfresh M W, Marwick A D and Holtzberg F 1993 Effect of flux creep on the temperature dependence of the current density in Y-Ba-Cu-O crystals *Phys. Rev.* B **47** 14440–7

Thompson J R, Sun Y R, Kerchner H R, Christen D K, Sales B C, Chakoumakos B C, Marwick A D, Civale L and Thomson J O 1992 Enhanced current density J_c and extended irreversibility in single-crystal $Bi_2Sr_2Ca_1Cu_2O_8$ via linear defects from heavy ion irradiation *Appl. Phys. Lett.* **60** 2306–8

Thuneberg E V, Kurkijärvi J and Rainer D 1984 Elementary-flux-pinning potential in type-II superconductors *Phys. Rev.* B **29** 3913–23

Toulemonde M, Bouffard S and Studer F 1994 Swift heavy ions in insulating and conducting oxides: tracks and physical properties *Nucl. Instrum. Methods Phys. Res.* B **91** 108–23

Trommler S, Hänisch J, Matias V, Hühne R, Reich E, Iida K, Haindl S, Schultz L and Holzapfel B 2012a Architecture, microstructure and J_c anisotropy of highly oriented biaxially textured Co-doped $BaFe_2As_2$ on Fe/IBAD-MgO-buffered metal tapes *Supercond. Sci. Technol.* **25** 084019

Trommler S, Hühne R, Hänisch J, Reich E, Iida K, Haindl S, Matias V, Schultz L and Holzapfel B 2012b The influence of the buffer layer architecture on transport properties for $BaFe_{1.8}Co_{0.2}As_2$ films on technical substrates *Appl. Phys. Lett.* **100** 122602

Tsuzuki K, Hara S, Xu Y, Morita M, Teshima H, Yanagisawa O, Noudem J, Harnois C and Izumi M 2011 Enhancement of the critical current densities and trapped flux of Gd-Ba-Cu-O bulk HTS doped with magnetic particles *IEEE Trans. Appl. Supercond.* **21** 2714–7

Umezawa A, Crabtree G W, Liu J Z, Weber H W, Kwok W K, Nunez L H, Moran T J, Sowers C H and Claus H 1987 Enhanced critical magnetization currents due to fast neutron irradiation in single-crystal $YBa_2Cu_3O_{7-\delta}$ *Phys. Rev.* B **36** 7151–4

US Dept. of Energy 2006 Basic research needs for superconductivity *Report of the Basic Energy Sciences Workshop on Superconductivity* (http://science.energy.gov/media/bes/pdf/reports/files/sc_rpt.pdf)

van der Beek C J, Demirdis S, Colson D, Rullier-Albenque F, Fasano Y, Shibauchi T, Matsuda Y, Kasahara S, Gierlowski P and Konczykowski M 2013 Electron irradiation of Co, Ni, and P-doped $BaFe_2As_2$-type iron-based superconductors *J. Phys.: Conf. Ser.* **449** 012023

van Otterlo A, Scalettar R T, Zimányi G T, Olsson R, Petrean A, Kwok W and Vinokur V 2000 Dynamic phases and the peak effect in dirty type II superconductors *Phys. Rev. Lett.* **84** 2493–6

Vlcek B M, Viswanathan H K, Frischherz M C, Fleshler S, Vandervoort K, Downey J, Welp U, Kirk M A and Crabtree G W 1993 Role of point defects and their clusters for flux pinning as determined from irradiation and annealing experiments in $YBa_2Cu_3O_{7-\delta}$ single crystals *Phys. Rev.* B **48** 4067–73

Vodolazov D Y 2013 Vortex-induced negative magnetoresistance and peak effect in narrow superconducting films *Phys. Rev.* B **88** 014525

Welp U, Fendrich J A, Kwok W K, Crabtree G W and Veal B W 1996 Thermodynamic evidence for a flux line lattice melting transition in $YBa_2Cu_3O_{7-\delta}$ *Phys. Rev. Lett.* **76** 4809–12

White A E *et al* 1988b Ion-beam-induced destruction of superconducting phase coherence in $YBa_2Cu_3O_{7-\delta}$ *Phys. Rev.* B **37** 3755–8

White A E, Short K T, Dynes R C, Levi A F J, Anzlowar M, Baldwin K W, Polakos P A, Fulton T A and Dunkleberger L N 1988a Controllable reduction of critical currents in $YBa_2Cu_3O_{7-\delta}$ films *Appl. Phys. Lett.* **53** 1010–2

Willis J O, Cooke D W, Brown R D, Cost J R, Smith J F, Smith J L, Aikin R M and Maez M 1988 Proton radiation damage in superconducting $EuBa_2Cu_3O_x$ and $GdBa_2Cu_3O_x$ *Appl. Phys. Lett.* **53** 417–9

Wimbush S C, Durrell J H, Tsai C F, Wang H, Jia Q X, Blamire M G and MacManus-Driscoll J L 2010 Enhanced critical current in $YBa_2Cu_3O_{7-\delta}$ thin films through pinning by ferromagnetic $YFeO_3$ nanoparticles *Supercond. Sci. Technol.* **23** 045019

Winiecki T and Adams C 2002a A fast semi-implicit finite-difference method for the {TDGL} equations *J. Comput. Phys.* **179** 127–39

Winiecki T and Adams C S 2002b Time-dependent Ginzburg–Landau simulations of the voltage-current characteristic of type-II superconductors with pinning *Phys. Rev.* B **65** 104517

Xiong G C, Li H C, Linker G and Meyer O 1988 Transport properties, phase transition, and recovery near 200 K of proton-irradiated $YBa_2Cu_3O_7$ thin films *Phys. Rev.* B **38** 240–3

Xu A, Braccini V, Jaroszynski J, Xin Y and Larbalestier D C 2012 Role of weak uncorrelated pinning introduced by $BaZrO_3$ nanorods at low-temperature in $(Y, Gd)Ba_2Cu_3O_x$ thin films *Phys. Rev.* B **86** 115416

Xu A, Delgado L, Khatri N, Liu Y, Selvamanickam V, Abraimov D, Jaroszynski J, Kametani F and Larbalestier D C 2014 Strongly enhanced vortex pinning from 4 to 77 K in magnetic fields up to 31 T in 15 mol.% Zr-added (Gd,Y)-Ba-Cu-O superconducting tapes *APL Mater.* **2** 046111

Yamada Y *et al* 2005 Epitaxial nanostructure and defects effective for pinning in $Y(RE)Ba_2Cu_3O_{7-x}$ coated conductors *Appl. Phys. Lett.* **87** 132502

Yamasaki H and Mawatari Y 1999 Current–voltage characteristics of melt-textured YBCO obtained from the field-sweep rate dependence of magnetization *IEEE Trans. Appl. Supercond.* **9** 2651–4

Yan Y and Kirk M A 1998 Observation and mechanism of local oxygen reordering induced by high-energy heavy-ion (U^+, Au^+, Xe^+) irradiation in the high-T_c superconductor $YBa_2Cu_3O_{7-\delta}$ *Phys. Rev.* B **57** 6152–64

Yeninas S *et al* 2013 Upper critical field of isoelectron substituted $SrFe_2(As_{1-x}P_x)_2$ *Phys. Rev.* B **87** 094503

Yeshurun Y, Malozemoff A P and Shaulov A 1996 Magnetic relaxation in high-temperature superconductors *Rev. Mod. Phys.* **68** 911–49

Zeldov E, Majer D, Konczykowski M, Geshkenbein V B, Vinokur V M and Shtrikman H 1995 Thermodynamic observation of first-order vortex-lattice melting transition in $Bi_2Sr_2CaCu_2O_8$ *Nature* **375** 373–6

Zhang Y *et al* 2011 Self-assembled oxide nanopillars in epitaxial $BaFe_2As_2$ thin films for vortex pinning *Appl. Phys. Lett.* **98** 042509

Zhu Y, Cai Z X, Budhani R C, Suenaga M and Welch D O 1993 Structures and effects of radiation damage in cuprate superconductors irradiated with several-hundred-MeV heavy ions *Phys. Rev.* B **48** 6436–50

Zhu J-X, Kim W, Ting C S and Hu C R 1998 Time-dependent Ginzburg–Landau equations for mixed *d*- and *s*-wave superconductors *Phys. Rev.* B **58** 15020–34

Ziegler J and Biersack J 1985 *The Stopping and Range of Ions in Matter* (*Treatise on Heavy-Ion Science*) ed D Bromley (Berlin: Springer) pp 93–129

Zmuidzinas J 2012 Superconducting microresonators: physics and applications *Annu. Rev. Condens. Matter Phys.* **3** 169–214